Using Global Existing Fiber Networks for Environmental Sensing

By Ezra Ip , Fabien Ravet , *Senior Member IEEE*, Hugo Martins , Ming-Fang Huang ,
Tatsuya Okamoto , Shaobo Han, *Member IEEE*, Chaitnaya Narisetty,
Jian Fang , *Member IEEE*, Yue-Kai Huang, *Member IEEE*, Milad Salemi, Etienne Rochat,
Fabien Briffod, Alexandre Goy, Maria del Rosario Fernández-Ruiz ,
and Miguel González Herráez , *Member IEEE*

ABSTRACT | We review recent advances in distributed fiber optic sensing (DFOS) and their applications. The scattering mechanisms in glass, which are exploited for reflectometry-based DFOS, are Rayleigh, Brillouin, and Raman scatterings. These are sensitive to either strain and/or temperature, allowing optical fiber cables to monitor their ambient environment in addition to their conventional role as a medium for telecommunications. Recently, DFOS leveraged technologies developed for telecommunications, such as coherent detection, digital signal processing, coding, and spatial/frequency diversity, to achieve improved performance in terms of measurand resolution, reach, spatial resolution, and bandwidth. We review the theory and architecture of commonly used DFOS methods. We provide recent experimental and field trial results where DFOS was used in wide-ranging applications, such as geo-hazard monitoring, seismic monitoring, traffic monitoring, and infrastructure health monitoring. Events of interest often have unique signatures either in the spatial, temporal, frequency, or wavenumber domains. Based on the temperature and strain raw data obtained from DFOS, downstream postprocessing allows the detection, classification, and localization of events. Combining DFOS with machine learning methods, it is possible to realize complete sensor systems that are compact, low cost, and can operate in harsh environments and difficult-to-access locations, facilitating increased public safety and smarter cities.

KEYWORDS | Brillouin scattering; coherent detection; distributed acoustic sensing (DAS); distributed strain sensing (DSS); distributed temperature sensing (DTS); distributed vibration sensing (DVS); optical communications; optical fiber sensing; Raman scattering; Rayleigh scattering.

Ezra Ip, **Ming-Fang Huang**, **Shaobo Han**, **Jian Fang**, **Yue-Kai Huang**, and **Milad Salemi** are with Optical Networking and Sensing, NEC Laboratories America, Princeton, NJ 08540 USA (e-mail: ezra.ip@nec-labs.com).
Fabien Ravet was with the Department of Operations, Omnisens, 1110 Morges, Switzerland. He is now with Gradesens, 1700 Fribourg, Switzerland.
Hugo Martins and **Miguel González Herráez** are with the Grupo de Ingenieria Fotónica, University of Alcala, 28801 Alcalá de Henares, Spain.
Tatsuya Okamoto is with Nippon Telegraph and Telephone Corp Research and Development, Tsukuba, Ibaraki 305-0805, Japan.
Chaitnaya Narisetty is with the Department of Computer Science, Carnegie Mellon University, Pittsburgh, PA 15213 USA.
Etienne Rochat, **Fabien Briffod**, and **Alexandre Goy** are with Omnisens, 1110 Morges, Switzerland.
Maria del Rosario Fernández-Ruiz is with the Department of Electronics, University of Alcala, 28801 Alcalá de Henares, Spain.

NOMENCLATURE

ADC	Analog-to-digital converter.
AI	Artificial intelligence.
AOM	Acousto-optic modulator.
APD	Avalanche photodiode.
AWGN	Additive white Gaussian noise.
BFS	Brillouin frequency shift.
BGS	Brillouin gain spectrum.

This article has been accepted for inclusion in a future issue of this journal. Content is final as presented, with the exception of pagination.

Ip *et al.*: Using Global Existing Fiber Networks for Environmental Sensing

B-OTDR	Brillouin optical time-domain reflectometry.
B-OTDA	Brillouin optical time-domain analysis.
BPD	Balanced photodiode.
CPR	Carrier phase recovery.
CCW	Counterclockwise.
c.w.	Continuous wave.
CS3	Cable safety self-protection system.
CW	Clockwise.
DAC	Digital-to-analog converter.
DAS	Distributed acoustic sensing.
DD-CP-OTDR	Direct detection of chirped-pulse optical time-domain reflectometry (based on Rayleigh).
DD-OTDR	Direct detection of optical time-domain reflectometry (based on Rayleigh and nonchirped pulses).
DFOS	Distributed fiber optic sensing.
DoC	Depth of cover.
DOF	Degree of freedom.
DSP	Digital signal processing.
DSS	Distributed strain sensing.
DTS	Distributed temperature sensing.
DTSS	Distributed temperature and strain sensing.
DVS	Distributed vibration sensing.
EBPF	Electrical bandpass filter.
EDFA	Erbium-doped fiber amplifier.
ELPF	Electrical low-pass filter.
FDM	Frequency-division multiplexing.
FFT	Fast Fourier transform.
f-k	Frequency–wavenumber.
FOC	Frequency offset compensation.
FUT	Fiber under test.
GTMS	Geotechnical monitoring system.
LO	Local oscillator.
ML	Machine learning.
MOD	Modulator.
M_L	Local magnitude.
M_W	Moment magnitude.
OBPF	Optical bandpass filter.
OFDR	Optical frequency-domain reflectometry.
OTDR	Optical time-domain reflectometry.
PD	Photodiode.
pdf	Probability density function.
PN	Phase noise.
R-OTDR	Raman optical time-domain reflectometry.
ROW	Right of way.
SBS	Stimulated Brillouin scattering.
SDM	Spatial-division multiplexing.
SMC	Subsidence monitoring cable.
SNR	Signal-to-noise ratio.
SOFAR	Sound fixing and ranging.
SOP	State of polarization.
SpBS	Spontaneous Brillouin scattering.

SpRS	Spontaneous Raman scattering.
TDE	Time-domain equalizer.
TMC	Temperature monitoring cable.
WDM	Wavelength-division multiplexing.
ϕ-CP-OTDR	Chirped pulse phase optical time-domain reflectometry (based on Rayleigh).
ϕ-OTDR	Phase optical time-domain reflectometry (based on Rayleigh and nonchirped pulses).
ULE	Ultralow expansivity.
VTMS	Vehicle traffic monitoring system.
WDL	Wavelength-dependent loss.
XPM	Cross-phase modulation.

I. INTRODUCTION

The optical fiber network is the backbone of modern telecommunications infrastructure. As of 2020, there exist more than four billion kilometers of installed optical fibers worldwide [1]. Optical fiber cables crisscross the world's oceans, forming dense networks around major metropolitan areas. Although optical fibers were first conceived for telecommunications [2], the potential of fibers to serve as sensors was noted as far back as the 1970s. In 2020, the global distributed fiber optic sensor market exceeds $1 billion in annual revenue and is expected to grow at a compound annual growth rate (CAGR) of 8.4% from 2021 to 2028 [3], [4].

The earliest fiber sensing devices were interferometric acoustic sensors [5], [6], [7]. By splitting a c.w. laser and sending one part through a sensing fiber arm that is perturbed by mechanical vibration and the other part through an unperturbed reference arm, the phase modulation induced by mechanical vibration on the sensing fiber can be retrieved from the interferometric signal between the two arms. Another early type of interferometer sensor based on a fiber ring was described in [8]. These sensors are based on forward transmission.

A key innovation in DFOS was the realization that Rayleigh backscatter that arises from refractive index inhomogeneities can yield an OTDR return signal. This effect was first exploited to measure fiber attenuation, and connector and splice losses [9], [10]. An early distributed sensor based on polarization variation in the OTDR was proposed in [11]. OTDR in optical fiber is functionally equivalent to a 1-D optical radar where the medium of propagation has sensitivity along its entire length. Technologies that have already been developed for free-space radar can also be applied for detecting and ranging disturbances along optical fibers. For example, OFDR is optical fiber's equivalent of a chirp radar [12].

The scattering mechanisms in fiber that can be exploited for reflectometry-based DFOS are Rayleigh, Brillouin, and Raman scatterings (see Fig. 1). Rayleigh scattering is an elastic, linear scattering process where no energy is transferred between the incident light and the glass medium.
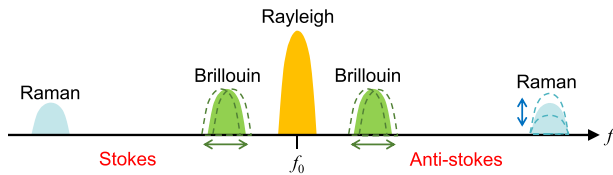
Fig. 1. *Scattering mechanisms in an optical fiber that are exploited in reflectometry-based DFOS.*

The return light is at the same frequency as the input signal. If the input light is coherent, the backscatter from various points along the fiber interferes, resulting in a speckle pattern that is a signature of the fiber state, and can be characterized as a Rayleigh impulse response. If temperature changes or mechanical stress is applied, the interference pattern changes. By comparing the interference pattern over time, thermal and mechanical disturbances can be measured. Alternatively, it can be viewed that longitudinal strain causes a change in optical distance between scatterers, translating into an optical phase change of the return light. Rayleigh scattering is the physical phenomenon used in DAS and DVS interrogators. In DAS, the recovered waveform is a linear function of the acoustic waveform, while DVS is based on intensity measurement, and the recovered waveform is a nonlinear function of the vibration waveform. Examples of DVS and DAS applications based on Rayleigh scattering include fiber microphones [13], [14], perimeter intrusion detection [15], [16], traffic monitoring [17], [18], and seismic monitoring [19], [20], [21].

In contrast to Rayleigh scattering, Brillouin and Raman scatterings are inelastic scattering processes where the incident light interacts with the propagation medium, and the return light is at a relative frequency shift compared with the input signal. Scatterings at frequencies below and above that of the incident light are denoted as "Stokes" and "anti-Stokes" processes, respectively.

Brillouin scattering arises from the interaction between the propagating light and thermally excited acoustic phonons that propagate in guided acoustic modes of the fiber. The acoustic pressure wave modulates the optical refractive index through the elasto-optic effect, behaving as a traveling wave grating that propagates along the fiber at the acoustic velocity. This produces a diffracted light at a Doppler shift relative to the propagating signal. This BFS depends on the doping composition of the fiber, as the "acoustic density" impacts the profile and propagation characteristics of the guided acoustic modes [22]. The BFS is typically around 10–11 GHz. More importantly from the perspective of sensing, BFS changes with both temperature and applied strain. A Brillouin sensor that measures the BFS of the backscattered light at every point along the fiber can, thus, estimate its temperature and strain profile [23], [24], [25], [26], [27], [28]. Brillouin scattering forms the basis of numerous DSS, DTS, and DTSS systems. Examples of applications using Brillouin scattering include

monitoring the integrity of civilian infrastructure, such as oil & gas pipelines [29], [30], [31], [32], railways [33], [34], bridges [35], [36], dams [37], [38], and airframe integrity [39], [40]. Brillouin sensors can be based on either spontaneous or stimulated photons. In the latter approach, a pump beam whose frequency is at the BFS relative to the sensing signal is intentionally launched in a counterpropagating direction to provide stimulated amplification for the backscatter. The use of stimulation significantly increases the power of the return signal, improving its optical SNR, which allows for improved measurement range and performance.

Finally, Raman scattering is caused by thermally influenced molecular vibrations. The Raman spectrum in glass fiber peaks at around 13 THz from the incident light. Since the probability of occupancy of Stokes and anti-Stokes phonons is temperature-dependent, the ratio of their powers can be used to infer temperature at a given fiber position. Raman backscatter is, thus, used for DTS [41], [42], [43]. Raman-based DTS applications include monitoring of oil wells [44], [45], oil & gas pipelines [46], [47], power transformers [48], [49], and soil moisture monitoring [50], [51].

In addition to temperature and strain, it is also possible for DFOS to sense other physical perturbations around the fiber, so long as these can be transduced into a strain or temperature perturbations through cable design or the use of specialty fibers [52], [53], [54], [55].

Although acoustic and temperature sensors can be realized using other technologies [56], [57], fiber optic sensors offer compelling advantages. First, DFOS allows the telecommunications infrastructure to be reused for environmental sensing, providing telecom operators with new sources of revenue. The ubiquity of optical fiber, particularly in urban areas, makes wide-area sensing possible and can facilitate public safety and enable smarter cities. Second, the glass medium has advantages such as greater resistance to corrosion compared with metals and plastics, as well as tolerance to high temperatures, high voltages, and relative immunity from electromagnetic interference. Fiber optic sensors can operate in extreme environments where other types of sensors fail. Third, optical fibers typically have diameters of only around 125 μm and are of small size and lightweight. As a propagation medium, its attenuation coefficient of around 0.2 dB/km is lower than competing technologies. Fourth, by combining optical channels using a wavelength-division multiplexer (WDM), sensing channels and telecommunication channels can coexist in the same optical fiber [18], [58], [59]. In metropolitan and long-haul networks, optical components, such as inline EDFAs, have isolators at their outputs and may prevent backscatter from reaching the transponder. Modifications to the network infrastructure may be necessary to enable compatibility with DFOS. This topic has been investigated in [18] and [60].

In DFOS, tradeoffs are made between spatial resolution, measurand resolution, and system reach. The use of higher

bandwidth sensing signals—or equivalently, signals with shorter temporal features—improves spatial resolution. However, this leads to increased noise, reducing the available SNR at the detector, which either results in worse measurand resolution, or a reduction in system reach or reduction in the number of sensing points. Similar tradeoffs must also be made between measurement time and acoustic frequency resolution. A definition of interrogator performance is reviewed in [61].

In DFOS methods based on phase measurement, the spectral quality of the laser may be important since time-varying strain or temperature also manifests as optical phase variations. Laser PN is, thus, an additive noise source. Even when using direct detection, laser PN may still result in amplitude fluctuations similar to that induced by strain or temperature changes. An analogy can be made with data transmission, where AWGN from inline amplifiers and laser PN both degrade signal detection performance [62], [63]. The noise tolerance of a DAS system depends on the amplitude and bandwidth of the vibration event being measured. To achieve high measurand resolution, low PN lasers with a linewidth below 100 Hz are typically required. Moreover, the energy of seismic vibration is concentrated in the 0.01–20-Hz range, which is a region where laser technical noise dominates. Seismic sensing based on phase measurement may require using specialized lasers that are thermally and mechanically stabilized with flat frequency noise down to sub-Hz level [64]. Such lasers can be expensive instruments. Thus, there exists a tradeoff between cost and required performance.

Although DFOS methods used commercially today were invented decades ago, their full potential has only recently begun to be fully realized. One of the most important recent advances is in coherent receivers [65] and DSP [62], [63], [66], [67]. Just as in telecommunications where these technologies were first developed, coherent detection and DSP offer similar advantages to DFOS. The ability to reconstruct the baseband electric field of the received signal preserves information in all the fiber's DOFs during the optical-to-electrical downconversion process, allowing for its subsequent arbitrary manipulation in DSP. Digital filters implemented in DSP can achieve superior rejection of out-of-band noise compared with analog electrical filters. Imperfections in optoelectronic devices can be digitally compensated. A digital coherent DFOS transponder is easily reconfigurable. Parameters such as the bandwidth of the sensing pulse and its chirp rate, the pulse repetition rate, and the differential gauge length can all be modified in software, enabling software-defined DFOS in the same manner that software-defined networks (SDNs) have revolutionized telecommunications.

DFOS can borrow other DSP tools from telecommunications. For example, coding is a widely used tool to improve system performance. In DFOS, codes with good autocorrelation property approximating a delta function allow increased energy to be launched into a fiber cable while keeping peak power below nonlinear limits and preserving spatial resolution. Simplex codes and Golay codes have been used in Rayleigh-based DFOS [68], [69], while chirped pulses were demonstrated in [70], [71], [72], [73], [74], [75], and [76]. DFOS systems based on Brillouin and Raman backscatters are sensitive to only the amplitude of the incident signal, and Simplex codes [77], [78], [79], cyclic codes [80], [81], complementary Golay codes [82], [83], [84], genetically optimized aperiodic codes [85], and color codes [86], [87] have been considered.

Spatial and frequency diversities are other communications' tools that can be used by DFOS to improve sensing performance. Not only does N-fold diversity increases SNR by a factor of N, it can also mitigate fading, as backscatter is a statistical process where the reflected light at any fiber position may have low amplitude, leading to dead zones with poor performance. Scattering in different frequency bands, different fiber cores, or different modes of the same fiber is statistically independent. For given performance requirement, diversity can reduce the "outage probability" at any given fiber location [88], [89], [90], [91], [92]. SDM and FDM schemes with time-interleaving can be used to increase the vibration sampling rate above the limit imposed by the round-trip propagation delay of the fiber [93], [94].

DFOS systems based on backscatter ultimately have limitations such as weak return power or compatibility issues if the sensing system needs to operate on amplified links where isolators are present. Recently, an alternative class of methods based on forward transmission was proposed. In one such method, a low PN c.w. laser is launched at one end of a fiber cable and coherently detected at the far end using another low PN c.w. laser as LO [95], [96]. If this c.w. transmission is duplicated in the opposite direction, and a vibration event of interest is well modeled as a point source, then, due to the difference in propagation delay between the disturbance and the two receivers located at opposite ends of the cable, the vibration's position can be estimated by correlating the phases measured at each receiver. It was recently shown that the optical phase can also be retrieved from coherent telecom transponders, allowing the same method to be used on data-modulated telecom signals [58], [97], [98]. The realizable spatial resolution is dependent on the bandwidth of the vibration source and can be on order of kilometers, which is much worse than the spatial resolution achievable using DAS based on backscatter. However, even a spatial resolution of kilometers may be sufficient for estimating the epicenter of earthquakes using submarine cables. In [99] and [100], it was demonstrated that SOP recovered from a coherent receiver can also be used to detect earthquakes. However, the localization ability of this scheme has not yet been demonstrated.

The structure of this article is given as follows. In Section II, we review the theory and architecture of commonly used DFOS methods based on Rayleigh, Brillouin, and Raman backscatters, as well as recently
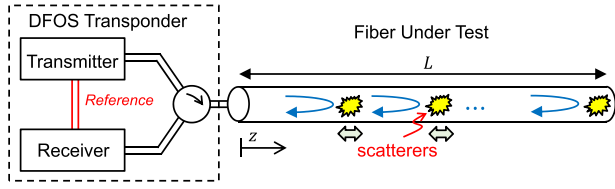
Fig. 2. *Canonical model of a DFOS system based on measurement of backscatter from the FUT.*

developed methods based on forward transmission. Sections III–VII cover DFOS applications. In Section III, geohazard monitoring of soil erosion, landslides, and subsidence is reviewed. This is followed by traffic monitoring and cable health monitoring in Sections IV and V. In Sections VI and VII, we review ocean wave monitoring and seismic monitoring, demonstrating the richness of spatiotemporal data that are obtainable using DFOS, and the array of phenomena that can be characterized in the f-k domains. Finally, practical implementation issues associated with deploying DFOS systems over installed telecom fibers are discussed in Section VIII.

II. THEORY
A. Distributed Fiber Optic Sensing Model

The principle of DFOS systems based on the measurement of backscatter is to obtain an OTDR signal from the FUT [101]. A canonical model of such a DFOS system is shown in Fig. 2. The sensing transponder consists of a transmitter that generates the sensing (probe) signal and a receiver that detects the backscatter from the fiber. Signals are launched and received from the FUT via a circulator. The transmitter's seed laser can be provided as a reference to the receiver if the method requires phase comparison.

An OTDR can be generated by launching pulses into the FUT. One way to generate sensing pulses with a high extinction ratio is to use an AOM. Let $p(t) = (P)^{1/2}\mathrm{rect}(t/T)$ be a rectangular pulse with peak power P and pulse duration T. Its Fourier transform is $P(f) = (P)^{1/2}T \cdot \mathrm{sinc}(fT)$, which has a one-sided bandwidth of $B = 1/T$ measured to the first null of the $\mathrm{sinc}(\cdot)$ function.

B. DFOS Based on Time-Domain Measurement of Rayleigh Backscatter

Due to the Rayleigh backscatter, the segment of the FUT from $z - \Delta z/2$ to $z + \Delta z/2$ will generate an electric field of

$$\mathbf{y}_z(t) = e^{-2\alpha z - j2kz}\mathbf{s}(z)p(t - \tau)\Delta z \qquad (1)$$

where α is the attenuation coefficient of the fiber and $k = 2\pi\nu n_{\mathrm{eff}}/c$ is the propagation constant, with ν being the optical frequency of the probe signal and n_{eff} being the effective index of the fiber. Each polarization component

of $\mathbf{s}(z)$ is a circular Gaussian random variable [102] whose mean-square amplitude $E[|\mathbf{s}(z)|^2]$ is a property of the fiber and is typically on the order of -70 to -75 dB/m. $\tau = (2n_{\mathrm{eff}}/c)z$ is the round-trip propagation delay. The Rayleigh backscatter generated by the whole FUT is the integration of (1) over its entire length L. It can be shown that the Rayleigh backscatter can be characterized as an impulse response where delay t maps to fiber position z

$$\mathbf{h}(t) = \int_0^L \mathbf{s}(z)e^{-2\alpha z - j2kz}\delta\left(t - \frac{2n_{\mathrm{eff}}}{c}z\right)dz. \qquad (2)$$

Neglecting laser PN, the received signal is the convolution between the sensing signal with $\mathbf{h}(t)$

$$\mathbf{y}(t) = p(t) \otimes \mathbf{h}(t) + \mathbf{n}(t) \qquad (3)$$

where $\mathbf{n}(t)$ is the total noise added by the system, including amplified spontaneous emission (ASE) of any inline amplifiers along the FUT, as well as shot noise and thermal noise of the receiver. The resolvable time scale of $\mathbf{y}(t)$ determines the spatial resolution of the OTDR. Taking the Fourier transform of (3), we have $\mathbf{Y}(f) = P(f)\mathbf{H}(f) + \mathbf{N}(f)$. The Rayleigh frequency response $\mathbf{H}(f)$ is typically wideband with bandwidth scaling inversely proportionally to the size of the microscopic refractive index inhomogeneities. The bandwidth of $\mathbf{Y}(f)$ is, thus, usually determined by the probe signal $P(f)$. Hence, the spatial resolution of the OTDR is given by

$$z_r = \frac{c}{2n_{\mathrm{eff}}B}. \qquad (4)$$

An important parameter is $N_z = \lfloor L/z_r \rfloor$, which is the number of independent sensing points in the FUT, also sometimes referred to as the number of "sensing channels."

In the presence of an environmental disturbance arising from longitudinal stress σ along the fiber axis or a change in temperature ΔT_e, the round-trip phase between two scatters separated by Δz is [103]

$$\delta\phi = \delta\phi_0\left(1 + k_\epsilon\epsilon + k_{\Delta T_e}\Delta T_e\right) \qquad (5)$$

where $\delta\phi_0 = 4\pi\nu n_{\mathrm{eff}}\Delta z/c$ is the round-trip phase in ambient conditions and $\epsilon = \sigma/E$ is the induced strain with E being Young's modulus of glass. In the standard single-mode fiber, k_ϵ is typically around 0.78 and takes into the strain-optic effect 104], while $k_{\Delta T_e}$ has been estimated to be around 6.92×10^{-6} [103] and accounts for the thermo-optic effect and thermal expansion of glass.

At short time scales, temperature change can be neglected, and time variations in $\mathbf{h}(t)$ can be assumed to arise from strain only. Two standard detection methods are direct detection and differential phase detection. In both methods, $p(t)$ is transmitted periodically at a rate
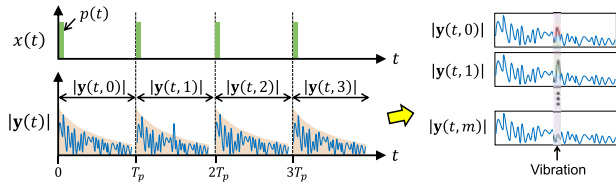
Fig. 3. *Illustrating the parallelization of the received backscatter into frames when a periodic signal is launched into the FUT.*

Fig. 4. *Architecture for DD-OTDR. MOD: optical modulator. OBPF: optical bandpass filter. PD: photodiode. ELPF: electrical low-pass filter. ADC: analog-to-digital converter.*

of $R_p = 1/T_p$, where the repetition (frame) period T_p should be longer than the round-trip propagation delay $T_{2L} = (2n_{\text{eff}}/c)L$ of the FUT. Accounting for PN of the transmitter's seed laser $\phi_{\text{Tx}}(t)$, the periodic sensing signal is

$$x(t) = e^{j\phi_{\text{Tx}}(t)} \sum_m p(t - mT_p). \tag{6}$$

and the received signal $\mathbf{y}(t) = x(t) \otimes \mathbf{h}(t) + \mathbf{n}(t)$ can be parallelized into frames, as shown in Fig. 3. Assuming that the continuous-time signal is then sampled at an interval T_s, the parallelized output is

$$\mathbf{y}[n, m] = \begin{cases} \mathbf{y}(nT_s + mT_p), & 0 \le nT_s < T_p \\ 0, & \text{else} \end{cases} \tag{7}$$

where n is the distance index as fiber position maps to delay and m is the vibration sampling time index. The pulse repetition rate R_p is the vibration sampling rate, allowing vibrations up to the Nyquist frequency of $R_p/2$ to be recovered without aliasing. As the length of the FUT determines the maximum R_p, if a higher sampling rate is required to sense fast vibrations, a time-interleaving scheme via FDM or SDM can be used [93], [94].

1) DVS Using Direct Detection of Rayleigh Backscatter: Vibration detection using direct detection of the Rayleigh backscatter measures change in $|\mathbf{y}[n, m]|^2$ over time index m and is sometimes referred to as DVS. This method is possible because the spatial resolution z_r is much larger than the length scale of refractive index inhomogeneities. As per (5), time-varying longitudinal strain causes the round-trip phase delay between the scatterers to change, so their coherent sum sometimes adds constructively and at other times destructively, resulting in amplitude fluctuation around the neighborhood of the vibration [see Fig. 3 (right)].

The transponder architecture for DD-OTDR is shown in Fig. 4. The advantage of this method is a simple receiver design, comprising only a noise-rejection OBPF of bandwidth B_o, followed by a photodetector and an ELPF of bandwidth B_e. The disadvantage is that amplitude change is not a linear function of strain; thus, the vibration waveform cannot be reconstructed from $|\mathbf{y}[n, m]|^2$.
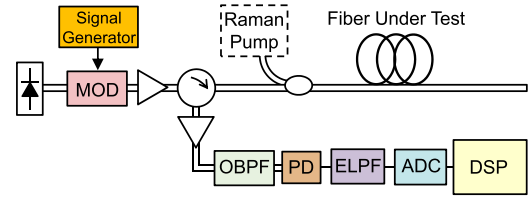
Furthermore, practical OBPFs have much larger bandwidths than the sensing signal, resulting in reduced SNR compared with using a coherent receiver.

2) DAS Using Differential-Detection of Rayleigh Backscatter: An improved vibration detection method uses phase-OTDR (ϕ-OTDR), which recovers $\delta\phi$ in (5) using differential detection [105], [106]. This method is sometimes referred to as DAS. As $\delta\phi \propto \sigma$, recovery of $\delta\phi$ allows linear reconstruction of the vibration waveform. Differential detection can be accomplished using a coherent receiver front end, as shown in Fig. 5, where the transmitter laser serves as the LO for downconverting the Rayleigh backscatter to the electrical baseband. Coherent detection recovers the full information of the received electric field in all the DOFs of the fiber. A comprehensive review of coherent detection in the context of telecommunications can be found in [62] and [63]. Two commonly used configurations are homodyne detection and heterodyne detection (see Fig. 6). In homodyne detection, the center frequency of the signal (ν_{tx}) and the frequency of the LO (ν_{rx}) are the same. As their beat product is centered at zero frequency, the baseband electrical signal will be complex-valued. The optical hybrid must provide two outputs (in-phase and quadrature) per polarization. In heterodyne detection, the frequency difference $|\nu_{\text{rx}} - \nu_{\text{tx}}|$ is deliberately set larger than the one-sided bandwidth B of the signal so that their beat product occupies only one side of the frequency axis. This enables the baseband signal to be reconstructed by detecting only one of the two
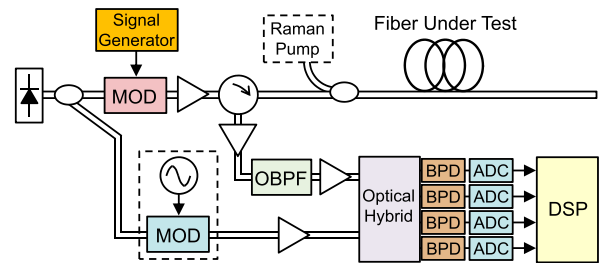

Fig. 5. *Architecture for coherent-detection Rayleigh OTDR. BPD: balanced photodetector. The frequency shifter in the dotted box is optional and allows this architecture to be used for B-OTDR.*
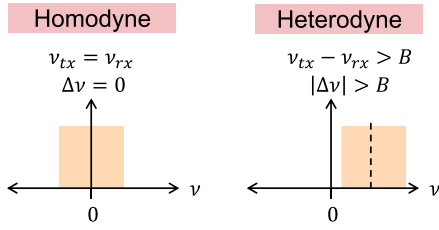
This article has been accepted for inclusion in a future issue of this journal. Content is final as presented, with the exception of pagination.

Ip *et al.*: Using Global Existing Fiber Networks for Environmental Sensing

Fig. 6. *Homodyne versus heterodyne detection.*

quadratures. Heterodyne detection saves one PD per polarization but at the expense of requiring wider bandwidth components, which is typically not a problem in sensing.

Since the laser that generates the probe signal in Fig. 5 also serves as LO, if the MOD does not produce a frequency shift (e.g., a Mach–Zehnder MOD), the architecture shown would be homodyne detection. However, AOMs are also commonly used in sensing transponders due to their high extinction ratio. An AOM produces a frequency shift f_{aom} typically on the order of tens of MHz. If the bandwidth of the probe signal is narrower than f_{aom}, the architecture would be heterodyne detection (e.g., [105]). An optional frequency shifter can be included in the LO path, as shown by the dotted box in Fig. 5. This enables the same architecture to be used to detect Brillouin backscatter at reasonable baseband bandwidth, as discussed in Section II-D.

The purpose of the coherent receiver is to recover the baseband electric field

$$\mathbf{y}(t) = e^{j\phi_{\mathrm{Tx}}(t)}\left[x(t) \otimes \mathbf{h}(t)\right] + \mathbf{n}(t). \tag{8}$$

This signal is typically sampled and digitized at a synchronous rate of $1/T_s = M/T$, where M is the oversampling ratio relative to the pulse bandwidth. As per (7), the signal can be parallelized into frames to obtain $\mathbf{y}[n,m] \triangleq \mathbf{y}(nT_s + mT_p)$, which is a 2×1 complex-valued vector of the backscatter's electric field at distance index n and time index m. Differential products between pairs of polarizations i and j can then be computed at the delay Δ_g, which emulates a differential gauge length of $z_g = \Delta_g(c/2n_{\mathrm{eff}})T_s$

$$\zeta_{ij}[n,m] = y_i[n,m]\, y_j^*[n-\Delta_g,m], \quad i,j \in \{1,2\}. \tag{9}$$

In principle, taking the unwrapped phase of any $\angle\zeta_{ij}[n,m]$ yields an estimate of fiber strain $\epsilon[n,m]$ at that position and time. However, as each $\zeta_{ij}[n,m]$ is the product of two circularly Gaussian random variables, the reconstructed phase will be noisy at faded positions. A more rigorous approach is to combine them using a rotated-vector-sum method (e.g., [72])

$$\zeta[n,m] = \sum_{ij} e^{-j\phi_{ij,n}} \zeta_{ij}[n,m] \tag{10}$$

where the optimum angles $\phi_{ij,n}$ can be found by taking the correlation between $\zeta_{ij}[n,m]$ over a certain time window. The unwrapped phase $\theta[n,m] = \angle\zeta[n,m]$ is an estimate of the strain $\epsilon[n,m]$ at fiber distance $(n - \Delta_g/2)(c/2n_{\mathrm{eff}})T_s$ and time mT_p.

Robustness against fading can be further improved by using a polarization diversity scheme described in [91], which recovers the full Jones matrix associated with each fiber position. This can be accomplished, for example, by sending alternate pulses in orthogonal polarizations. The terms $\mathbf{h}(t)$, $\mathbf{n}(t)$, and $\mathbf{y}(t)$ in (8) then become 2×2 matrices, where each column is associated with the signals received from launching a pulse in that polarization. The round-trip phase of th scatterer at position index n can be determined using [91]

$$\psi[n,m] = \frac{1}{2}\angle\det(\mathbf{y}[n,m]) \tag{11}$$

and from which the differential phase at the delay Δ_g can be computed as $\theta[n,m] = \mathrm{unwrap}(\psi[n,m] - \psi[n-\Delta_g,m])$.

We can write $\theta[n,m]$ as

$$\theta[n,m] = \delta\phi[n,m] + \phi_{\mathrm{PN}}[n,m] + \phi_{\mathrm{AWGN}}[n,m] \tag{12}$$

where $\phi_{\mathrm{PN}}[n,m]$ and $\phi_{\mathrm{AWGN}}[n,m]$ are noise terms arising from laser PN and AWGN, both of which corrupt our estimate of $\delta\phi[n,m]$. Since $\phi_{\mathrm{PN}}[n,m]$ arises from differential detection between two spatial points separated by gauge time $\tau_g = \Delta_g T_s$, if the laser has one-sided frequency noise spectrum of $S_{\nu\nu}(f)$, the one-sided spectrum of $\phi_{\mathrm{PN}}[n,m]$ will be

$$S_{\phi_{\mathrm{PN}}\phi_{\mathrm{PN}}}(f) = (2\pi)^2 |1 - e^{-j2\pi f\tau_g}|^2 S_{\nu\nu}(f). \tag{13}$$

The spectrum of $\phi_{\mathrm{AWGN}}[n,m]$ term depends on η_N, which is the SNR of $\mathbf{y}[n,m]$ and is subject to Rayleigh fading. Since half of the power of AWGN is in the azimuthal direction, and phase is sampled at a rate R_p, while differential detection doubles the PN power per sample, we have

$$S_{\phi_{\mathrm{AWGN}}\phi_{\mathrm{AWGN}}}(f) = \frac{2}{\eta_N R_p}. \tag{14}$$

The schematic inFig. 7 illustrates the spectrum of $\theta[n,m]$. Note that the vibration term includes both the event of interest and ambient environmental noise (e.g., wind, temperature fluctuations, and equipment noise) For a vibration *event* to be detectable, there must exist frequencies over which $\delta\phi[n,m]$ is larger than all the other terms. The noise power spectral density (PSD) of ϕ-OTDR is $S_{\phi_{\mathrm{PN}}\phi_{\mathrm{PN}}}(f) + S_{\phi_{\mathrm{AWGN}}\phi_{\mathrm{AWGN}}}(f)$ in units of $\mathrm{rad}^2/\mathrm{Hz}$. The measurand resolution of DAS is the smallest strain ϵ that can be resolved. By inverting (5) (assuming strain only)
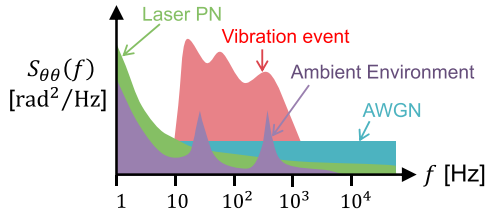
Fig. 7. *Illustrating the requirement for vibration detection. The PSD of an event of interest must be greater than the sum of laser PN, AWGN, and ambient environmental noise over some part of the phase spectrum.*

and setting Δz to the gauge length z_g, we have

$$\epsilon_{\min} = \frac{\lambda}{4\pi (0.78) n_{\text{eff}} z_g} \sqrt{S_{\phi_{\text{PN}}\phi_{\text{PN}}} (f) + S_{\phi_{\text{AWGN}}\phi_{\text{AWGN}}} (f)} \quad (15)$$

in units of $\epsilon/(\text{Hz})^{1/2}$. Note that (15) is frequency-dependent due to coloring by $S_{\phi_{\text{PN}}\phi_{\text{PN}}}(f)$. Of particular interest is laser PN at low frequencies. This technical noise arising from thermal expansion or mechanical vibration of the laser cavity will typically result in $S_{\nu\nu}(f)$ rising above the high-frequency limit of $\Delta\nu/\pi$ imposed by the laser's native Lorentzian linewidth $\Delta\nu$ [107]. Vibration detection at low frequencies is challenging, as it requires lasers to be stable down to 0.1 to 20 Hz for seismic detection [95]. System performance (measurand resolution and low-frequency performance) versus laser cost is an important tradeoff. Laser PN also makes ϕ-OTDR more suitable for measuring dynamic strains than static strains. From Fig. 7, a vibration event of interest can be detected by passing $\theta[n, m]$ (with m being the time variable) through a digital bandpass filter, followed by thresholding or an appropriate ML algorithm for vibration detection and event classification.

If the FUT is unamplified, he received optical power will be lowest at the far end of the FUT, i.e., $P_{\min} = Pe^{-2\alpha L}|\mathbf{s}(L)|^2 z_r$. The minimum SNR is, thus, given by

$$\eta_{\min} = \frac{Pe^{-2\alpha L}|\mathbf{s}(L)|^2 z_r}{N_0} \quad (16)$$

where $N_0 = 2h\nu(F - 1)B$ is the variance of optical noise over the bandwidth of the sensing signal assuming matched filtering and is set by the receiver's preamplifier, where ν is the optical frequency of the sensing signal and F is the noise figure of the preamplifier. As the amplitude of each polarization component $|s_i(L)|$ is Rayleigh distributed, $\eta_{\min}$ is statistical. For a given SNR sensitivity level, there exists an outage probability.

3) Coded-DAS Using Rayleigh Backscatter: Although SNR can be improved by increasing the peak power P of

the pulses, in practice, Kerr nonlinearity and Brillouin scattering restrict the usable P, which limits $\eta_{\min}$ and, thus, the sensing range $L_{\max}$ at a given minimum SNR requirement. One method to improve SNR is to replace $p(t)$ with a coded sequence $c(t)$ whose autocorrelation function $R_{cc}(t) = c(t) * c(t)$ approximates a delta function

$$R_{cc} (t) = \int_{-\infty}^{+\infty} c\left(t'\right) c\left(t' + t\right) dt' \approx N \cdot \delta (t). \quad (17)$$

Neglecting laser PN, it is observed that

$$\begin{aligned} c(t) * \mathbf{y}(t) &= c(t) * [c(t) \otimes \mathbf{h}(t) + \mathbf{n}(t)] \\ &\approx N \cdot \mathbf{h}(t) + c(t) * \mathbf{n}(t) \\ &= N \cdot \hat{h}(t). \end{aligned} \quad (18)$$

Thus, the Rayleigh impulse response can be estimated by performing correlation detection on the received signal $\mathbf{y}(t)$. It is important that $R_{cc}(t)$ is negligible outside of a narrow time window. Otherwise, $\hat{h}(t) = (1/N)R_{cc}(t) \otimes \mathbf{h}(t)$ will have "spatial leakage," i.e., $\hat{h}(t)$ will have contributions from $\mathbf{h}(t - u)$ for certain values of u. This means that vibration at the fiber position with delay $t - u$ will appear at the fiber position with delay t. Examples of "good" codes that have been proposed for coded ϕ-OTDR include simplex codes [68], Golay codes [69], and chirped pulses [72]. Golay codes comprise a pair of bipolar sequences $a[l]$ and $b[l]$ of length $N = 2^M$, with the special property that the sum of their autocorrelation functions is a delta function

$$a[l] * a[l] + b[l] * b[l] = 2N \cdot \delta[l]. \quad (19)$$

In Golay-coded ϕ-OTDR, the transmitter sends $a(t) = \sum_n a[l]p(t - lT)$ during odd frames, and $b(t) = \sum_n b[l]p(t - lT)$ during even frames. $p(t)$ is the pulse shape and can be a rectangular pulse of duration T defined earlier. Let $\mathbf{y}_a(t)$ and $\mathbf{y}_b(t)$ be the Rayleigh backscatter received due to launching $a(t)$ and $b(t)$ into the FUT. The receiver performs correlation detection. In the absence of AWGN or PN, the autocorrelation property of Golay codes gives

$$a(t) * \mathbf{y}_a(t) + b(t) * \mathbf{y}_b(t) = 2N \cdot R_{pp}(t) \otimes \mathbf{h}(t) \quad (20)$$

where $R_{pp}(t)$ is the autocorrelation of $p(t)$. This is the same result as passing the received signal for the uncoded case in (3) through a matched filter, and the extra factor of $2N$ is the coding gain. Since two frames are needed to produce one estimate of $\mathbf{h}(t)$, the SNR gain is N. A disadvantage of using Golay codes is that, if the channel changes between frames, there will be a loss of performance due to spatial leakage not canceling when summing the correlation outputs of two consecutive frames.

This article has been accepted for inclusion in a future issue of this journal. Content is final as presented, with the exception of pagination.

Ip *et al.*: Using Global Existing Fiber Networks for Environmental Sensing

An alternative approach is to use chirped pulses as the "coded" sequence. In this case, the transmitter sends [108], [109]

$$p(t) = \sqrt{P}\exp\left(j2\pi\gamma\frac{t^2}{2}\right)\text{rect}\left(\frac{t}{T_c}\right) \qquad (21)$$

where T_c is the chirp duration and γ is the chirp rate since the instantaneous frequency of (21) is $f(t) = \gamma t$. One way to generate chirped pulses is to use digital-DACs driving a Mach–Zehnder I/Q MOD. The signal in (21) has a bandwidth of $B = \gamma T_c$, and its autocorrelation is

$$R_{pp}(t) = (T_c - |t|)\,\text{sinc}\,(\gamma t\,(T_c - |t|)). \qquad (22)$$

For long chirp duration $T_c \gg T$, the width of the $\text{sinc}(\cdot)$'s main lobe is $T = 1/\gamma T_c = 1/B$, which is the same spatial resolution as using a rectangular pulse of duration T in uncoded ϕ-OTDR. The effective "code length" of a chirped pulse is $N = T_c/T$. Hence, ϕ-CP-OTDR also increases SNR by the coding gain N. ϕ-CP-OTDR has also been referred to as time-gated domain OFDR (TGD-OFDR) [72]. The use of ϕ-CP-OTDR recently yielded a single-span DAS reach of 171 km [75], while a frequency-diversity implementation using all-Raman amplification yielded a DAS reach of 1007 km [76].

C. DFOS Based on Frequency-Domain Measurement of Rayleigh Backscatter

An alternative approach to Rayleigh-based sensing comes from recognizing that the round-trip phase $\delta\phi$ between scatterers in (5) comprises two components: the ambient component $\delta\phi_0 = 4\pi\nu n_{\text{eff}}\Delta z/c$, which is proportional to optical frequency, and the perturbation components, which changes with ϵ and ΔT_e. Suppose that strain and temperature change slowly enough that it is possible to scan the center frequency ν of the probe signal until a frequency offset $\Delta\nu$ is found, which restores $\delta\phi$ to the original value. This can be observed by the speckle pattern $\mathbf{y}[n, m]$ (at center frequency $\nu + \Delta\nu$) returning to the original shape $\mathbf{y}[n, m_0]$ measured at a previous time index m_0 (at center frequency ν) in the neighborhood of position index n. Let the distance-dependent frequency shift be $\Delta\nu[n]$. Inverting (5), we have [103]

$$\frac{\Delta\nu}{\nu} = -k_\epsilon\epsilon - k_{\Delta T_e}\Delta T_e. \qquad (23)$$

At a typical telecom frequency of $\nu = 193.4$ THz, the sensitivity of $\Delta\nu$ to strain and temperature are around 151 MHz/$\mu\varepsilon$ and 1.34 GHz/K, respectively. This is the basis for DTSS using Rayleigh backscatter.

1) DTSS Using Direction Detection of Chirped-Pulse OTDR: A property of chirped pulses introduced in (21) for CP-OTDR is that instantaneous frequency is proportional to
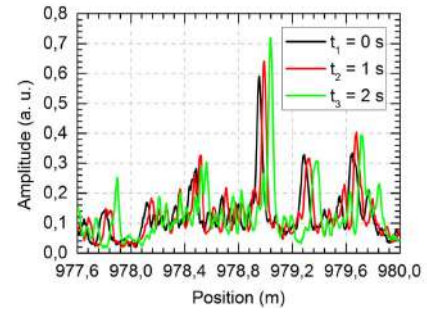

Fig. 8. *Three DD-CP-OTDR frames measured when a region of the FUT around 979 m was heated to three different temperatures [71].*

time and, thus, frequency shift maps to temporal delay. This property is exploited in DD-CP-OTDR that was developed in [74]. The probe pulse is the same as in (21), but the chirp, in this case, is not intended to increase code length but to increase optical bandwidth. The chirp rate is given by $\gamma = \Delta f/T_c$, where $B = \Delta f$ is the chirp-induced bandwidth of $p(t)$. Provided $\Delta f \gg 1/T_c$, i.e., the chirp-induced bandwidth is much larger than the transform-limited pulse bandwidth, localized displacement due to strain or temperature change will manifest as delay of the received amplitude speckle pattern [74]. The DD-CP-OTDR architecture is the same as in Fig. 4 with the output of the MOD being a chirped pulse. Fig. 8 shows examples of three amplitude profiles $|\mathbf{y}[n, m]|^2$ measured in a DD-CP-OTDR experiment when a fiber section around 979 m was heated. The spatial shift of the amplitude profile due to temperature change can be observed [71]. The receiver records an initial amplitude profile at calibration. During measurement, the instantaneous amplitude profile is correlated with the reference over a predetermined window around a fiber position of interest, from which strain or temperature change is inferred from the estimated delay. This method achieves a spatial resolution of

$$z_r = \frac{cT_c}{2n_{\text{eff}}} \qquad (24)$$

as the timescale of the smallest resolvable feature in $|\mathbf{y}[n, m]|^2$ is governed by the pulsewidth T_c.

The use of spatial correlation makes DD-CP-OTDR less sensitive to SNR fluctuations arising from Rayleigh fading than ϕ-OTDR. This is irrespective of whether coded or uncoded pulses are used for coherent ϕ-OTDR, as correlation detection ultimately recovers $\mathbf{h}(t)$ with only a linear coding gain, which is prone to Rayleigh fading. Suppose that the amplitude at a particular fiber position was faded. Since the amplitude of neighboring points is unlikely to also be faded, the spatial correlation should still produce a valid temporal delay. Fig. 9 shows the pdf of strain noise obtained with ϕ-OTDR and DD-CP-OTDR over long-term measurement, which allows averaging of a large number of Rayleigh fading realizations [110], [111]. As the pdf
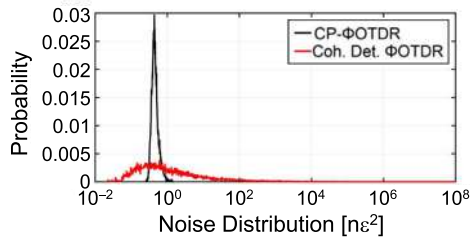
This article has been accepted for inclusion in a future issue of this journal. Content is final as presented, with the exception of pagination.

Ip *et al.*: Using Global Existing Fiber Networks for Environmental Sensing

Fig. 9. *PDF of strain noise using ϕ-OTDR and DD-CP-OTDR [110].*

Fig. 11. *Instantaneous frequency versus time for the LO light in OFDR (with and without delay fiber) and for the Rayleigh backscatter reflected at fiber position z.*

of DD-CP-OTDR has a much smaller standard deviation, this method achieves near-equal performance for all spatial points [110]. This was found to be true even when measuring sub-Hz vibrations at low vibration sampling rates R_p [20]. DD-CP-OTDR is suitable for seismic sensing as the direct detector output can be analyzed without denoising or smoothing to compensate for strain measurement errors at faded positions [21]. The disadvantage is increased detector bandwidth, which must accommodate the chirp-induced bandwidth Δf.

In DD-CP-OTDR, laser PN will also cause the return signal to be delayed, as the derivative of PN is frequency noise. However, the delay caused by laser PN will be constant for all spatial positions n in each frame $|\mathbf{y}[n, m]|^2$, permitting a PN compensation method proposed in [73], where an unperturbed fiber serves as a reference at the transponder. DD-CP-OTDR with laser PN compensation can achieve high strain measurand resolution on the order of $p\epsilon/(\text{Hz})^{1/2}$ even when using lasers with MHz linewidths [112].

2) DTSS Using OFDR: By increasing the chirp duration T_c in (21) to the frame period T_p, we obtain OFDR [113]. A more conventional architecture for OFDR is shown in Fig. 10. The frequency-swept light source can be generated with DACs driving an optical MOD as in CP-OTDR. Alternatively, a wavelength-tunable laser driven by a sawtooth signal can be used. The second approach has the advantage that much larger chirp bandwidths Δf can be produced.
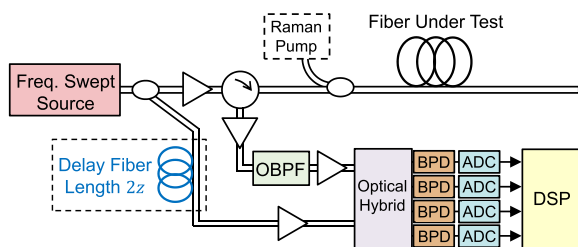

Fig. 10. *Architecture for Rayleigh OFDR (OFDR). The delay fiber sets the reference point in the FUT for the measurement of the Rayleigh frequency response.*
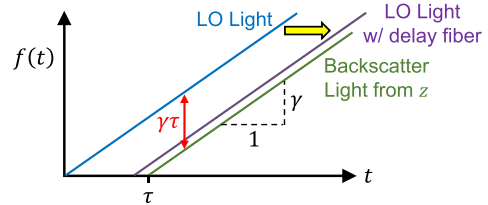
The spatial resolution achieved is [114]

$$z_r = \frac{c}{2n_{\text{eff}}\Delta f}. \qquad (25)$$

A tunable laser sweeping across the C-band ($\sim$5 THz) can yield a spatial resolution of $\sim$20 μm and allows the interrogation of fine structures inside optical devices for characterization and fault diagnosis [115].

As with ϕ-OTDR, the received backscatter can be detected using a coherent receiver, with the difference that the LO is now the frequency-swept source. Fig. 11 shows instantaneous frequency versus time for the LO and the backscattered light reflected at fiber position z, which has a round-trip delay τ. It is observed that their beat product has a constant frequency difference of $-\gamma\tau$. Hence, fiber position maps to beat the frequency of the received signal. If the complex-valued dual-polarization outputs of the coherent receiver are passed through EBPF with bandwidth B_e centered around $-\Delta f = -\gamma\tau$, the output at time t will be an estimate of the Rayleigh frequency response $\mathbf{H}(z, f(t - (2n_{\text{eff}}z/c)))$, where $z = (c/2n_{\text{eff}})(\Delta f/\gamma)$ is the fiber position measured and $f(t)$ is the instantaneous frequency of the frequency-swept light source at t. Note that the Rayleigh impulse response (such as recovered by $\mathbf{y}[n, m]$ in ϕ-OTDR) and the Rayleigh frequency response are related by a 1-D Fourier transform pair $\mathbf{h}(z, t) \xleftarrow{\mathcal{F}} \mathbf{H}(z, f)$. The EBPF output in time is a readout of the spectrum of the Rayleigh backscattered light at z. In addition, an EBPF with bandwidth B_e has an integration time of $\sim 1/B_e$. The measured Rayleigh frequency response is, thus, for a fiber section of length $z_e = (c/2n_{\text{eff}})(B_e/\gamma)$ centered at z, which can be interpreted as a "fiber Bragg grating," where, in the presence of strain or temperature change, the spectrum of the backscattered light will experience a frequency shift. Measuring $\mathbf{H}(z, f)$ over successive time frames (with frame period T_p) and correlating them allow estimation of the spatiotemporal temperature-strain profile of the FUT.

The drawbacks of OFDR as described are: 1) the beat frequency is proportional to the distance from the transponder, potentially requiring large receiver bandwidths and 2) more importantly, the measurement range is limited by the coherence length of the light source [116],

This article has been accepted for inclusion in a future issue of this journal. Content is final as presented, with the exception of pagination.

Ip *et al.*: Using Global Existing Fiber Networks for Environmental Sensing

i.e., when the phase of the LO becomes uncorrelated with the phase of the backscatter generated by the same laser at time τ earlier, frequency of the beat signal will no longer map simply to fiber position. Tunable lasers typically have coherent lengths of only a few tens of meters, which is insufficient for measuring large-scale structures, such as an optical fiber network. It is possible to overcome the coherence length limit by adding a delay fiber of length $2z$, as shown by the dotted box in Fig. 10 [117]. The delay fiber will match the PN of the signal reflected at z with that of the delayed LO while also shifting the beat frequency to dc. The delay fiber, thus, changes the reference position from the circulator output to z. Laser coherence length will determine the relative distance from the reference over which measurement results are not distorted by PN. The delay fiber should be housed in an enclosure more mechanically and thermally stable than the FUT to prevent its environmental noise from impacting measurement results.

In general, using an external MOD to generate the frequency-swept signal will achieve a longer coherence length than using a tunable laser, as a low phase-noise seed laser can be used at the MOD input [118]. Furthermore, the sweep profile of a tunable laser will not be perfectly linear. An additional delay interferometer arm is often used to track the sweep profile and calibrate the OFDR measurement [119]. This requires additional optical and electrical hardware. The external modulation configuration may also allow a higher repetition (frame) rate R_p, allowing faster vibrations to be measured.

As per (23) $\Delta\nu$ is a function of both ϵ and ΔT_e. If one of these variables is static, the other variable can be determined. However, a real fiber cable usually experiences both temperature and strain variations together. Some approaches to temperature-strain discrimination include the following.

1) Using a hybrid Brillouin/Rayleigh system (Brillouin-based DFOS is discussed in Section II-D) [120], [121]. The frequency shifts $\Delta\nu/\nu$ and Δf_B obtained using the Rayleigh and Brillouin systems give rise to a matrix equation

$$\begin{bmatrix} \Delta\nu \\ \Delta f_B \end{bmatrix} = \begin{bmatrix} -\nu k_\epsilon & -\nu k_{\Delta T_e} \\ c_\epsilon & c_{\Delta T_e} \end{bmatrix} \begin{bmatrix} \epsilon \\ \Delta T_e \end{bmatrix}$$

which can be inverted to estimate ϵ and ΔT_e.
2) Using a PM fiber, where birefringent-dependent frequency shift provides an extra parameter $\Delta\nu_{\text{bire}}$, which results in an invertible matrix equation for ϵ and ΔT_e [122].

D. DFOS Based on Brillouin Scattering

In distributed strain and/or temperature sensing using Brillouin scattering, the return signal is at a frequency shift of $\pm f_B$ relative to the input signal. SpBS originates from the interaction between the propagating light with thermally excited acoustic phonons propagating in guided acoustic modes of the fiber. The BGS typically has a linewidth of $\Delta\nu_B \approx 30$ MHz, while its center frequency, or the BFS f_B, is around 10.7 GHz. Both BGS and BFS depend on the doping characteristics of the fiber and the changes in temperature or applied strain. In the presence of strain ϵ or temperature change ΔT at a given fiber position, the BFS at that position will be shifted by [123]

$$\Delta f_B = c_\epsilon \epsilon + c_{\Delta T_e} \Delta T_e \tag{26}$$

where c_ϵ and $c_{\Delta T_e}$ are the strain and temperature coefficients, with typical values around 0.048 MHz/$\mu\varepsilon$ and 1.1 MHz/K, respectively [22], [124]. Note that these shifts are around three orders of magnitude smaller than using Rayleigh in (23).

Just like in Rayleigh OTDR, an uncoded B-OTDR transmitter launches rectangular pulses into the FUT. The coherent receiver, as shown in Fig. 5, can be reused, and Δf_B is estimated at every position in the B-OTDR. To reduce the sampling rate requirement, the transmitter's seed laser can be frequency shifted by the mean value of f_B in ambient conditions. The shifted laser then serves as the LO. In this case, the ADCs only need to sample at a rate of $R_s \geq 2|\Delta f_{B,\text{max}}| + \Delta\nu_B$, where $|\Delta f_{B,\text{max}}|$ is the maximum BFS excursion that can occur at any fiber position at its maximum operating range. This will ensure the sampled signal captures the entire BGS without aliasing. As before, let the sampling rate be $R_s = M/T_s$, where M is the oversampling ratio relative to the pulse bandwidth. The ADC output is parallelized as per (7), and we denote the present signal due to Brillouin backscatter as $\mathbf{y}_B[n, m]$, with n being the delay (position) index and m the time (frame) index. The samples in each frame can be grouped into blocks of length N_b, with the samples in the lth block being $\mathbf{y}_{B,l}[n', m] = \mathbf{y}_B[lN_b + n', m]$ for $0 \leq n' < N_b$. The BGS can be calculated as the square amplitude of the FFT of $\mathbf{y}_{B,l}[n', m]$

$$Y_B[k, l, m] = \left| \sum_{n'=0}^{N_b-1} \mathbf{y}_{B,l}[n', m] e^{-j2\pi n'k/N_b} \right|^2 \tag{27}$$

where k is the frequency index that corresponds to analog frequency kR_s/N_b, l is the position index, and m is the time (frame) index. Although BGS is computed at a distance spacing of $(c/2n_{\text{eff}})(N_b/R_s)$, the spatial resolution is the same as in Rayleigh OTDR given by (4).

Brillouin scattering is typically 15–20 dB weaker than Rayleigh scattering [125]. To estimate BFS accurately, it is often necessary to first average $Y_B[k, l, m]$ over M_B consecutive frames before estimating Δf_B. Temporal averaging will reduce the sampling rate of strain and temperature to R_p/M_B. B-OTDR is more suitable for measuring static or slowly varying strain and temperature.

One method to improve SNR is to use the B-OTDA configuration [22], [23], [24]. In the architecture shown
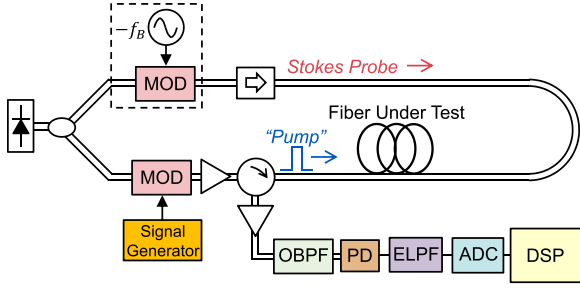
This article has been accepted for inclusion in a future issue of this journal. Content is final as presented, with the exception of pagination.

Ip *et al.*: Using Global Existing Fiber Networks for Environmental Sensing

Fig. 12. *Architecture of Brillouin OTDA (B-OTDA). An SBS generated in the top path by a frequency shifter is launched in a counterpropagating direction to the pulsed or coded "pump" generated in the bottom path. BGS is measured by sweeping f_B.*

in Fig. 12, part of the seed laser is frequency downshifted by f_B in the vicinity of the BFS to generate a Stokes probe signal (SBS) that is launched into the remote end of the FUT. The input signal, either as pulses or as a coded sequence [84], becomes a "pump" that provides stimulated gain to the SBS. The gain experienced by the probe depends on f_B via the BGS and is governed by standard intensity rate equations [126]. By stepping f_B through an appropriate range, the BGS profile of the FUT can be measured. The receiver comprises of an optical filter that selects the Stokes signal followed by direct detection. The advantage of B-OTDA is increased sensing range due to higher received power. A potential drawback is that this method requires access to both ends of the FUT, which is not always feasible in downhole applications but is not a limiting factor in transportation infrastructures.

As with Rayleigh-based sensing, coding can be employed in B-OTDR and B-OTDA to improve SNR. Since Brillouin is based on power measurement, applicable codes can only take nonnegative values. Complementary Golay codes are an example of such a code that was proposed in [83]. This scheme was later used in [84] to demonstrate B-OTDR at 1-cm resolution. Recall the Golay sequences $a[l]$ and $b[l]$ introduced earlier in Section II-B. Four unipolar sequences can be generated as follows:

$$a_1[l] = \frac{1}{2}(1 + a[l]) \tag{28a}$$

$$a_2[l] = \frac{1}{2}(1 - a[l]) \tag{28b}$$

$$b_1[l] = \frac{1}{2}(1 + b[l]) \tag{28c}$$

$$b_2[l] = \frac{1}{2}(1 - b[l]). \tag{28d}$$

From the autocorrelation property of Golay sequences in (19), we have

$$a[l] * (a_1[l] - a_2[l]) + b[l] * (b_1[l] - b_2[l]) = 2N \cdot \delta[l]. \tag{29}$$

The transmitter generates four continuous-time sequences by modulating $a_i[l]$ and $b_i[l]$ with an appropriate

pulse shape, such as rectangular pulses with duration T. The four continuous-time signals are then successively launched into the FUT. Let $\mathbf{y}_{B,a1}(t)$, $\mathbf{y}_{B,a2}(t)$, $\mathbf{y}_{B,b1}(t)$, and $\mathbf{y}_{B,b2}(t)$ be the Brillouin backscatters received from the transmission of $a_1(t)$, $a_2(t)$, $b_1(t)$, and $b_2(t)$, respectively. Suppose that these signals are sampled and digitized at a rate $R_s = M/T_s$ as before, and (27) is invoked by setting $N_b = M$ so that the square amplitude of the FFT is computed at a spatial spacing equal to the baud interval T of the coded sequences. Let $Y_{B,a1}[k,l,m]$ be the square amplitude of the FFT for the mth frame of $a_1(t)$ and so on. From (29), the BGS can be obtained by computing

$$Y_B[k,l,m] = a[l] * (Y_{B,a1}[k,l,m] - Y_{B,a2}[k,l,m]) + b[l] \\ * (Y_{B,b1}[k,l,m] - Y_{B,b2}[k,l,m]) \tag{30}$$

for all frequency indices k, spatial indices l, and frame indices m. For a code of length N, it has been shown that SNR will be improved by a coding gain of $(N + 1/(2N)^{1/2})$ [84]. The square-root proportionality is due to intensity detection.

Simplex codes [78] and cyclic codes [80] are other types of codes that have been demonstrated for Brillouin sensing. These achieved SNR coding gains of $(N + 1/2(N)^{1/2})$ [79]. Improvement in BFS accuracy has also been demonstrated, although not in the same proportion as with SNR. Recently, the pros and cons for unipolar Simplex and Golay codes, as well as optimization rules, were reported in [81], ultimately demonstrating that: 1) simplex codes are preferrable over Golay codes for long-range sensing due to their robustness against pulse power nonuniformity and 2) high-order nonlocal effects limit the optimum code length to $2/g_{\max}$, where $g_{\max}$ is the maximized single-pulse Brillouin gain.

Genetically optimized aperiodic codes have also been studied [85]. Unlike Simplex and Golay codes that require sending different sequences, aperiodic codes use only one unique predefined sequence. One advantage of this approach is that there is no need for individual pulses within the sequence to have the same intensity as in Simplex and Golay, so the transient response of EDFAs is not detrimental to performance.

Ultimately, Simplex, Golay, genetically optimized, and cyclic codes use time as the coding domain. As Brillouin sensing is a frequency analysis, there exist color codes that use not only the time domain but also the frequency domain for coding. A matrix defines the code both in the time and frequency domains; in other words, a different frequency is attributed to any individual pump pulses [86]. To balance energy transfer, the proposed scheme used a dual pump configuration (two pump frequencies at + and – Brillouin shift from the central laser frequency) with a frequency shifted probe to recover the Brillouin changes induced by temperature or strain.

Finally, a combination cyclic color code was also proposed [87]. In this case, there is a running pulse pattern

This article has been accepted for inclusion in a future issue of this journal. Content is final as presented, with the exception of pagination.

Ip *et al.*: Using Global Existing Fiber Networks for Environmental Sensing

that fills the fiber entirely. As one pulse exits, another one enters the fiber, as in an endless ribbon, while each individual pump pulse has a different frequency. Colored cyclic codes have a $(2)^{1/2}$ gain improvement compared with noncyclic codes.

BFS can be obtained from the BGS measured with B-OTDR (coded or uncoded) or B-OTDA in several ways, such as by interpolating $Y_B[k, l, m]$ with quadratic least-squares fit to find the fractional value k, where the BGS has a maximum value [127]. It is also possible to correlate $Y_B[k, l, m]$ with the known BGS shape of the fiber and then find the position of the correlation peak [128], and the detection of temperature or strain anomalies smaller than the spatial resolution has been reported using curve fitting based on spectral analysis and deconvolution [129], [130]. ML methods have also been proposed [131], [132].

As per (26), the BFS Δf_B obtained via B-OTDR or B-OTDA is a function of both ϵ and ΔT_e. Some temperature-strain discrimination approaches that have been described in the literature include the following.

1) Using a hybrid Raman/Brillouin system. As the Raman system (covered in Section II-E) is sensitive to temperature changes only, its contribution to Δf_B can be removed [124], [133].
2) A related approach uses the "Landau–Placzek ratio" between the Brillouin scattering intensity and the Rayleigh scattering intensity to infer temperature independently of strain [134], from which temperature's contribution to Δf_B is removed.
3) Special cable design, such as incorporating tightly strain-coupled fiber with loose tube fiber in the same cable. It is assumed that strain on the loose tube fiber is zero; thus, its BFS is sensitive to temperature only, which allows the strain to be determined from the BFS of the strain-coupled fiber [135].
4) Using diversity, such as two (or more) different cores of a heterogeneous multicore fiber [136] or two (or more) modes of a multimode fiber [137], [138]. Equation (26) then becomes a matrix equation

$$\Delta \mathbf{f}_B = \mathbf{c} \begin{bmatrix} \epsilon \\ \Delta T_e \end{bmatrix}.$$

Provided that $\mathbf{c}$ has rank two, ϵ and ΔT_e can be determined from $\mathbf{c}^{-1} \Delta \mathbf{f}_B$, where $\mathbf{c}^{-1}$ is the either inverse or Penrose pseudoinverse.

5) Exploiting birefringence in a polarization-maintaining (PM) fiber; the dynamic grating created by Brillouin scattering induces different Doppler shifts on x- and y-polarized signals, providing a second variable, Δf_{yx}, with a different dependence on temperature and strain [139].
6) Large-effective area fibers (LEAFs) have multiple Brillouin scattering peaks due to using different dopant compositions or different doping concentrations in
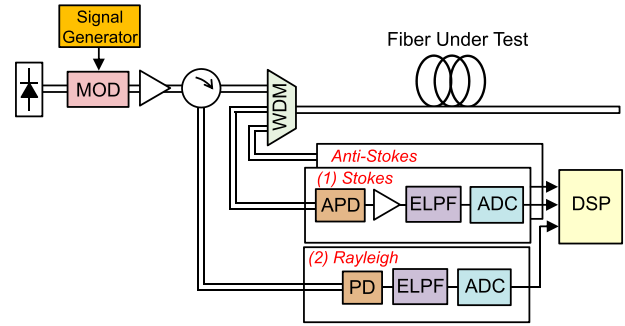

Fig. 13. *Architecture of Raman OTDR (R-OTDR). APD: avalanche photodiode. ELPF: electrical low-pass filter. WDM: wavelength-division multiplexer. Options (1) and (2) use the powers at the Raman Stokes and Rayleigh frequencies, respectively, to normalize the power measured at the Raman anti-Stokes frequency.*

the radial layers to achieve the desired refractive index profile. Similar to 4), this results in an invertible matrix equation for $\Delta \mathbf{f}_B$ [140].

7) In addition to BFS, the shape of the BGS also changes slightly depending on whether the perturbation is caused by temperature or strain. This was exploited in [141] where an artificial neural network (ANN) enabled simultaneous determination of ϵ and ΔT_e from the BGS.

E. DFOS Based on Raman Scattering

The third backscattering mechanism commonly used in DFOS is SpRS, which is an inelastic scattering process where the incident light interacts with phonons associated with thermally influenced molecular vibrations [126].

The architecture for DTS using SpRS is shown in Fig. 13. Just like Rayleigh OTDR, the uncoded R-OTDR transmitter launches rectangular pulses of duration T into the FUT through an optional circulator (if Rayleigh backscatter is used for power normalization) followed by a WDM. Backscattered photons at the Raman anti-Stokes and Stokes frequencies are received on the other two ports of the WDM. Due to low received power, APD is used for photodetection of Raman backscattered photons, followed by electrical amplification, electrical low-pass filtering, and sampling by ADCs. R-OTDR has the same spatial resolution as (4) for Rayleigh-based OTDR.

SpRS can be analyzed as a three-level system [142]. Let the peak power of the probe pulse evolve as $P_p(z) = P_{p0} g(z)$, where P_{p0} is the pulse peak power at launch, and $g(z) = \exp(-\int_0^z \alpha(z') dz')$ is the loss experienced by the probe pulse duration forward propagation, with $\alpha(z)$ being the fiber's attenuation at the probe wavelength. If $\alpha_s(z)$ and $\alpha_{as}(z)$ are the fiber's attenuations at the Stokes and anti-Stokes frequencies, the fiber segment at position z at the temperature $T_e(z)$ will generate Raman backscattered

light with powers of [143]

$$P_s(z) = K_s \frac{P_{p0}}{1 - \exp\left(-\frac{hf_R}{k_B T_e(z)}\right)} g(z) g_s(z) \quad (31a)$$

$$P_{as}(z) = K_{as} \frac{P_{p0}\exp\left(-\frac{hf_R}{k_B T_e(z)}\right)}{1 - \exp\left(-\frac{hf_R}{k_B T_e(z)}\right)} g(z) g_{as}(z) \quad (31b)$$

where h is Planck's constant, f_R is the Raman frequency shift, k_B is Boltzmann's constant, K_s and K_{as} are fitting constants, and $g_s(z) = \exp(-\int_0^z \alpha_s(z')dz')$ and $g_{as}(z) = \exp(-\int_0^z \alpha_{as}(z')dz')$ account for the loss experienced by the backscatter on the return trip to the sensing receiver.

Note $P_{as}(z)$ alone is temperature-dependent and can serve as a temperature sensor. However, measuring $P_{as}(z)$ in isolation is susceptible to power fluctuations of in P_{p0}. Moreover, the exact loss profiles $\alpha(z)$, $\alpha_s(z)$, and $\alpha_{as}(z)$ may be unknown due to losses from splices, connectors, and fiber bends. To improve accuracy, it is common to normalize the anti-Stokes power measurement with either the power of the Raman stokes backscatter [41] or the Rayleigh backscatter $P_r(z)$, which is temperature-independent [42], [144]

$$P_r(z) = K_r P_{p0} g^2(z). \quad (32)$$

Let the output of the receiver circuit in Fig. 13 be $I_s(z) = \eta_s P_s(z)$, $I_{as}(z) = \eta_{as} P_{as}(z)$, and $I_r(z) = \eta_r P_r(z)$, where η_s, η_{as}, and η_r are the detector efficiencies at the Raman Stokes, Raman anti-Stokes, and Rayleigh frequencies, respectively. When $I_s(z)$ is used to normalize $I_{as}(z)$, the ratio between (31a) and (31b) can be inverted to yield [145]

$$T_e(z) = \frac{C_1}{\ln\left(\frac{I_s(z)}{I_{as}(z)}\right) + C_2 + \int_0^z (\alpha_s(z') - \alpha_{as}(z')) dz'} \quad (33)$$

where $C_1 = hf_R/k_B$ and $C_2 = \ln(\eta_{as} K_{as}/\eta_s K_s)$ are fitting constants that can be obtained during calibration. Alternatively, if $I_r(z)$ is used to normalize $I_{as}(z)$

$$T_e(z) = \frac{C_1}{\ln\left(1 + \frac{I_r(z)}{I_{as}(z)}\exp\left(C_3 + \int_0^z (\alpha(z') - \alpha_{as}(z')) dz'\right)\right)} \quad (34)$$

where $C_3 = \ln(\eta_{as} K_{as}/\eta_r K_r)$. Lumped losses along the fiber cable arising from splices, connectors, and bends are typically wavelength-independent and are canceled in (33) and (34). However, accurate temperature measurement still requires correct compensation of WDL of the fiber. WDL may vary over time due to fiber degradation (e.g., hydrogen ingress [146]) or change in external conditions, requiring periodic calibration and compensation of WDL over long periods of operation. Alternative
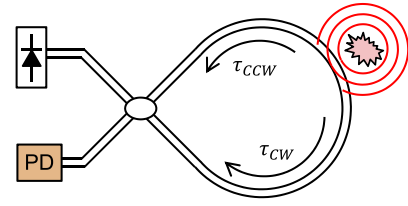

Fig. 14. *Vibration detection using a Sagnac interferometer.*

approaches, such as using a double-end configuration [147], a double-ended configuration with anti-Stokes power measurement only [148], and a multiwavelength configuration [149], have been proposed to improve robustness against time-varying WDL.

SpRS is the weakest of the three scattering processes. The powers at the Stokes and anti-Stokes frequencies are typically 20 and 30 dB weaker than Rayleigh scattering, respectively [126]. Just as with B-OTDR, temporal averaging is required to realize good temperature estimation accuracy. The intensity coding methods used in B-OTDR and B-OTDA can also be applied to R-OTDR to increase SNR by the coding gain. Examples using Simplex and cyclic codes can be found in [77], [144], and [150].

F. DFOS Based on Forward Transmission

The DFOS methods introduced in Sections II-B–II-E were based on the measurement of backscatter, which has the advantage of good spatial resolution, but the disadvantage is that backscatter is weak. An alternative class of DFOS methods is based on forward transmission. The higher received power enables higher optical SNR and potentially longer sensing range. Forward transmission-based sensing was first proposed in the context of a Sagnac interferometer shown in Fig. 14 [151].

Suppose that a point source vibration induces an optical phase of $\delta\phi(t)$ at a location on the Sagnac interferometer where the CW and CCW propagation delays are τ_{CW} and τ_{CCW}, respectively. The photodetector output is approximately proportional to the phase difference between the CW and CCW signals, which is

$$\Delta\theta(t) = \delta\phi(t - \tau_{CW}) + \delta\phi(t - \tau_{CCW})$$
$$\approx (\tau_{CCW} - \tau_{CW}) \frac{d\delta\phi}{dt}. \quad (35)$$

If $\delta\phi(t)$ can be measured independently, say by interfering one of the outputs of the interferometer with a reference source, the delay difference $\tau_{CCW} - \tau_{CW}$ can be inferred, from which the position of the vibration can also be estimated. This method was further refined in [152] and [153].

1) Forward Transmission Method Based on Measurement of Optical Phase: Recently, the optical phase measurement method based on forward transmission was revisited in
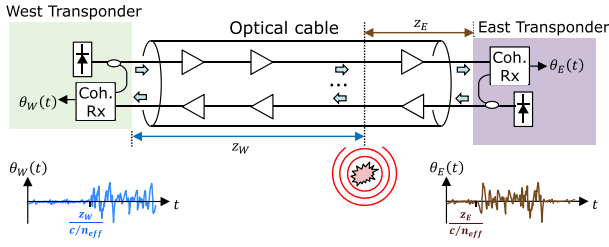
This article has been accepted for inclusion in a future issue of this journal. Content is final as presented, with the exception of pagination.

Ip *et al.*: Using Global Existing Fiber Networks for Environmental Sensing

Fig. 15. *Vibration detection using the bidirectional forward transmission. When a point source vibration event occurs, each receiver will measure an interferometric phase above the ambient noise level. Correlating the phases measured by each receiver enables the estimation of the vibration's position.*

the context of a bidirectional link shown in Fig. 15 [95], [96], [97]. Inside the cable are two fibers. In one of the fibers, the East (E) transponder transmits an unmodulated c.w. laser. At the other end of the cable, the signal is coherently detected by the West (W) transponder using its laser as LO. In the other fiber, this is replicated with the West transponder sending c.w. to the East transponder. Suppose that the signals transmitted by the East and West transponders are $x_E(t) = (P_E)^{1/2} e^{j(2\pi f_E t + \phi_E(t))}$ and $x_W(t) = (P_W)^{1/2} e^{j(2\pi f_W t + \phi_W(t))}$, where $f_{E/W}$ and $\phi_{E/W}(t)$ are their respective optical frequencies and PNs, and $P_{E/W}$ are their respective launch powers. Let the one-way propagation delay of the FUT be $T_L = L/(c/n_{\text{eff}})$. If a vibration event is well-modeled as a point source, and z_E and z_W are the respective distances from each transponder to the point in the FUT closest to the vibration source, then $\tau_E = z_E/(c/n_{\text{eff}})$ and $\tau_W = z_W/(c/n_{\text{eff}})$ are the respective delays. The interferometric signals obtained at each receiver will have phases of

$$\theta_E(t) = 2\pi(f_W - f_E)t + (\phi_W(t - T_L) - \phi_E(t))$$
$$+ \delta\phi(t - \tau_E) + \phi_{\text{AWGN},E}(t) \quad (36a)$$
$$\theta_W(t) = 2\pi(f_E - f_W)t + (\phi_E(t - T_L) - \phi_W(t))$$
$$+ \delta\phi(t - \tau_W) + \phi_{\text{AWGN},W}(t) \quad (36b)$$

where $\delta\phi(t)$ is the vibration-induced phase of interest, and $\phi_{\text{AWGN},E/W}(t)$ are the PNs at each receiver due to all the AWGN sources in the link, including ASE of inline amplifiers and receiver noise. Equations (36a) and (36b) have the same form as (12) for ϕ-OTDR, except that $\delta\phi(t)$ is now the accumulated vibration-induced phase along the whole link, the PN term is the phase difference between E and W lasers, and there is an additional term in case of a frequency offset between the lasers. The condition for vibration detection can once again be analyzed as in Fig. 7. Due to heterodyning, the PSD of PN is

$$S_{\phi_{\text{PN}}\phi_{\text{PN}}}(f) = [S_{\nu\nu,E}(f) + S_{\nu\nu,W}(f)]/f^2 \quad (37)$$

where $S_{\nu\nu,E}(f)$ and $S_{\nu\nu,W}(f)$ are the frequency noise spectra of the E and W lasers, respectively.

As with ϕ-OTDR, the interferometric phases in (36a) and (36b) are typically passed through an optimized band-pass filter, followed by thresholding, or more sophisticated ML methods can be used to detect and classify vibration events. After bandpass-filtering $\theta(t) \xrightarrow{\text{BPF}} \theta'(t)$, the position of the vibration can be estimated by taking the correlation between $\theta'_E(t) \sim \delta\phi'(t - \tau_E)$ and $\theta'_W(t) \sim \delta\phi'(t - \tau_W)$, which will have a peak at $\Delta\tau = \tau_E - \tau_W$. Since $z_E + z_W = L$, the position of the vibration can be deduced as $z_E = (1/2)(L + (c/n_{\text{eff}})\Delta\tau)$ and $z_W = (1/2)(L - (c/n_{\text{eff}})\Delta\tau)$, respectively.

2) Forward Transmission Method Based on Measurement of SOP: Another forward-transmission method that has been proposed is based on the measurement of the SOP. It has long been known that lightning strikes can cause fast SOP rotation, which can result in the adaptive equalizers in coherent transponders becoming unlocked, resulting in burst errors [154]. A study conducted in [155] was able to correlate fast polarization events with known lightning strikes and found that lightning can induce angular velocities up to 5 Mrad/s on the Poincaré sphere in OPGW aerial cables. Such large bandwidth potentially enables accurate localization of lightning events using a time-of-flight difference method similar to that described above for optical phase detection, except here, the start time of the event is defined as the onset of fast polarization changes. Recently, this method has also been used for seismic detection [99].

In contrast to the optical phase method, which measures the change in polarization-averaged pathlength induced by the environment, SOP is a measure of the relative phase between signal polarizations arising from birefringence and is insensitive to laser PN. One way to obtain the SOP vector $\mathbf{S}[m] = [S_1[m] \quad S_2[m] \quad S_3[m]]^T$ as a function of the time index m is to transmit a c.w. signal and measure the Jones vector of the received signal

$$\mathbf{y}[m] = \begin{bmatrix} y_1[m] \\ y_2[m] \end{bmatrix}.$$

The three components of SOP can be calculated using

$$S_1[m] = |y_1[m]|^2 - |y_2[m]|^2 \quad (38a)$$
$$S_2[m] = 2\text{Re}\{y_1[m]y_2^*[m]\} \quad (38b)$$
$$S_3[m] = 2\text{Im}\{y_1[m]y_2^*[m]\}. \quad (38c)$$

Alternatively, a data-modulated signal can be transmitted, and SOP is extracted from the weights of the time-domain equalizer (TDE) in the coherent transponder. Suppose that the TDE at the mth time index is

$$\mathbf{w}^{(m)} = \begin{bmatrix} \mathbf{w}_{11,n}^{(m)} & \mathbf{w}_{12,n}^{(m)} \\ \mathbf{w}_{21,n}^{(m)} & \mathbf{w}_{22,n}^{(m)} \end{bmatrix}$$

where each $\mathbf{w}_{ij,n}^{(m)}$ is a vector of length N_{eq} which is the memory length of the equalizer. Since the TDE rotates the signal back to the reference transmitted polarizations, taking the time-average of the weights yields its dc value, which is the inverse of the channel's Jones matrix:

$$
\mathbf{W}^{(m)} = \begin{bmatrix} \sum_n \mathbf{w}_{11,n}^{(m)} & \sum_n \mathbf{w}_{12,n}^{(m)} \\ \sum_n \mathbf{w}_{21,n}^{(m)} & \sum_n \mathbf{w}_{22,n}^{(m)} \end{bmatrix}.
$$

Either column of $\mathbf{W}^{(m)}$ is equivalent to $\mathbf{y}[m]$, from which SOP can be calculated.

SOP fluctuations induced by the environment are a random walk on the surface of the Poincaré sphere. It was shown in [100] that every fiber segment contributes an isotropically distributed random vector $\Delta\mathbf{s}_z$, and the variance of its length is proportional to the product between the variance of PMD in that segment, $\langle\tau^2(z)\rangle$, and the square of the local strain $\epsilon(z)$ in that segment. End-to-end SOP change is then given by the integral

$$
\langle \Delta\mathbf{s}^2 \rangle = \frac{\pi}{4}\left(\frac{2\pi c}{\lambda}\right)^2 \int_0^z \langle \tau^2(z) \rangle \epsilon^2\left(z'\right) dz'. \tag{39}
$$

The square dependence on local strain inside the integral means that positive and negative strains excited by a pressure wave at different locations of the fiber do not average out to zero, as might be the case with optical phase measurement. It was, thus, argued that SOP measurement can serve as a complementary tool to optical phase measurement [100].

III. MONITORING GEOHAZARDS WITH DISTRIBUTED SENSING

Optical fiber cables are commonly deployed along transportation infrastructures as part of the owner/operator backbone. Fibers of the communication cable can be made available to improve the protection of the infrastructure against natural hazards by implementing a GTMS [31]. The GTMS makes use of the available fibers, comprises DFOS (DAS, DSS, and/or DTS) interrogators and a data analysis software layer, and aims to detect and locate the preliminary signs of all natural events that can threaten civilian infrastructure. In some cases, dedicated strain sensing cables can be laid in parallel to the telecom cable along the whole length of the infrastructure [158] or in specific sections where the geohazard risk is higher, and risk mitigation requires higher sensitivity [157]. In the latter case, the telecom cable is used to monitor temperature everywhere, detect large ground movements, and route the sensing signal to the dedicated strain sensing cables.

In this section, we show the detection and localization of three types of ground movement, which cover most of the cases encountered in practice, namely, *erosion*, *landslide*, and *subsidence*. Each of these ground movements produces

Table 1 Geohazards and Sensing Methods

Geohazard	Soil Strain Measurement DSS	Soil Strain Measurement DAS	Soil Temperature Measurement DTS
Erosion			X
Landslide — Assessment, creep, preliminary signs	X		
Landslide — Rock avalanche, mud flow	X	X	
Subsidence	X		

unique spatiotemporal signatures in temperature and/or strain that can be measured using the DTS, DAS, and DSS methods covered in Section II [156]. Table I summarizes the three natural hazards of interest and with which combination of DFOS techniques they can be apprehended. The DAS system used in this section is based on CP-OTDR, while both DTS and DSS are based on B-OTDA. B-OTDA is preferred for the applications described here as it can handle sensing lengths over 50 km while keeping the spatial resolution below 4 m [31]. B-OTDA also has better tolerance against an increase in fiber loss due to accelerated fiber aging resulting from natural hazards [157].

A. Soil Erosion Measurement Using DTS

Erosion is the removal of soil or rock under the action of waterflow, wind or glaciers, which transports the removed material to another location. This ground movement is best monitored using DTS, as cover material provides thermal insulation to the duct or pipeline carrying the optical cable. When surface material is removed in the vicinity of the fiber optic cable, the cable may become directly exposed to surface water or ambient temperature changes. Even if the cable is within an enclosure, water infiltration from flooding, and change in soil condition between frozen and thawed states will impact local soil temperature.

An example is shown in Fig. 16 for an erosion event that occurred on an optical cable buried along the ROW of a natural gas pipeline in Peru [158], [159], [160]. The route of this cable climbs the oriental slopes of the Andes. Fig. 17 shows a photograph of the ground condition around the temperature anomaly that was pinpointed by the GTMS, which was subsequently confirmed by visual inspection. A tension crack had developed in the ROW at this location, resulting in water infiltration following sudden rainfall. This water infiltration provoked a fast and significant temperature drop over a short segment of cable. Fig. 16(a) shows the time evolution of temperature for two fiber positions at the pothole (25, 265 m), and at 18 m away (25, 247 m). Following a sharp initial drop, the temperature is observed to increase exponentially back to its normal value as the surrounding soil dried out. Fig. 16(b) shows the spatial temperature profile measured on three different days. The water infiltration event impacted around 20 m of cable and is observed on May 16, 2016. These two figures show typical spatial and temporal signatures for erosion events over flat land that was also encountered along other pipelines.
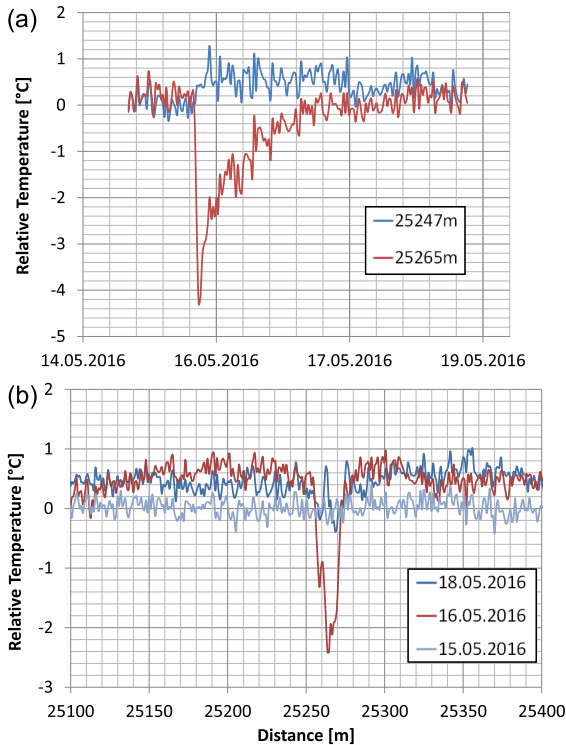
Fig. 16. *(a) Temporal and (b) spatial evolutions of temperature due to a water infiltration event caused by soil erosion [160].*
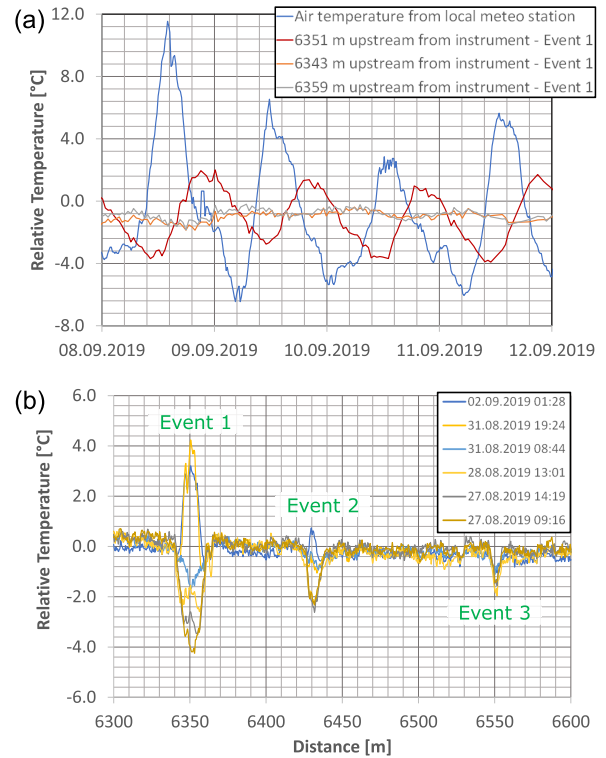

Fig. 18. *(a) Temperature variation measured with DTS compared with local meteorological data for Event 1. (b) Temperature profiles showing three temperature anomaly events caused by erosion [164], [165].*

Shallow water flowlines in Arctic conditions also suffer from erosion due to the pipeline acting as a heat source, which affects local soil characteristics. This can lead to the melting of the permafrost. The pipeline trench is then more prone to erosion or scouring by sea current or water streams flowing from shore. Cold water can then ingress into the naturally excavated trench and induce a cold spot that can be detected by the GTMS [161], [162], [163].

These erosion-associated temperature events are not isolated cases but are commonplace in most of the pipelines monitored so far using DTS. Similar behaviors have also

Fig. 17. *Photograph of the eroded surface which caused the water infiltration event in Fig. 16 [160].*

been reported in power cables, where temperature sensing can help assess soil coverage around the structure [163].

Another example where DTS assisted in the identification and characterization of eolian erosion was provided in [164] and [165]. The coastal section of the ROW of the Peruvian LNG pipeline does not suffer from geohazards caused by rainfall or flooding but is exposed to sand dune migration and eolian erosion. Fig. 18 shows examples of temporal and spatial temperature variations created by eolian erosion. Two features can be observed. First, temperature change has a periodicity of 24 h, but the temperature excursion measured by DTS for the buried cable is less than the temperature excursion of the ambient air measured at a nearby weather station. Second, the temporal profile of temperature variation at three points around Event 1 is delayed from the temperature variation of the ambient air due to the thermal insulation of the sand cover. A thermal model proposed in [164] and [165] allows the DoC to be estimated given the time lag Δt between the ambient temperature waveform and the temperature waveform measured by the DTS. The results are summarized in Table II, where Δt is taken as the time difference between the maximum of the ambient temperature waveform and the maximum measured by DTS at each fiber position. The estimated DoC ranges from

This article has been accepted for inclusion in a future issue of this journal. Content is final as presented, with the exception of pagination.

Ip *et al.*: Using Global Existing Fiber Networks for Environmental Sensing

Table 2 Analysis of Eolian Erosion Event Measured With DTS

	Event 1	Event 2	Event 3
Position	6350 m	6431 m	6551 m
Width	20 m	11 m	5 m
Δt	6 h 58 min	12 h 43 min	17 h 17min
DoC	0.14 m	0.25 m	0.34 m

14 to 34 cm for Events 1–3. The spatial extension of each eroded zone is also reported.

The two experimental examples above show the strength of combining DTS with thermal modeling. If the soil cover is more than 50 cm, the only detectable thermal changes are those caused by seasonal changes and water infiltration. In the latter case, the measured temperature returns slowly to that of the ambient soil after the soil dries out. If the soil cover is less than 50 cm, the measured temperature tracks diurnal changes, and DoC can be inferred from the observed time lag.

B. Measurement of Landslide Using DAS and DSS

Landslides are downward sloping movements of rock, soil, or both, occurring in the rupture of a surface, in which most of the material moves as a coherent or semicoherent mass, with small internal deformation [166]. Landslides can be in translation or rotation of soil material and include rock falls and mudflows. This type of ground movement can cause not only damage to buildings, or obstruct roads and railways, but can also induce permanent stress to the ground, deforming subterranean utilities, such as cables and pipes. The occurrence of rock fall can be detected using DAS, while longer term consequences can only be assessed by DSS measurements.

Fig. 19 shows a DAS measurement conducted at an avalanche test site in Switzerland in November 2020. A fiber optic cable was buried on a slope where avalanches are common. To simulate the short, intense strain produced by rockfalls, explosives were used, and the impact on the cable was monitored using DAS. Fifteen explosions with 230 g of explosive charge each were carried out at different positions left and right of the cable and at distances ranging from a few meters to 30 m from the cable. The DAS waterfall plot in Fig. 19(a) captures one such explosion. The strain pattern is observed twice as the slope was bisected by two fiber cables connected in a loop. Fig. 19(b) shows the strain waveform measured at 490 m. The event has a short time duration of around 1 s. After the initial vibration subsides, the DAS is unable to assess the permanent effects on the surrounding soil.

Permanent surface deformation can be assessed using DSS. An example is shown in Fig 20(a), where an event on October 22, 2010, caused a sudden increase in strain, and this elevated strain subsequently became permanent. The position and spatial extent of the event are clearly localized by DSS, as shown in Fig. 20(b). It was confirmed by site inspection that this event was caused by a rock fall on the ROW of the trans-Andean pipeline [158], [159], [167] (see Fig. 21).
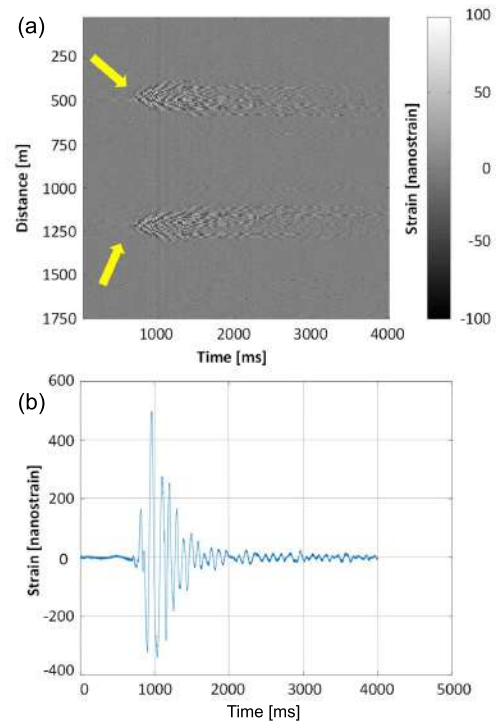

Fig. 19. *(a) DAS waterfall plot showing the impact of an explosion which is highlighted by the yellow arrows. The event is observed at two positions as the fiber layout is a loop. (b) Time series for strain measured at fiber position 490 m [158], [159], [167].*
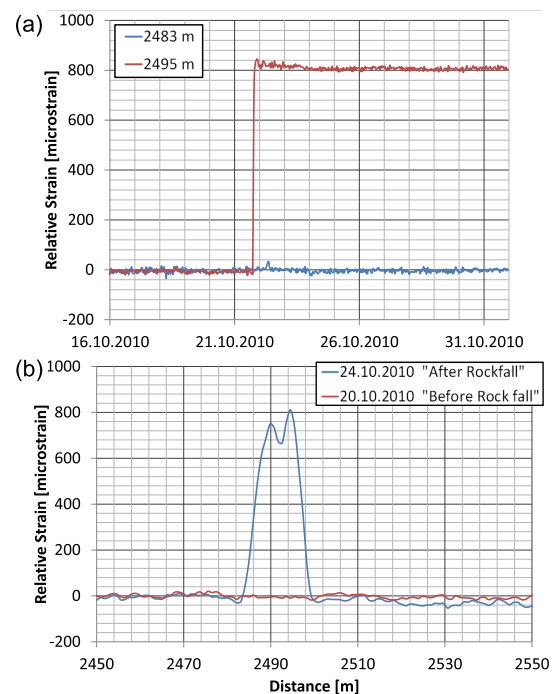

Fig. 20. *(a) Time evolution of strain for a rock fall event that provoked soil settlement and induced a permanent surface deformation. (b) Spatial profile of strain associated before and after the rock fall event [158], [159], [167].*

This article has been accepted for inclusion in a future issue of this journal. Content is final as presented, with the exception of pagination.

Ip *et al.*: Using Global Existing Fiber Networks for Environmental Sensing

Other types of landslides, such as slope failure, can also be detected using the DSS component of GTMS. Unlike rock fall events, which are characterized by a sudden jump in strain, slope failure events happen over a longer time scale, with strain building up gradually with time, making it difficult to detect with a DAS. Fig. 22 shows an example of an event that was recorded using DSS, and which was confirmed by site inspection (Fig. 23). The progressive development of a slope failure occurred between fiber positions 4500 and 4530 m, and the preliminary stage of this event was observed as a gradually increasing strain over a two-month period. Such time scales are incompatible with DAS methods. Fig. 22(b) shows that the cable segment impacted was around 30 m long. Measurement stopped on March 23, 2011, to allow remedial work to stabilize the ground. Similar events as shown have also been detected at other points along the same cable, and the spatiotemporal patterns recorded consistently showed strain gradually building up until slope rupture or remediation works were conducted [158], [159], [167]. In other pipeline projects crossing mountainous regions, slope failure events presenting similar features were observed and monitored.

C. Measurement of Soil Subsidence Using DSS

Ground subsidence consists of a terrain surface moving downward relative to the surrounding soils. This can be caused by the depletion of ground water reservoirs or by underground mining, limestone dissolution, and natural gas extraction.

We illustrate soil subsidence monitoring through the example of the settlement effect commonly seen in flat lands covered by swamps or at the bottom of valleys previously occupied by glaciers or lakes. By the mechanism of volume reduction or consolidation, the soil settles when a load is applied. The water content is moved away by the applied load pressure, and the phenomenon can be quantified by a vertical displacement.
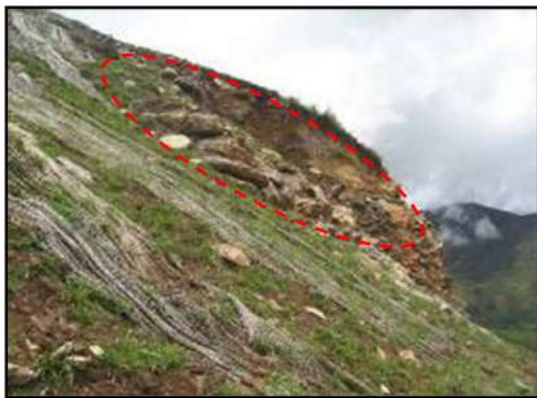

Fig. 21. *Photograph confirming the rock fall event detected at fiber position of 2490 m in Fig. 20(b) on a Peruvian LNG pipeline [158], [159], [167].*
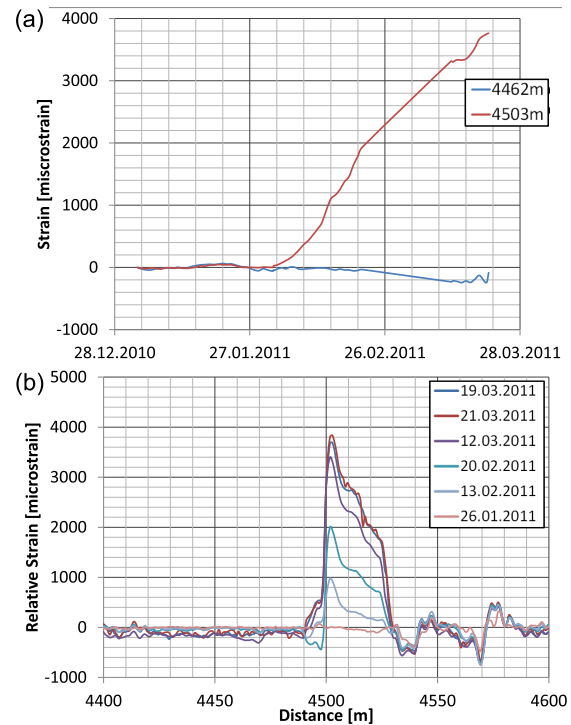

Fig. 22. *Detection of a slope failure at an early stage using DSS on the Peruvian LNG pipeline. (a) Time evolution of strain at two locations showing a gradual increase in strain over a two-month period. (b) Spatial strain profile measured on different dates during the observation period [158], [159], [167].*

The test setup was in the bed of former Lake Texcoco near Mexico City. The measurement was conducted during the summer of 2016, and the objective was to evaluate the use of the GTMS to monitor vertical displacement caused by buildings and construction in sites frequently exposed to consolidation. The SMC was laid at a depth of 50 cm. A TMC running in parallel allowed compensation for temperature effects. The length of the complete sensor was 90 m. To complement the fiber optic sensors, settlement plates were laid on the side of the trench at the level of the trench bottom. The movement of the plate is measured using a digital height measurement sensor. A section of the cable between 65 and 85 m was loaded with material to induce soil consolidation. The load consisted of layers of clay and tezontle, and generated a pressure of 2300 N/m^2. Fig. 24 shows the strain profiles measured before and after the application of the load. The strain profile that resulted from the load is not uniform but has tensile and compressive segments that were qualitatively confirmed by the simulation of Boussinesq's solution [168].

IV. TRAFFIC MONITORING AND CABLE THREAT PREVENTION

While DFOS methods can recover the spatiotemporal profiles of strain and temperature in an optical cable, ML is needed for higher level tasks, such as traffic counting,

This article has been accepted for inclusion in a future issue of this journal. Content is final as presented, with the exception of pagination.

Ip *et al.*: Using Global Existing Fiber Networks for Environmental Sensing

Fig. 23. *Photograph of the slope rupture confirmed by site inspection, which was detected by DSS on a Peruvian LNG pipeline [158], [159], [167].*

Fig. 25. *Flowchart of the Fiber-VTMA/Fiber-CS3 AI platform for simultaneous multipurpose sensing.*

vibration source classification, and cable threat identification. ML can be applied to data collected using any of the methods discussed in Section II and can be considered a back-end postprocessing operation independent of the DFOS method. The role of the DFOS front end is to collect large volumes of data to train the ML model. Although it is possible for a DFOS transponder to send the collected data to a central controller for processing and analysis, there is an advantage in having on-premise AI built into the DFOS transponder, as this minimizes the need to transfer and store data, and enhances data privacy.

A. Real-Time Simultaneous Multipurpose Sensing

An example of ML applied to simultaneous traffic monitoring and cable threat prevention was recently reported in [169]. Two AI modules, Fiber-VTMS and Fiber-CS3, were hosted on an edge AI platform. Fig. 25 shows a flowchart of the two-in-one system. Information is shared
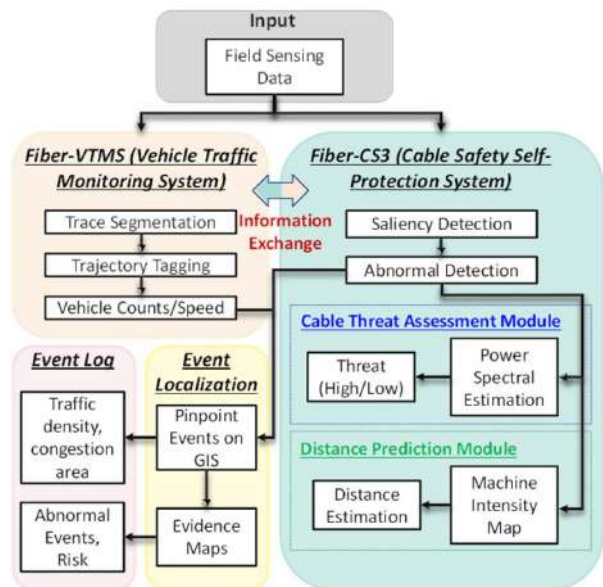

Fig. 24. *Strain profiles measured before (orange curve) and after (blue curve) the application of the load. Strain structure presents tension and compression components over the loaded section.*

between the Fiber-VTMS and Fiber-CS3 modules so that events detected by each system can be cross-referenced with events detected by the other before an alarm is triggered. This can reduce the probability of false alarms. For example, traffic jams detected by the Fiber-VTMS may be correlated with road construction detected using Fiber-CS3. Similarly, when a cable damage event occurs, it will be detected by Fiber-CS3, while Fiber-VTMS can provide information about who may be the responsible party. The GPS coordinates of the detected events can be pinpointed using a cable localization module described in [170].

1) Fiber-VTMS: Fiber-VTMS is based on TrafficNets, which adopts the U-Net architecture for precise segmentation of traffic traces from the fiber sensing image data and uses efficient graphics processing unit (GPU) computation. Details of this system can be found in [171]. Fig. 26(a) shows a typical traffic monitoring waterfall plot obtained with a DAS over a 4-min interval [18]. The brightness of a pixel corresponds to the vibration intensity at the fiber position and time indicated by the horizontal and vertical axes. Each bright line is a moving vehicle whose speed and direction can be determined by the inverse of its slope. Other information of interest, which may be extracted from a waterfall plot, includes traffic flow rate, traffic density, vehicle separation distance, and even the weight of individual vehicles. For example, the blue box in Fig. 26(a) shows an abnormally slow-moving vehicle, while the green box and the red box show regions of low and high traffic densities. Fiber-VTMS classifies the pixels on the waterfall image into two groups—traffic-related and nontraffic-related—for further analysis. Fig. 26(b) shows waterfall plots taken at the same location in regular traffic
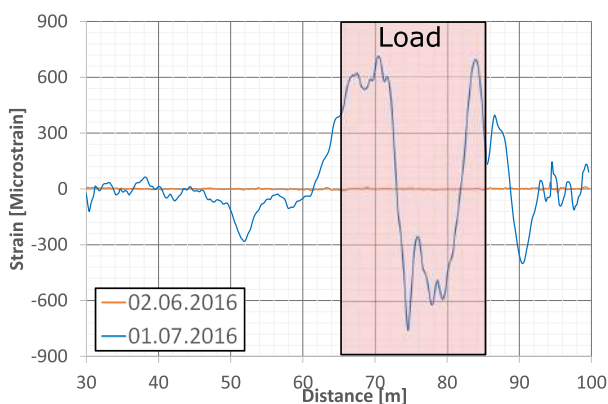
This article has been accepted for inclusion in a future issue of this journal. Content is final as presented, with the exception of pagination.

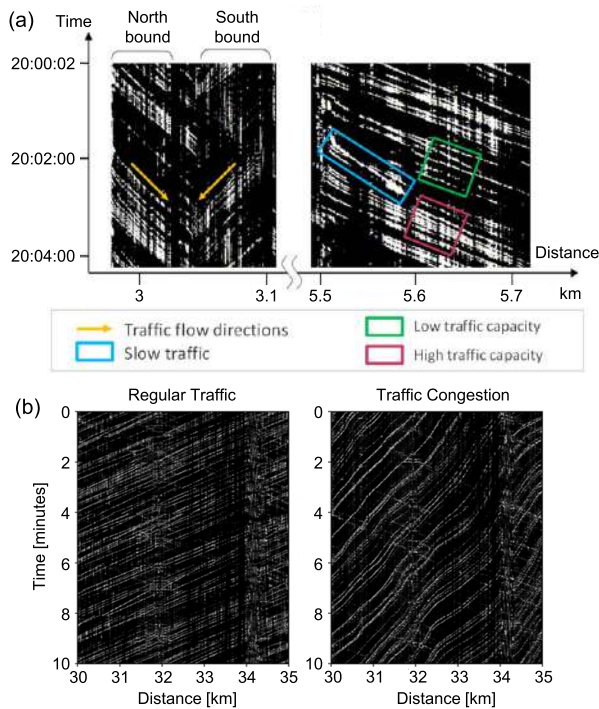Ip *et al.*: Using Global Existing Fiber Networks for Environmental Sensing

Fig. 26. *(a) Examples of traffic monitoring waterfall images recovered from DAS based on DD-OTDR. (b) Examples of regular and heavy traffic conditions [18].*

over a seven-month period from October 2020 to May 2021. The DAS had a spatial resolution of 1.6 m and a vibration sampling period of 120 ms. Fig. 27(a) shows an example of a traffic pattern measured over a 10-min window. The Fiber-VTMS AI extracted north- and south-bound vehicle trajectories from the waterfall image and colored their pixels red and white, respectively. Vehicle counts and estimated vehicle speeds are also provided by the system output [173]. Fig. 27(b) and (c) shows a summary of the monitored south-bound traffic entering the island. Vehic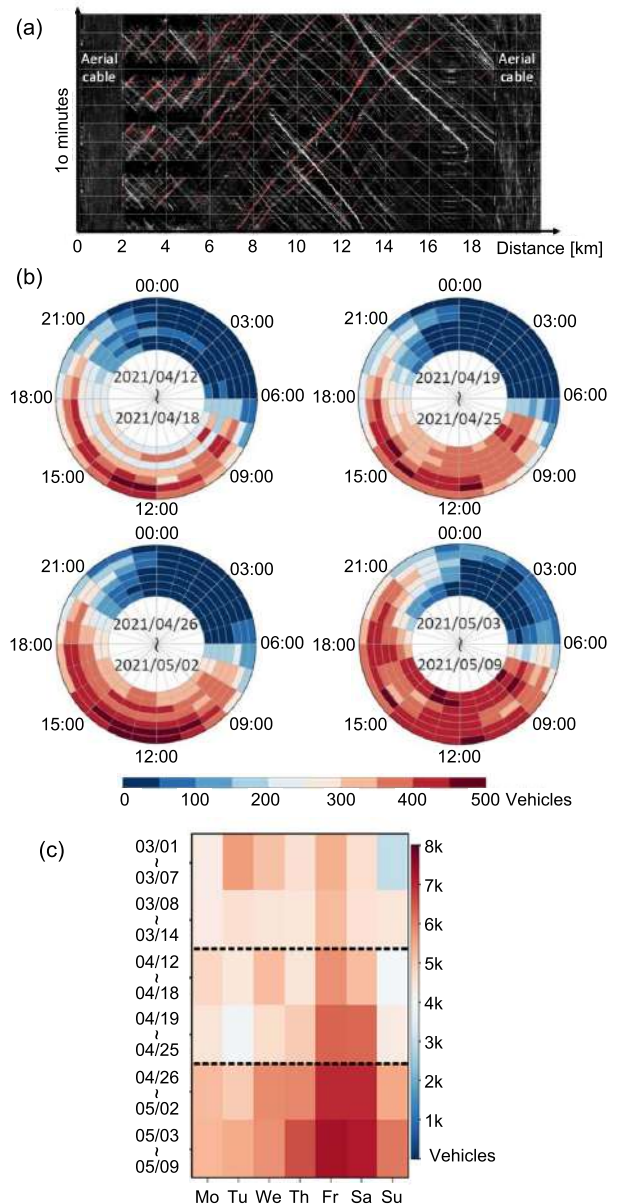les per hour are shown as radial-polar plots and during rush hour, showing distinct patterns that can be recognized by the AI.

2) Fiber-CS3: Fiber-CS3 takes traffic information from Fiber-VTMS and establishes location-specific thresholds for detecting nontraffic-related anomalies. Strong vibration points are first identified using a saliency detector, which is based on an adaptive threshold derived from whole route data. The points that cannot be attributed to vehicles by Fiber-VTMS are fed into Fiber-CS3. The dense spatiotemporal DAS data are, thus, reduced to a sparse format, so further identification of abnormal conditions can be conducted with low latency. The threat level of each detected abnormal event is further assessed using time–frequency representations [172]. A high-level summary of events identified is stored in an event log for future analysis.

B. Field Trial Over an Existing Telecom Cable

A field trial using the Fiber-VTMS/Fiber-CS3 platform was conducted over a carrier 5G network in Long Beach Island (LBI) in New Jersey, USA. The monitored cable was 21 km long, consisting of aerial sections between 0 and 2 km, and 19 and 21 km [see Fig. 27(a)], while the remainder of the cable from 2 to 19 km is buried below ground at a depth of between 1 and 1.5 m. Vibration data were collected with a real-time DAS module based on DD-OTDR, which continuously monitored the cable

Fig. 27. *(a) Example of a traffic monitoring waterfall image after vehicles were identified by Fiber-VTMS and the pixel of their trajectories are colored. (b) Hourly (Monday innermost ring, Sunday outermost ring) and (c) daily vehicle counts reported by Fiber-VTMS [169].*

where each angular slice represents an hour during the day, and each radial slice represents a day of the week (Monday is innermost and Sunday outermost). During the four-week period, there was a consistent rush hour period centered around 12 P.M. It is observed that the rush hour duration lengthened over the course of the monitoring period, as warming weather resulted in more people visiting the beach after 7 P.M. Fig. 27(c) shows daily vehicle count from March to May, with higher numbers observed in Fridays and Saturdays during late spring.

Long-term field monitoring results using Fiber-CS3 are shown in Fig. 28. The AI assigned "abnormality scores" to nontraffic-related vibration events of interest. Higher scores indicate a higher risk to the cable. The Fiber-CS3 assesses events on both aerial and buried cables. Fig. 28(a) shows the detected events on an "evidence map." Events associated with road construction, aerial cable anomalies, and field experiments are shown as blue, red, and green ovals, respectively. The abnormality score of each event is indicated by the size and brightness of the oval, with larger, darker ovals corresponding to higher risk.

It was shown in [172] that the cable threat level can be assessed using a frequency-attenuation discriminator, and the method is validated here against construction work depicted as Events b and c. In the vibration spectra measured for these events shown in Fig. 28(b) and (c), it is observed that Event b has amplitude peaks at higher frequencies (55, 80, and 110 Hz and so on) than the amplitude peaks of Event c. Moreover, three impulses indicated by bright horizontal lines are observed at 12:59:32, 13:09:37, and 14:32:15 for Event b. The threat assessment module assigned a higher abnormality score to this event. It was verified by visual inspection that this was caused by an excavator situated less than 3 m from the buried cable [see Fig. 28(b)–(i)], while, in Event c, the excavator was 100 m from the cable. Fig. 28(d) shows another Event d where a construction accident resulted in a utility pole falling on the monitored aerial cable (at 14:30:21 on May 4). The abnormality score shown in Fig. 28(a) assigned a high risk to this event, as it may lead to a cable cut. With DFOS and real-time AI, such events can be identified and reported to the carrier. Rapid risk assessment and fault identification may help avoid cable damage and reduce network downtime. Other low-risk events were also detected by the AI, such as Events g and h. These were caused by asphalt paving machines 8 m away from the cable moving parallel with the cable. External information, such as work hours and roadwork locations, can also be provided to the AI to improve its accuracy of risk assessment.

A pilot study was also conducted to estimate the distance between a vibration source and the cable. This field experiment is depicted as Event e in Fig. 28(a). A jackhammer was used in the vicinity of the buried cable, and the distance between the jackhammer and the cable was swept from 1.8 to 11 m at a 0.9-m interval. The field experimental setup is shown in Fig. 28(e)–(i). A model based on the joint
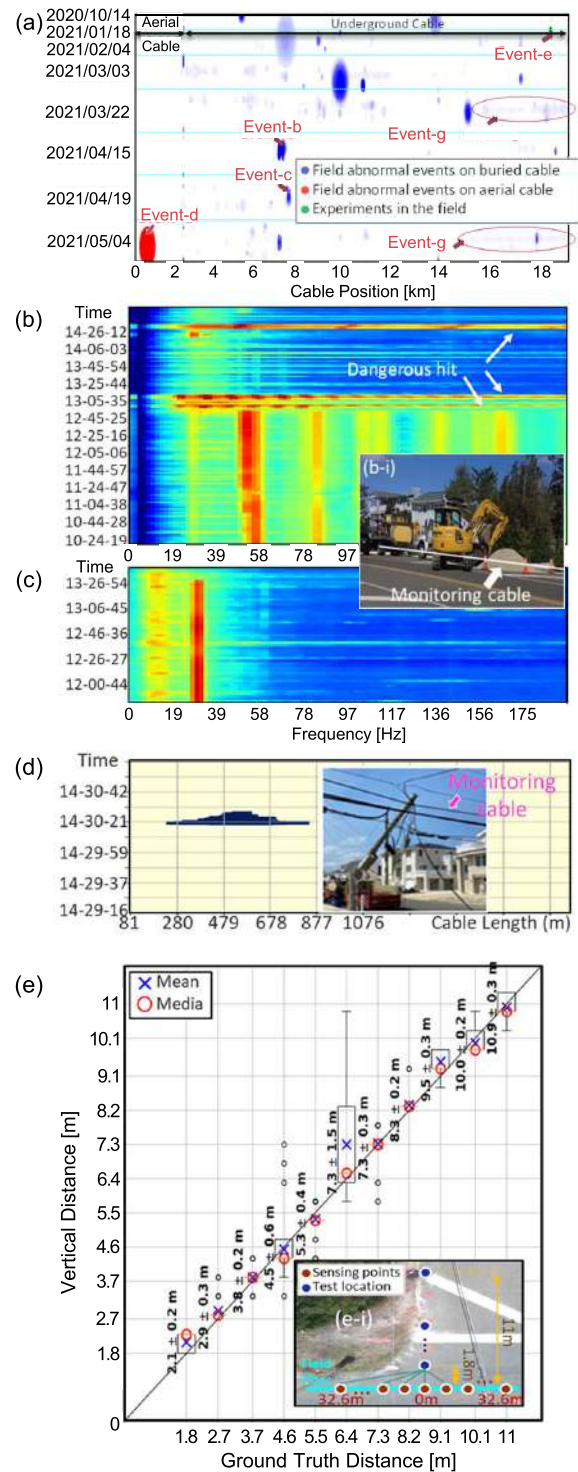

Fig. 28. *(a) Evidence map produced by Fiber-CS3 that reports nontraffic-related events. (b) and (c) Time–frequency plot of strain measured by the DAS for Events b and c. (d) Excess strain measured due to a fallen utility pole on an aerial cable. (e) Vibration intensity versus distance measured in a pilot study where a jackhammer was used in the vicinity of the buried cable [169].*

probability distribution between distance and vibration intensity was developed. Fig. 28(e) shows the performance
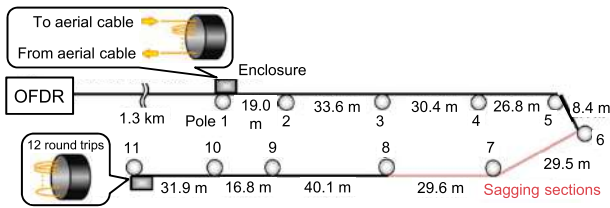
This article has been accepted for inclusion in a future issue of this journal. Content is final as presented, with the exception of pagination.

Ip *et al.*: Using Global Existing Fiber Networks for Environmental Sensing

Fig. 29. *Setup of the field experiment monitoring the deployment condition of an aerial cable. Distances between utility poles are shown [117].*

of the model at predicting distances. The root mean square prediction error across the full range of distances tested was 0.54 m.

V. DISTRIBUTED ACOUSTIC SENSING BASED ON OFDR

In this section, we review the use of OFDR for monitoring static strain in aerial fiber optic cables. The spatiotemporal strain data can be used to infer the condition of the cable and pinpoint abnormal events without time-consuming manual inspection of the whole fiber cable, thereby facilitating network maintenance.

Fig. 29 shows the field experimental setup for interrogating a deployed cable, which comprises of a 1.35-km underground section, followed by a 266.1-m aerial cable suspended on 11 utility poles. The aerial cable contains 12 fiber pairs (24 fibers in total). These fibers are spliced end-to-end to create 12 roundtrips through the suspended cable. Fusion splices are housed in fiber enclosures mounted on poles 1 and 11. Including the fiber drops at each end, the aerial section is approximately $24 \times 273 = 6552$ m long. Two aerial spans between utility poles 6 and 8 were sagging compared with the other spans. The sag-to-span-length ratio was $\sim 1.0 \times 10^{-1}$ for the two sagging spans and $< 1.0 \times 10^{-2}$ for all other spans. At the OFDR transponder, a 10-km delay fiber allowed the interrogation of a fiber section centered at 5 km from the transponder. The wind speed at the time of measurement was 2.7 m/s. The OFDR module operated with a chirp width of 111 MHz (spatial resolution of 93 cm) and a chirp repetition rate of 200 Hz (vibration sampling period of 5 ms). The receiver bandwidth was 350 MHz.

Fig. 30 shows optical frequency shift versus time for the fiber section between 500 and 2500 m (measured without the delay fiber at the OFDR transponder). Comparing the excursion in optical frequency shift between underground and aerial sections, it is observed that there is less frequency shift in the underground section. This is due to optical frequency shift being sensitive not only to strain but also to temperature. The slowly varying frequency shift in the aerial section is caused by a change in temperature. This is expected as temperature should be more stable in a buried cable than in an aerial cable exposed to sunlight and the ambient environment. To remove temperature

fluctuation's contribution to frequency shift, a high-pass filter with a cutoff frequency of 1.3 Hz was applied to the data. The relationship between optical frequency shift ν with strain ε and temperature ΔT_e is given by $(\Delta\nu/\nu) = -0.78\varepsilon - 6.92 \times 10^{-6}\Delta T_e$ in (23) [103], where $\nu = 193.5$ THz is the center frequency of the frequency-swept sensing signal. The conversion efficiency was 151 MHz/$\mu\varepsilon$ in this experiment. Fig. 31 shows the inferred dynamic strain distribution on the aerial cable. Lines of symmetry can be observed at distances of 4632, 4905, and 5178 m. This is due to the aerial cable being 273 m long; thus, the multiple passes of the chirped signal all interrogate the same environment surrounding the cable. The excellent symmetry, with a correlation of 88% between the strains measured by different passes, shows that vibration induces a similar strain to every fiber in the optical cable. The diagonal lines show the dynamic strain propagating along the cable. As the cable is fixed to utility poles, each segment between two poles sways independently of the other segments. The propagation speed of the vibration in each segment can be used to assess the cable condition in that segment.

It is observed that, around the lines of symmetry at 4632, 4905, and 5178 m, there is a stable region around 6–8 m long with no diagonal lines. These correspond to excess fiber inside fiber enclosures protecting the splice points at poles 1 and 11, and these fibers are isolated from the ambient environment.

After identifying the beginning and end of each cable segment in Fig. 31 (pole numbers are marked), a 2-D Fourier transform of the spatiotemporal strain profile was calculated for each segment to assess the dispersion characteristics of the vibration in that segment. As vibration propagation speed is related to cable tension, this will infer whether that cable segment is tight or sagging. Fig. 32 shows frequency versus wavenumber (f-k) spectra for: 1) a sagging span between poles 6 and 7 and 2) a normal nonsagging span between poles 8 and 9. Both spectra exhibit mirror symmetry. The dispersion characteristic is highlighted by the dotted white line. The dispersion characteristics with positive and negative slopes correspond to vibration propagating forward and backward along the cable, respectively, while the slope infers the propagation speed, which was estimated to be 19.1 and 41.2 m/s for sagging and nonsagging spans, respectively. The large difference in propagation speed and its dependence on the degree of sagging can be exploited by a cable monitoring tool. These results demonstrate that DVS based on OFDR is an attractive alternative to on-field visual inspection by human workers. The remote strain monitoring capability can potentially also allow the detection of ice accumulation, falling branches, and other abnormal conditions deemed hazardous to cable health. ML can classify abnormal events and trigger a warning to the network operator when a dangerous condition is encountered, while location information can also be provided to assist field maintenance.
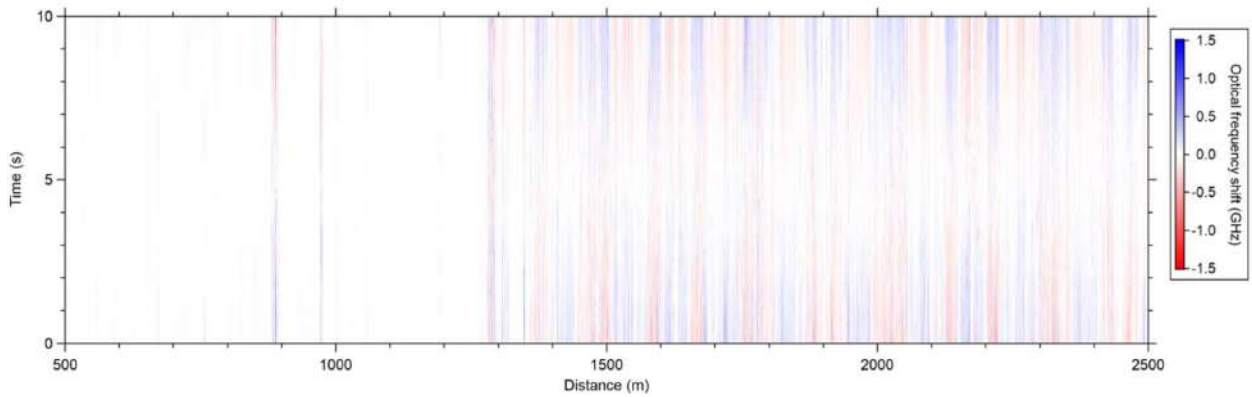
This article has been accepted for inclusion in a future issue of this journal. Content is final as presented, with the exception of pagination.

Ip *et al.*: Using Global Existing Fiber Networks for Environmental Sensing

Fig. 30. *Optical frequency shift distribution along the deployed optical fiber. Optical frequency shift caused by temperature fluctuation is dominant over that caused by strain fluctuation, while the temperature is more stable in the buried section (before 1300 m) than in the aerial section [103].*
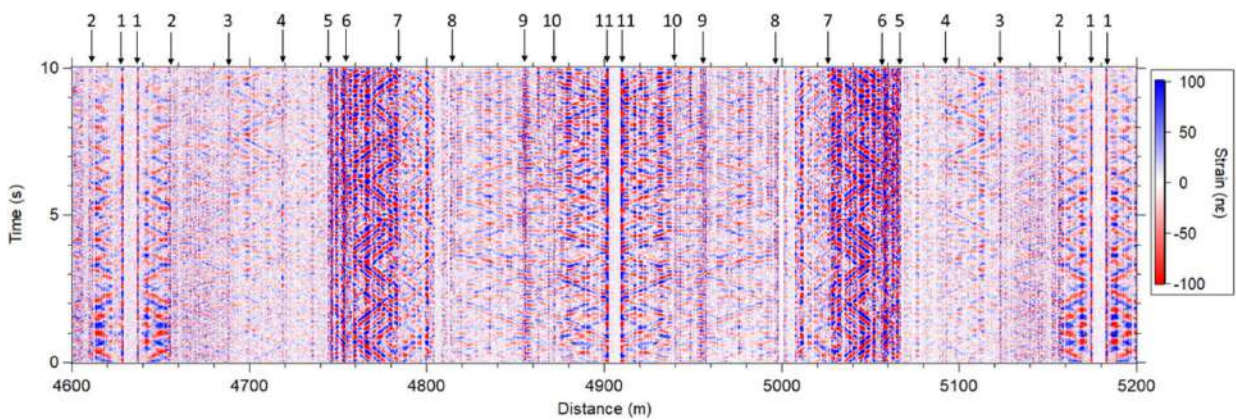

Fig. 31. *Dynamic strain distribution measured for the aerial optical cable. The numbers above the graph are the locations of the utility poles in Fig. 29. The color scale is intentionally saturated to better illustrate vibration behavior [103].*

VI. MONITORING OCEAN WAVES AND SEISMIC WAVES USING DD-CP-OTDR IN SUBMARINE CABLES

DD-CP-OTDR has attracted much interest in submarine seismology, as submarine cables on the ocean floor allow seismic measurement at locations where it is difficult to place conventional seismometers. DD-CP-OTDR can collect vibration measurements from a large number of sensing points. As these sensing points are also uniformly spaced at a fine spatial resolution, the Fourier analysis can discriminate different types of vibration by their propagation characteristics in the f-k domain. Such detailed analysis is often difficult using conventional point sensor arrays due to the large spatial granularity of the data, which results in spatial frequency aliasing, thus masking the dispersion signatures of certain waves of interest. Table III shows typical performance parameters achievable using DD-CP-OTDR. These numbers are well matched to typical requirements in seismology. A DD-CP-OTDR system with a 100-km range,
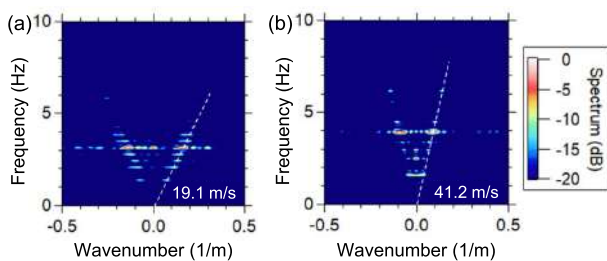

Fig. 32. *f-k spectra for (a) sagging and (b) nonsagging cable spans [117].*

Table 3 Typical Performance Parameters in DD-CP-OTDR

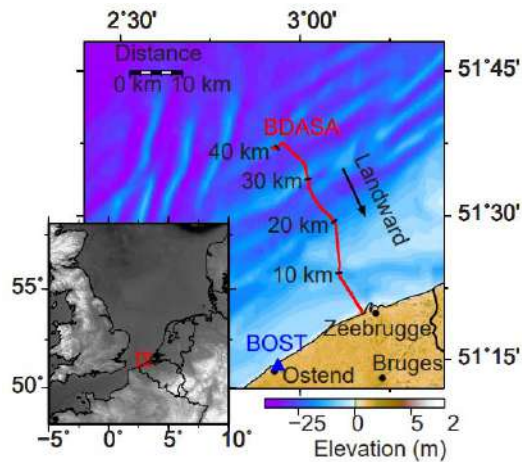| Range	100 km (assisted by Raman) [20]
Spatial resolution	5 to 10 m [20]
Measurand resolution	$3 \text{ p}\epsilon/\sqrt{\text{Hz}}$
Operation bandwidth	10^{-6} to tens of Hz (max. sampling rate is only limited by fiber length, 1 kHz for 100 km)
Detection bandwidth	1 GHz

Fig. 33. *Map showing the location of the Belgium DAS Array (BDASA) submarine cable in the North Sea [20].*

10-m spatial resolution, and good measurand resolution from 10^{-6} Hz to 1 kHz can characterize a vast range of wave motions of interest, allowing the determination of their direction, wavelength, frequency, velocity of propagation, and dispersion characteristics.

As an optical cable is a 1-D sensor, all propagation characteristics measured will be relative to the axis of the cable. The apparent velocity of a wave measured with DAS will differ from the true velocity by the cosine of the angle between the direction of the wave and the direction of the cable. Conducting DAS simultaneously over multiple cables at different orientations relative to the earth's surface can allow the direction and 2-D propagation characteristic of detected waves to be inferred. Another possibility is to use a zig-zagging cable with sections that are at different orientations.

A seismic experiment conducted using DD-CP-OTDR on a 41.92-km submarine cable offshore from Belgium is shown in Fig. 33. The DD-CP-OTDR module measured spatiotemporal strain variations $\epsilon(z,t)$ at a spatial resolution of 10 m (4192 sensing points) and at a vibration sampling rate of $R_p = 1$ kHz, which was then downsampled to 10 Hz to reduce dataset size for further processing. Copropagating Raman amplification was used to reduce power fluctuations of the received backscatter to less than 3 dB over the 42-km cable.

Upon taking the 2-D Fourier transform of $\epsilon(z,t)$, the f-k plot shown in Fig. 34 was obtained [20]. Two well-separated bands corresponding to the dispersion characteristics of ocean waves and seismic Scholte waves can be observed in Fig. 34(b), which replots the upper right quadrant of Fig. 34(a) in logarithmic scale. Ocean waves have frequencies ranging from 0.01 to 0.18 Hz, while seismic Scholte waves have frequencies ranging from 0.36 to 4 Hz. Their group velocities can be inferred by the inverse slope of their dispersion characteristics. Ocean waves propagate at up to ~20 m/s, while seismic

Scholte waves propagate at much higher velocities of up to ~1.5 km/s, which is nearly two orders of magnitude faster than ocean waves. This large difference between their apparent velocities demonstrates that they are of different physical origins, with one wave propagating through water and the other wave through the seafloor interface. The results in Fig. 34 also provided the first evidence of *in situ* microseism generation where a seismic "Scholte" wave is excited at the seafloor by a depth-invariant pressure term generated by opposing groups of ocean waves at double their frequency—a phenomenon described by the Longuet-Higgins theory of microseism generation [174]. This present study was able to show the phenomenon of microseism generation in greater detail than previous studies using conventional ocean-bottom point sensors, as point sensors are difficult to install in large numbers and costly to extract data from without optical fiber. Small network size means microseism direction, and intensity was previously measured at only a few points over relatively short distances, which led to poor spatial frequency
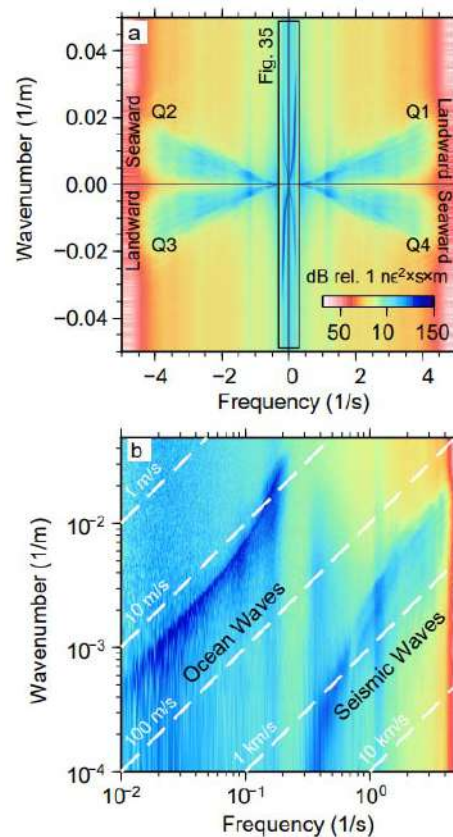

Fig. 34. *f-k spectrum based on 1 h of strain data measured on the 42-km BDASA cable. (a) Spectrum in linear scale showing the propagation of various landward and seaward waves. (b) Upper right quadrant of (a) in the logarithmic scale showing well-separated bands corresponding to the dispersion characteristics of ocean waves and seismic Scholte waves. The white lines indicate phase velocity contours (c = f/k) [20].*
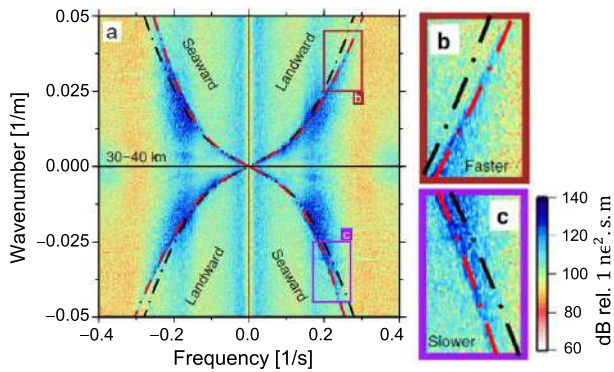
This article has been accepted for inclusion in a future issue of this journal. Content is final as presented, with the exception of pagination.

Ip *et al.*: Using Global Existing Fiber Networks for Environmental Sensing

Fig. 35. *f-k spectrum based on 10 min of strain data recovered from the fiber section between 30 and 40 km on the BDASA cable. (a) Spectrum in linear scale showing asymmetry between the dispersion curves for landward and seaward waves. Theoretical dispersion curves are plotted with (red) and without (black) the effects of an ocean current. The theoretical dispersion relation of ocean waves (angular frequency ω and angular wavenumber k) propagating in an ocean current of apparent velocity U is described by $(\omega - Uk)^2 = gktanh(kH)$, where g is gravitational acceleration and H is water depth. (b) and (c) Close-up views of the dispersion curves for landward and seaward waves, showing the best fit theoretical curve (red) corresponding to a landward current (therefore, faster apparent velocities for the landward waves) [20].*

resolution, rendering it difficult to discriminate different wave phenomena as clearly as in Fig. 34.

Another phenomenon revealed by the experiment is the difference in energy between landward and seaward ocean waves. This can be observed inside the box in Fig. 34(a) (an enlarged version is shown in Fig. 35), where the wave with a positive slope has a larger amplitude than the wave with a negative slope. Furthermore, f-k plots taken for different fiber sections (e.g., $20-30$ versus $30-40$ km) showed that the relative energy between seaward and landward ocean waves increases with distance from shore. This indicates that some of the seaward waves are reflections from a bathymetric ridge [20].

A closer examination of the seaward and landward ocean waves also reveals asymmetry in their dispersion characteristics. Fig. 35 reproduces the ocean waves in Fig. 34(a) at a higher resolution, where it is observed that landward-propagating waves have higher apparent velocities than seaward-propagating waves. Comparison between the measured f-k results with theoretical modeling allowed the determination that this asymmetry was caused by ocean currents with apparent velocities in the landward direction, which increased gradually from 0.1 to 0.5 m/s during the 1-h monitoring period. Note that an ocean current denotes continuous water flow without "wave-like" properties and is not directly observable by DAS if it does not generate pressure/strain gradients that propagate along the fiber cable.

An important feature in DD-CP-OTDR, which allows f-k processing, is its uniform measurand resolution along the entire fiber length [110]. This allows the raw amplitude

data to be processed without the need for denoising or smoothing to compensate for the signal at faded locations [21].

With the same datasets, ambient noise interferometry was performed on passive ocean-bottom DD-CP-OTDR recordings, which was shown to be a powerful tool for subsurface structural investigation [175]. The methodology is shown in Fig. 36 and is based on calculating the time-domain cross correlation $R_{\epsilon\epsilon}(z_j, t) = \text{corr}[\epsilon(z_i, t), \epsilon(z_j, t)]$ between the strain measured at fiber position z_i (32 km in this case) with strain measured at neighboring fiber positions z_j (30–34 km in this case). When a wave originating from infinitely far away propagates past the cable, the strain times series $\epsilon(z_i, t)$ and $\epsilon(z_j, t)$ will have a correlation peak at the delay $(z_j - z_i)/v_w$, where v_w is the wave's apparent velocity. This will be observed as a straight line passing through the center of the 2-D intensity plot of $R_{\epsilon\epsilon}(z_j, t)$ versus z_j and t. However, if a wave originated from a point source closest to the cable at the position z_o, at a perpendicular distance of d at this position, peak correlation will appear as a hyperbola at $\pm(d^2 + (z_j - z_o)^2)^{1/2}/v_w$. In the example shown in Fig. 36, there is a point source at 31 km, which generated secondary waves, indicating the presence of a scatterer. The shape of the hyperbola can be used to estimate both the position z_o closest to the source and its perpendicular distance d.

Another example of ocean floor vibration monitoring using DD-CP-OTDR was conducted on the CANALINK submarine cable in the Canary Islands and was reported in [176]. As shown in Fig. 37, the cable connected the islands of Tenerife (TF) and Gran Canaria (GC), reaching a maximum depth of 3570 m. Two DD-CP-OTDR modules were located at TF and GC, and each monitored ∼60 km of the cable from shore. Spatiotemporal strain variations $\epsilon(z, t)$ were measured at a spatial resolution of 10 m
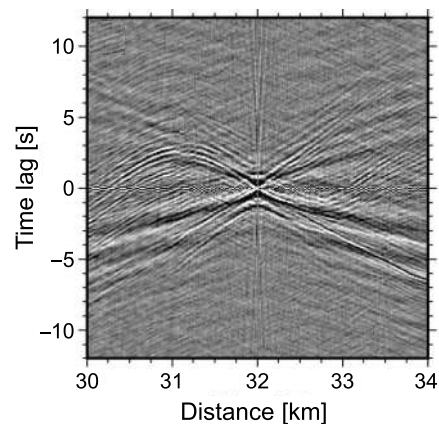

Fig. 36. *Cross correlation $R_{\epsilon\epsilon}(z_j, t)$ between the strain time series measured at $z_i = 32$ km with the time series of neighboring positions from 30 to 34 km along the BDASA cable. A hyperbola centered at 31 km is observed, indicating obliquely incident Scholte waves generated by a strong secondary source or scatterer [175].*
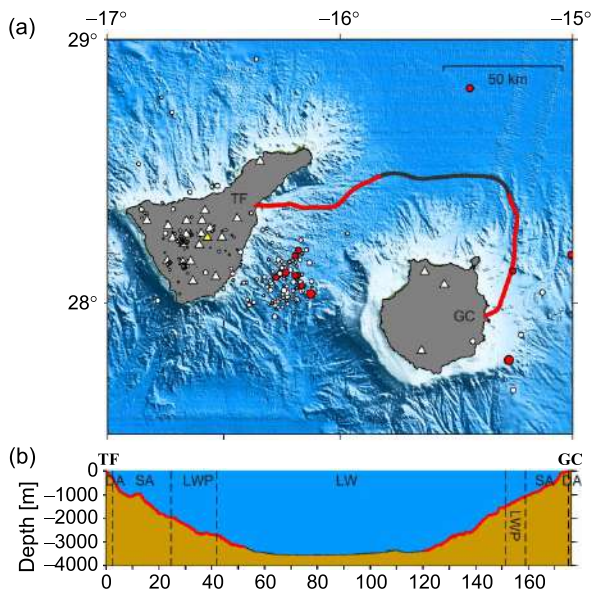
This article has been accepted for inclusion in a future issue of this journal. Content is final as presented, with the exception of pagination.

Ip *et al.*: Using Global Existing Fiber Networks for Environmental Sensing

Fig. 37. *(a) Map of the 176-km long CANALINK telecommunications cable connecting TF and GC. The first ∼60 km from each side (red lines) were monitored with two DD-CP-OTDR from July to September 2020. (b) Bathymetric profile of the cable, which reaches a maximum depth of 3570 m. Dashed vertical lines separate sections of lightweight (LW), lightweight-protected (LWP), single-armored (SA), and double-armored (DA) cables [176].*

Fig. 38. *Strain amplitude measured by DD-CP-OTDR at TF on September 18, 2020, showing the propagation of P-, S-, and T-waves due to an M_W 6.9 Mid-Atlantic Ridge earthquake that occurred around 3000 km away [176].*

(5984 sensing points) and a vibration sampling rate of $R_p = 1$ kHz. After downsampling to 50 Hz, a bandpass filter between 0.05 and 24 Hz was applied to the data to isolate the acoustic band of interest.

Hydroacoustic Tertiary (T) waves were observed for the first time using a DAS in this experiment. T-waves are generated by oceanic earthquakes. They propagate in the SOFAR channel, which is a horizontal layer of water in the ocean where guided acoustic waves at low frequencies propagate with low transmission loss. SOFAR has been the subject of several studies, including seismic ocean thermometry [177]. When a T-wave reaches the shore, it may transform into a seismic wave that occurs after the primary (P) and secondary (S) waves.

Fig. 38 shows the vibration amplitude time series measured by the DD-CP-OTDR at TF. Several waves resulted from an M_w 6.9 earthquake in the Mid-Atlantic Ridge that occurred on September 18, 2020, at a distance of around 3000 km from the cable. The reference position of 0 km is where the cable enters the water at TF, and negative values correspond to the terrestrial section of the cable.

Fig. 39(a) and (b) shows the radial and transversal vibration amplitude time series measured with a conventional land-based seismometer. Vibrations due to seismic P- and S-waves are labeled. In addition, there exists a hydrostatic T-wave with higher frequencies and lower amplitude, which is revealed in Fig. 39(c) by passing Fig. 39(a) through a high-pass filter with a cutoff frequency of 1 Hz. Fig. 39(d) shows the vibration measured at fiber
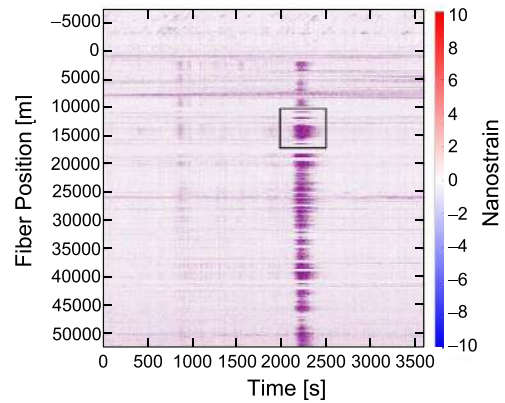
position 45 km using DD-CP-OTDR after bandpass filtering. Good agreement is observed with Fig. 39(c).

Hydroacoustic T-waves are more effectively recorded using ocean-bottom seismometers and hydrophone arrays than using coastal and island-based seismic stations. However, ocean-bottom seismometers and hydrophones have higher maintenance costs. This study demonstrates that DD-CP-OTDR over submarine telecommunications cables

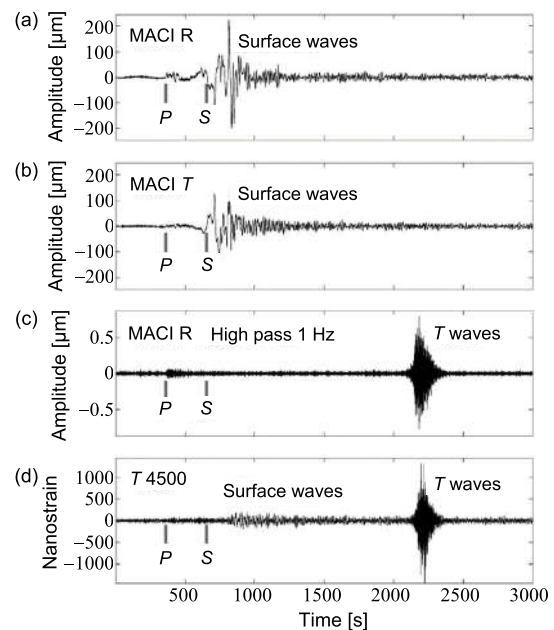**Fig. 39.** *Recordings of P-, S-, and T-waves following an M_w 6.9 Mid-Atlantic Ridge earthquake on September 18, 2020. (a) Radial and (b) transversal vibration amplitude measured using a seismometer at the MACI seismic station. (c) T-wave is revealed by passing (a) through a 1-Hz high-pass filter. (d) Strain time series measured using DD-CP-OTDR at 45 km from TF on the CANALINK cable [176].*
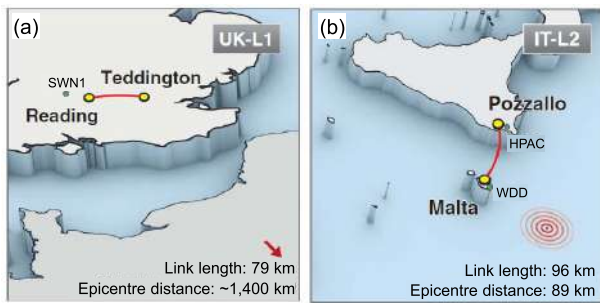
This article has been accepted for inclusion in a future issue of this journal. Content is final as presented, with the exception of pagination.

Ip *et al.*: Using Global Existing Fiber Networks for Environmental Sensing

Fig. 40. *Maps of two seismic detection experiments conducted using the accumulated optical phase measurement method for (a) terrestrial cable in the U.K. and (b) submarine cable in Italy. Reproduced from [95].*

Fig. 41. *Comparison between the optical phase measured on the 79-km terrestrial UK-L1 cable using the accumulated optical phase measurement method with the displacement measured using a seismometer in Swindon (GB.SWN1) for an M_W 6.5 earthquake in central Italy on October 30, 2016. Results are reproduced from [95].*

is a cheap and effective tool for the study of hydroacoustic energy propagation in remote oceanic regions [176].

A. Future Directions

Most DAS-based submarine seismic research to date has focused on the 0.01–100-Hz region. There has been a trend toward using DAS to study events at even lower frequencies associated with infragravity waves and tidal motion [178]. DAS experiments over month-long monitoring periods investigating long-term environmental fluctuations on this timescale have been demonstrated for chemical [179] and temperature monitoring [180]. It is expected that high-sensitivity seismic monitoring at similar timescales will be conducted in the future.

VII. DFOS BASED ON FORWARD TRANSMISSION

A. Optical Phase Measurement Using c.w. Signals

DFOS methods based on backscatter measurement have the disadvantage of round-trip propagation loss, as well as the inability to pass through inline amplifiers with circulators at their outputs. Methods such as DD-OTDR or ϕ-OTDR will require network architecture modifications to allow the backscatter to propagate back to the sensing transponder. The longest reach reported to date for Rayleigh-based DAS using chirped pulses on an unamplified span is only 171 km [75]. Recently, a new class of methods based on forward transmission was proposed. This work was inspired by long-distance atomic clock frequency transfer over optical fiber networks, where the cumulative effect of mechanical vibration-induced strain on the cable is a noise source detrimental to clock comparisons. A system that is sensitive enough to detect such phase perturbations can also be used as a sensor.

The accumulated optical phase measurement method was first demonstrated on terrestrial and submarine cables (Fig. 40) [95]. Results from two experiments demonstrating the efficacy of this method are shown in Figs. 41 and 42. In both experiments, a transponder injected a c.w. signal at one end of a fiber pair, which was
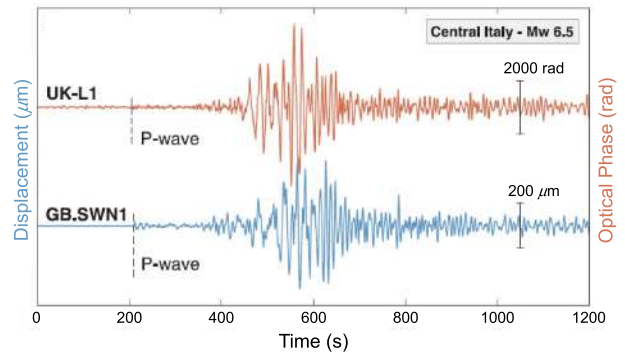
looped back at the far end, allowing delayed self-coherent detection by the receiver.

In the first experiment, an M_W 6.5 earthquake in Central Italy was detected on October 30, 2016, on a 79-km long UK-L1 fiber link connecting National Physical Laboratory (NPL) with a data center in Reading [Fig. 40(a)]. Fig. 41 shows a comparison between the accumulated optical phase measured using the interferometry method with the displacement measured using a conventional seismometer (GB.SWN1) located in Swindon less than 100 km away from NPL. Excellent correlation is observed between the two waveforms. The main sources of noise in the interferometry method are laser PN and ambient vibration induced by the environment integrated over the length of the cable. This is in contrast to DAS based on backscatter measurement, where ambient vibrations are only integrated over the gauge length. As UK-L1 is a
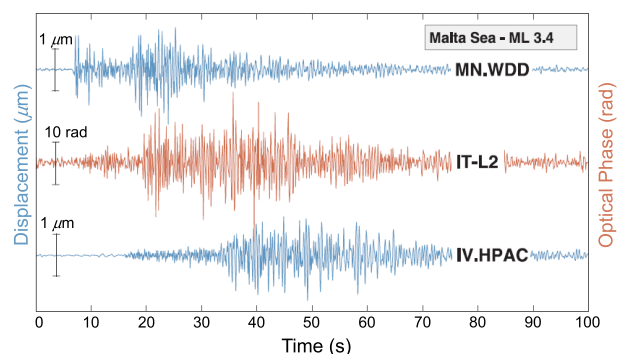
Fig. 42. *Comparison between the optical phase measured on the 96-km submarine IT-L2 cable using the accumulated optical phase measurement method with the displacement measured using conventional seismometers (MN.WDD and IV.HPAC) for an M_L 3.4 earthquake in the Malta Sea on September 2, 2017. A 1.5-Hz high-pass filter was applied to the optical signal to suppress strong environmental noise at 1 Hz. Results are reproduced from [95].*

This article has been accepted for inclusion in a future issue of this journal. Content is final as presented, with the exception of pagination.

Ip *et al.*: Using Global Existing Fiber Networks for Environmental Sensing

terrestrial cable, noise was primarily due to man-made sources and was in the same frequency range as earthquake signals. The laser in this measurement was phase locked to a hydrogen maser-referenced optical frequency comb and had frequency stability on the order of 10^{-13} at 1-s averaging time.

Another experiment with improved seismic sensitivity was conducted over an environmentally quieter 96.4-km long submarine cable (IT-L2) [Fig. 40(b)], using a laser locked to an ultralow expansion (ULE) glass Fabry–Perot cavity with frequency stability on the order of 10^{-15} at a few seconds of averaging time. Fig. 42 shows the detection of an M_L 3.4 earthquake on September 2, 2017, whose epicenter was 89 km from the cable in the Malta Sea. The seismic wave produced an optical phase excursion of only ~40-rad peak-to-peak but was still detectable owing to the low ambient noise of the sea floor. The waveforms measured using conventional seismometers near each end of the cable are also shown. The difference in the arrival times of the P-wave measured with each method is consistent with a wave propagation speed of ~5 km/s.

These results demonstrate the potential for seismic sensing using submarine cables. The ocean bottom is expected to be even quieter than the coastal IT-L2 cable, which experiences noise from shipping and wave motion. In addition, environmental noise is expected to accumulate noncoherently over long fiber cables, thus scaling as $(L)^{1/2}$ [181]. Even a 5000-km cable with the same environmental noise level as IT-L2 is expected to be only seven times noisier.

B. Optical Phase Measurement Using Data-Modulated Signals

Recently, it was recognized that there is no need to transmit dedicated c.w. signals over the fiber to measure optical phase, as optical phase is already tracked in digital coherent transponders by a combination of adaptive DSP operations, such as FOC, adaptive TDE, and CPR [62], [63], [97], [98]. Only a small overhead is required to provide the optical phase for sensing purposes, as the baud rate of telecom signal is tens of GHz, whereas the optical phase only needs to be sampled at hundreds of kHz to record even the fastest acoustic phenomenon realistically encountered in the real world. This opens the potential for telecom transponders to perform sensing as an auxiliary function, provided that appropriate changes are made, such as using more stable lasers and time synchronization through a common reference, such as GPS.

A field experiment was conducted using this method in [58] and [97]. Several real-world vibration events were detected and localized. These include hammer strikes against utility poles, and emulated intrusion, tampering, and construction scenarios. The 378.8-km link shown in Fig. 43 comprised of terrestrial cables, around 25% of which were aerial cables suspended on utility poles that were exposed to wind and air temperature changes, while
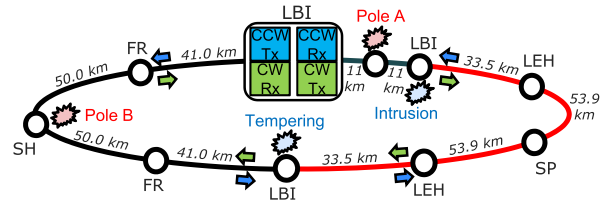

Fig. 43. *Schematic map of a bidirectional vibration sensing and localization field trial, where optical phase was extracted from 200G DP-16QAM coherent receivers. The two DFOS-compatible transponders were colocated at LBI. The map shows the position of various emulated vibration events [58], [97].*

the rest of the cable was buried next to major roadways. Two coherent transponders were colocated at LBI. They each transmitted 200-Gb/s DP-16QAM in the CW and CCW directions, respectively, and the signals were coherently detected by the receiver of the other transponder. Fig. 44(a) shows the phase spectra measured for the vibration events together with the ambient noise level. As per Section II-B, a vibration event is detectable if there exist spectral components where the event is above ambient noise. Furthermore, for events well modeled as a point source, its location can be estimated by correlating the optical phase waveforms recovered at each transponder, and the localization accuracy is a function of the bandwidth above ambient noise and the phase SNR.

Fig. 44(b) shows a localization example where two utility poles A and B spaced 276.8 km apart, as shown in Fig. 43, were struck simultaneously with hammers. Two correlation peaks are observed. The positions of these correlation peaks match the expected positions. This result shows that it is possible to discriminate multiple vibration events on the same cable using the present method, provided that the events are separated by a distance greater than $(c/n_{\text{eff}}(B_{\text{vib},1} + B_{\text{vib},2}))$, where $B_{\text{vib},1}$ and $B_{\text{vib},2}$ are the bandwidths of each vibration event. In addition, as phase SNR is high, the position of the sinc-like correlation peaks varies much less than its full-width at half-maximum (FWHM) [58], [97]. In the hammer strike example, the
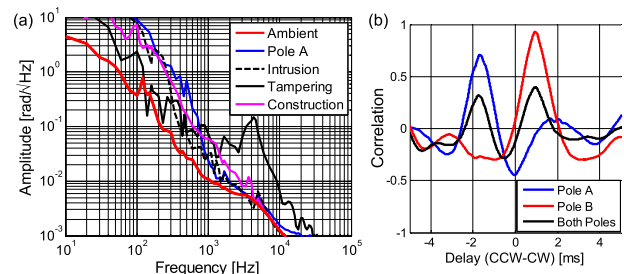

Fig. 44. *(a) Phase spectra measured for various real-world vibration events alongside ambient noise. (b) Correlation between the optical phases measured for the CW and CCW directions due to utility poles A and B being struck separately with hammers and when both poles were struck simultaneously [58], [97].*

standard deviation in the estimated position was a few kilometers, whereas, for tampering, due to its higher bandwidth of >30 kHz, the standard deviation in the estimated position was as small as 25 m.

C. SOP Measurement Using Data-Modulated Signals

The SOP measurement method was originally inspired by the observation that lightning strikes cause fast polarization fluctuations in aerial cables. This potentially enables aerial cables to serve as sensors for monitoring lightning strikes [155].

Recently, this method has also been adopted to detect seismic waves in submarine cables [99]. In contrast to aerial cables, the submarine environment is orders of magnitude quieter except for short sections near landing stations or in shallow water. The ocean bottom is a unique environment at a near constant temperature of around 4 °C, with minimal mechanical or electromagnetic perturbations. Nevertheless, submarine cables remain sensitive to the movement of the seafloor caused by seismic waves or changes in hydrostatic pressure arising from ocean swell propagating downward from the surface to the seafloor. The experiment described in [99] was conducted over a 10 000-km-long Curie cable connecting Los Angeles, USA, with Valparaiso, Chile. The route of this cable traverses a seismically active region near the eastern edge of the Pacific Plate, where 50 large earthquakes greater than M_W 7.5 have been observed since 1900. As described in Section II-E, the Stokes vector of SOP was obtained from the adaptive equalizer taps of a commercial coherent transponder's application-specific integrated circuit (ASIC) at a sampling interval of 56 ms [100].

To extract the vibration signal of interest arising from seismic waves and ocean waves, it was necessary to remove slowly varying polarization drift, which was attributed to temperature drift and mechanical vibration near landing stations. Slowly varying polarization drift was obtained by taking a moving average of the Stokes parameters over a 200-s time window. This allowed the determination of rotation matrices, which rotates the moving average to the north pole of the Poincaré sphere $\mathbf{S} = [0, 0, 1]$ and is equivalent to performing a high-pass filtering operation with a cutoff frequency of 5 mHz. The residual SOP fluctuations after rotation are due to the vibration phenomena of interest and are mostly confined to S_1 and S_2.

Fig. 45(a) shows the fluctuation of Stokes parameters due to an M_W 7.4 earthquake near Oaxaca, Mexico, on June 23, 2020. The PSD revealed in Fig. 45(b) and (c) shows that earthquake energy is concentrated between 0.01 and 1 Hz, with a pronounced peak from 0.15 to 0.35 Hz. Despite using telecom grade lasers with linewidth on the order of tens of kHz, with much higher PN at low frequencies than metrology grade lasers like that in [95], the PSD of SOP fluctuation is flat down to 0.01 Hz. Insensitivity to laser PN is an advantage of the
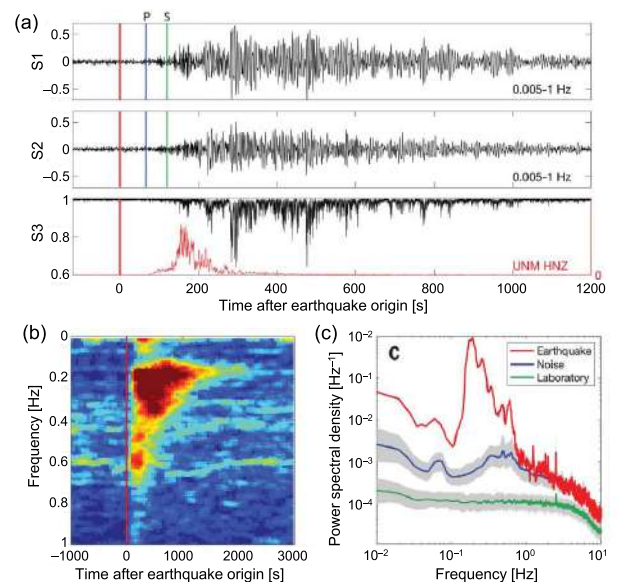

Fig. 45. *(a) SOP anomaly measured in the presence of an M_W 7.4 earthquake. SOP was extracted from the equalizer of a commercial coherent transponder. (b) Spectrogram of the SOP anomaly. (c) Comparison between the PSD measured in the presence of the earthquake with ambient noise. Results are reproduced from [99].*

SOP method. However, owing to the small bandwidth of seismic signals, the ability to localize earthquakes may be limited.

The experimental examples presented in this section show the feasibility of DFOS based on forward transmission, either by launching a c.w. signal with sufficiently low power to avoid inducing excessive nonlinear penalty on any copropagating telecom signals; alternatively, the telecom signal itself may serve as the probe signal. Compared with methods based on backscatter measurement, forward transmission can potentially achieve greater reach due to better optical SNR but likely at the price of poorer spatial resolution. In backscatter measurement methods, spatial resolution can be controlled by the sensing transponder via the bandwidth of the probe signal. In bidirectional forward transmission, the spatial resolution depends only on the spectral characteristics of the vibration source and is not controllable by the sensing transponder.

VIII. DISCUSSION

Practical deployment of DFOS systems must take into account numerous factors and constraints. One example is network architecture constraints. Deployed networks typically have inline EDFAs with isolators at their outputs that prevent backscatter from propagating back to the sensing transponder. Then, there are also optical cross-connects such as reconfigurable optical add/drop multiplexers (ROADMs) with significant insertion loss and, depending on their design, may also not allow backscatter

This article has been accepted for inclusion in a future issue of this journal. Content is final as presented, with the exception of pagination.

Ip *et al.*: Using Global Existing Fiber Networks for Environmental Sensing

to pass through. In order for DFOS to have a range greater than one fiber span, it may be necessary to redesign network elements to provide a return path for the backscatter. Some proposed solutions in the literature include using bidirectional EDFAs [182] or all-Raman amplifiers without isolators [76]. However, these solutions used in lab experiments are not currently deployed. In submarine cables, a return path connecting the outputs of repeater amplifiers in opposite directions is already provided to assist fault localization using coherent OTDR [183], [184]. However, the high loss of the loopback circuit and low power level of the backscatter before amplification make DFOS difficult.

Deployed terrestrial cables are also prone to repeated fiber cuts and resplicing, resulting in large lumped losses due to bad splices, fiber bends, and connectors. Increased return loss will reduce the optical SNR of the backscatter. The presence of flat connectors at patch panels will also create Fresnel reflections, which manifests as spikes in a coherent OTDR. Depending on how the signal is amplified before detection, spikes in the OTDR may even cause optical damage to the receiver though the use of coded probe signals will help reduce the peak-to-average power ratio (PAPR) arising from point source reflections. High PAPR will also result when interrogating fiber spans of even moderate length (e.g., a fiber span with 20-dB span loss has a return loss difference of 40 dB between start and end points). Rayleigh fading will further increase PAPR. When the OTDR signal is digitized, quantization noise may be an issue at weak signal points. This may require preprocessing the OTDR signal to reduce its PAPR before digitization, or the sensing system may only interrogate a shorter section of fiber at a time to reduce signal amplitude difference from beginning to end.

The sensing signals describe in Section II are typically pulsed. Just as legacy ON–OFF keying (OOK) can incur a large XPM penalty on coherent telecom signals based on dual-polarization quadrature amplitude modulation (DP-QAM) [185], sensing signals will likewise induce nonlinear penalties. To ascertain compatibility between DFOS and data transmission, the launched power of the sensing signal needs to be carefully controlled, and the copropagating telecom channels must be verified to be error-free. Investigation into the coexistence between DFOS and data transmission has been conducted in, e.g., [18] and [59]. It is also possible to shape the amplitude profile of the sensing signal to lengthen the duration of the probe signal's rise and fall times to reduce the XPM penalty [76]. An advantage of forward transmission schemes using data-modulated signals presented in Section VII is that they circumvent the coexistence issue.

DFOS systems can generate very large datasets owing to the ratio between the bandwidth of the sensing signal and the frequency of the slowest environmental disturbance that needs to be measured. For example, a conventional DAS with 10-m resolution requires using pulses of 100-ns duration. Even if the pulses are Nyquist-shaped, the optical signal needs to be sampled at >10 MSa/s. If vibration frequencies down to 0.01 Hz are required for studying seismic signals, a naïve real implementation will need to store 10^9 samples for processing. Memory requirement can be reduced if the vibration source has minimal high-frequency content, and the length of fiber being monitored has a round-trip propagation time much less than the required vibration sampling rate T_p. However, the use diversity or chirping in the case of DD-CP-OTDR will increase memory requirements. DFOS transponders can be expected to perform front-end DSP operations to at least recover the strain or temperature time series at an appropriate sampling rate. Even if these raw data are to be transmitted to a central server for further processing, the data rate requirement will be low (e.g., a few tens of kHz). Realistically, the AI function will be performed by onboard DSP at the DFOS transponder, as described in Section IV. The DFOS transponder will then only need to store and report anomalies to the central office, thus drastically reducing memory requirements.

IX. CONCLUSION

DFOS is an evolving field that has gained increasing attention from telecom operators for whom DFOS offers new opportunities for new applications using the existing global fiber infrastructure, with the potential to facilitate scientific research, enhance public safety, and build smarter cities. Most DFOS systems in research and development today are based on backscatter measurement via an OTDR, where events at different distances along a cable are discriminated by different round-trip propagation delays. The scattering mechanisms in glass are sensitive to strain and temperature. With innovative cable design, it is possible to transduce other environmental changes into these variables that are measurable using existing DFOS methods. Rayleigh scattering is widely used in DAS and DVS, and Brillouin scattering is used in DTS and DSS, while Raman scattering is used in DTS. The key performance parameters in a DFOS system include spatial resolution, sensing distance, measurand resolution, and sensing bandwidth. For a given application, the sensing transponder can choose appropriate parameters, such as the bandwidth and repetition rate of the sensing signal, to allow the best tradeoff between desirable performance characteristics.

DFOS can benefit from advances in other fields, such as radar and telecommunications. Indeed, the optical fiber can be viewed as a 1-D radar. Due to advances in telecom, coherent receivers, ADCs, and digital-DACs capable of multi-GHz bandwidths are now widely available components at a reasonable cost. They enable the recovery of the electric field of the received backscatter without loss of information and allow arbitrary manipulation of the transmitted and received signals via powerful DSP algorithms. Coding, frequency diversity, and spatial diversity are tools that can increase optical SNR, sensing bandwidth, and sensing range. Similarly, chirped radar has inspired the development of chirped-pulse OTDR and OFDR.

We reviewed a variety of DFOS applications in Geohazard monitoring, seismic monitoring, traffic monitoring, and infrastructure health monitoring. Events of interest often have unique spatiotemporal characteristics that can be exploited for their detection and localization. For example, when soil erosion exposes a part of the cable to the ambient environment, it can create a localized temperature abnormality with a unique settling time or unique delay relative to fluctuations in the ambient air temperature. Rockfalls and landslides result in a localized increase in ground pressure, which can be detected using DSS. Buried terrestrial cables situated along major roadways can be used for traffic monitoring. Passing vehicles then appear as lines on a DAS "waterfall" plot, and ML algorithms can be used to identify vehicles and estimate their speed and density. Spatiotemporal profiles of temperature and strain can also be transformed into the f-k domain, which is a powerful tool for analyzing the propagation characteristics of a variety of ocean waves and seismic waves that propagate in water or along the water–seafloor interface. The use of chirped-pulse DAS, with its uniform measurand resolution and excellent low-frequency performance, has led to the detection of seismic Scholte waves, which was previously difficult to study.

Recently, DFOS methods based on forward transmission were also revisited. Although much work remains to be conducted, this method has already been demonstrated for earthquake detection and infrastructure monitoring in terrestrial and submarine cables.

Future research in the DFOS system can focus on several areas. AI and ML methods, such as deep neural networks (DNNs) and convolutional neural networks (CNNs), can help improve the accuracy of event detection, classification, and localization. Improvements in laser technology can extend the frequency range over which phenomena of interest can be monitored. Future network design can take DFOS into consideration by providing pathways for backscattered light to return to the sensing transponder, thus facilitating the coexistence between telecommunication and environmental sensing. ∎

REFERENCES

[1] M. Jacoby, "As telecom demands grow, optical fibers will need to level up," *Chem. Eng. News*, vol. 98, no. 10, Mar. 2020. Accessed: Aug. 24, 2022. [Online]. Available: https://cen.acs.org/materials/photonics/telecom-demands-grow-optical-fibers/98/i10

[2] K. C. Kao and G. A. Hockham, "Dielectric-fibre surface waveguides for optical frequencies," *Proc. IEE*, vol. 113, no. 7, pp. 1151–1158, Jul. 1966.

[3] *Distributed and Single Point Fiber Optic Sensing Systems Forecast*. Accessed: Aug. 24, 2022. [Online]. Available: https://www.igigroup.com/st/pages/photonic_sensor_report.html

[4] *Distributed Fiber Optic Sensor Market Size Share & Trends Analysis Report*. Accessed: Aug. 24, 2022. [Online]. Available: https://www.grandview research.com/industry-analysis/distributed-fiber-optic-sensor-sensing-dfos-market

[5] J. A. Bucaro, H. D. Dardy, and E. F. Carome, "Optical fiber acoustic sensor," *Appl. Opt.*, vol. 16, no. 7, pp. 1761–1762, Jul. 1977.

[6] C. D. Butter and G. B. Hocker, "Fiber optics strain gauge," *Appl. Opt.*, vol. 17, no. 18, pp. 2867–2869, Sep. 1978.

[7] G. B. Hocker, "Fiber-optic sensing of pressure and temperature," *Appl. Opt.*, vol. 18, no. 9, pp. 1445–1448, May 1979.

[8] V. Vali and R. W. Shorthill, "Fiber ring interferometer," *Appl. Opt.*, vol. 15, no. 5, pp. 1099–1100, May 1976.

[9] M. K. Barnoski and S. M. Jensen, "Fiber waveguides: A novel technique for investigating attenuation characteristics," *Appl. Opt.*, vol. 15, no. 9, pp. 2112–2115, Sep. 1976.

[10] J. King, D. Smith, K. Richards, P. Timson, R. Epworth, and S. Wright, "Development of a coherent OTDR instrument," *J. Lightw. Technol.*, vol. 5, no. 4, pp. 616–624, Apr. 1987.

[11] A. J. Rogers, "Polarization-optical time domain reflectometry: A technique for the measurement of field distributions," *Appl. Opt.*, vol. 20, no. 6, pp. 1060–1074, Mar. 1981.

[12] W. Eickhoff and R. Ulrich, "Optical frequency domain reflectometry in single-mode fiber," *Appl. Phys. Lett.*, vol. 39, no. 9, pp. 693–695, Sep. 1981.

[13] Y. Wu, J. Gan, Q. Li, Z. Zhang, X. Heng, and Z. Yang, "Distributed fiber voice sensor based on phase-sensitive optical time-domain reflectometry," *IEEE Photon. J.*, vol. 7, no. 6, pp. 1–10, Dec. 2015.

[14] C. Franciscangelis, W. Margulis, L. Kjellberg, I. Soderquist, and F. Fruett, "Real-time distributed fiber microphone based on phase-OTDR," *Opt. Exp.*, vol. 24, no. 26, pp. 29597–29602, Dec. 2016.

[15] J. C. Juarez, E. W. Maier, K. N. Choi, and H. F. Taylor, "Distributed fiber-optic intrusion sensor system," *J. Lightw. Technol.*, vol. 23, no. 6, pp. 2081–2087, Jun. 2005.

[16] H. Wu et al., "Field test of a fully distributed fiber optic intrusion detection system for long-distance security monitoring of national borderline," *Proc. SPIE*, vol. 9157, Jun. 2014, Art. no. 915790.

[17] H. Liu, J. Ma, W. Yan, W. Liu, X. Zhang, and C. Li, "Traffic flow detection using distributed fiber optic acoustic sensing," *IEEE Access*, vol. 6, pp. 68968–68980, 2018.

[18] M.-F. Huang et al., "First field trial of distributed fiber optical sensing and high-speed communication over an operational telecom network," *J. Lightw. Technol.*, vol. 38, no. 1, pp. 75–81, Jan. 1, 2020.

[19] J. B. Ajo-Franklin et al., "Distributed acoustic sensing using dark fiber for near-surface characterization and broadband seismic event detection," *Sci. Rep.*, vol. 9, no. 1, p. 1328, Dec. 2019.

[20] E. F. Williams et al., "Distributed sensing of microseisms and teleseisms with submarine dark fibers," *Nature Commun.*, vol. 10, no. 1, pp. 1–11, 2019.

[21] M. R. Fernández-Ruiz, "Distributed acoustic sensing for seismic activity monitoring," *APL Photon.*, vol. 5, Feb. 2020, Art. no. 030901.

[22] M. Niklès, L. Thévenaz, and P. A. Robert, "Brillouin gain spectrum characterization in single-mode optical fibers," *J. Lightw. Technol.*, vol. 15, no. 10, pp. 1842–1851, Oct. 1997.

[23] T. Horiguchi, T. Kurashima, and M. Tateda, "A technique to measure distributed strain in optical fibers," *IEEE Photon. Technol. Lett.*, vol. 2, no. 5, pp. 352–354, May 1990.

[24] F. Farahi, C. N. Pannell, and D. A. Jackson, "Potential of stimulated Brillouin scattering as sensing mechanism for distributed temperature sensors," *Electron. Lett.*, vol. 25, no. 14, pp. 913–915, Jul. 1989.

[25] X. Bao, D. J. Webb, and D. A. Jackson, "22-km distributed temperature sensor using Brillouin gain in an optical fiber," *Opt. Lett.*, vol. 18, no. 7, pp. 552–554, Apr. 1993.

[26] X. Bao, D. J. Webb, and D. A. Jackson, "Combined distributed temperature and strain sensor based on Brillouin loss in an optical fiber," *Opt. Lett.*, vol. 19, no. 2, pp. 141–143, Jan. 1994.

[27] M. Niklès, L. Thévenaz, and P. A. Robert, "Simple distributed fiber sensor based on Brillouin gain spectrum analysis," *Opt. Lett.*, vol. 21, no. 10, pp. 758–760, May 1996.

[28] D. Garcus, T. Gogolla, K. Krebber, and F. Schliep, "Brillouin optical-fiber frequency-domain analysis for distributed temperature and strain measurements," *J. Lightw. Technol.*, vol. 15, no. 4, pp. 654–662, Apr. 1997.

[29] M. Nikles et al., "Leakage detection using fiber optics distributed temperature monitoring," *Proc. SPIE*, vol. 5384, pp. 18–25, Jul. 2004.

[30] L. Zou, X. Bao, F. Ravet, and L. Chen, "Distributed Brillouin fiber sensor for detecting pipeline buckling in an energy pipe under internal pressure," *Appl. Opt.*, vol. 45, no. 14, pp. 3372–3377, May 2006.

[31] F. Ravet, F. Briffod, and M. Nikles, "Extended distance fiber optic monitoring for pipeline leak and ground movement detection," in *Proc. Int. Pipeline Conf. (IPC)*, Calgary, AB, Canada, 2008, pp. 689–697, Paper IPC2008-64521.

[32] C. Borda, M. Niklès, E. Rochat, A. Grechanov, A. Naumov, and V. Velikodnev, "Continuous

This article has been accepted for inclusion in a future issue of this journal. Content is final as presented, with the exception of pagination.

Ip *et al.*: Using Global Existing Fiber Networks for Environmental Sensing

real-time pipeline deformation, 3D positioning and ground movement monitoring along the Sakhalin-Khabarovsk-Vladivostok pipeline," in *Proc. Int. Pipeline Conf. (IPC)*, Calgary, AB, Canada, Sep. 2012, pp. 179–187, Paper IPC2012-90476.

[33] H.-J. Yoon, K.-Y. Song, J.-S. Kim, and D.-S. Kim, "Longitudinal strain monitoring of rail using a distributed fiber sensor based on Brillouin optical correlation domain analysis," *NDT & E Int.*, vol. 44, no. 7, pp. 637–644, Nov. 2011.

[34] A. Minardo, G. Porcaro, D. Giannetta, R. Bernini, and L. Zeni, "Real-time monitoring of railway traffic using slope-assisted Brillouin distributed sensors," *Appl. Opt.*, vol. 52, no. 16, pp. 3770–3776, Jun. 2013.

[35] F. Bastianini, A. Rizzo, N. Galati, U. Deza, and A. Nanni, "Discontinuous Brillouin strain monitoring of small concrete bridges: Comparison between near-to-surface and smart FRP fiber installation techniques," *Proc. SPIE*, vol. 5765, pp. 612–623, May 2005.

[36] A. Minardo, R. Bernini, L. Amato, and L. Zeni, "Bridge monitoring using Brillouin fiber-optic sensors," *IEEE Sensors J.*, vol. 12, no. 1, pp. 145–150, Jan. 2012.

[37] O. Artières *et al.*, "Assessment of dams and dikes behavior with a fibre optic based monitoring solution," in *Proc. 2nd Int. Congr. Dam Maintenance Rehabil.*, Nov. 2010, pp. 79–86.

[38] D. Inaudi, I. Cottone, and A. Figini, "Monitoring dams and levees with distributed fiber optic sensing," in *Proc. 6th Int. Conf. Struct. Health Monit. Intell. Infrastruct.*, Hong Kong, Dec. 2013, pp. 1–10.

[39] T. Yari, M. Ishioka, K. Nagai, and T. Sakurai, "An application test using Brillouin optical correlation base analysis method for aircraft structural health monitoring," *Proc. SPIE*, vol. 6167, pp. 91–100, Mar. 2006.

[40] S. Minakuchi, Y. Okabe, T. Mizutani, and N. Takeda, "Barely visible impact damage detection for composite sandwich structures by optical-fiber-based distributed strain measurement," *Smart Mater. Struct.*, vol. 18, no. 8, Jul. 2009, Art. no. 085018.

[41] J. P. Dakin, D. J. Pratt, G. W. Bibby, and J. N. Ross, "Distributed optical fibre Raman temperature sensor using a semiconductor light source and detector," *Electron. Lett.*, vol. 21, no. 13, pp. 569–570, Jun. 1985.

[42] A. H. Hartog, A. P. Leach, and M. P. Gold, "Distributed temperature sensing in solid-core fibers," *Electron. Lett.*, vol. 21, no. 23, pp. 1061–1062, 1985.

[43] J. P. Dakin, D. J. Pratt, G. W. Bibby, and J. N. Ross, "Temperature distribution measurement using Raman ratio thermometry," *Proc. SPIE*, vol. 566, pp. 249–256, Jan. 1986.

[44] G. R. Williams, G. Brown, W. Hawthorne, A. H. Hartog, and P. C. Waite, "Distributed temperature sensing (DTS) to characterize the performance of producing oil wells," *Proc. SPIE*, vol. 4202, pp. 39–54, Dec. 2000.

[45] L.-B. Ouyang and D. L. Belanger, "Flow profiling by distributed temperature sensor (DTS) system—Expectation and reality," *SPE Prod. Oper.*, vol. 21, pp. 269–281, May 2006.

[46] F. Tanimola and D. Hill, "Distributed fibre optic sensors for pipeline protection," *J. Natural Gas Sci. Eng.*, vol. 1, nos. 4–5, pp. 134–143, Nov. 2009.

[47] A. Mirzaei, A. R. Bahrampour, M. Taraz, A. Bahrampour, M. J. Bahrampour, and S. M. A. Foroushani, "Transient response of buried oil pipelines fiber optic leak detector based on the distributed temperature measurement," *Int. J. Heat Mass Transf.*, vol. 65, pp. 110–122, Oct. 2013.

[48] S. Nakamura, S. Morooka, and K. Kawasaki, "Conductor temperature monitoring system in underground power transmission XLPE cable joints," *IEEE Trans. Power Del.*, vol. 7, no. 4, pp. 1688–1697, Oct. 1992.

[49] J. Downes and H. Y. Leung, "Distributed temperature sensing worldwide power circuit monitoring applications," in *Proc. Int. Conf. Power*

Syst. Technol. (PowerCon), vol. 2, Nov. 2004, pp. 1804–1809.

[50] S. C. Steele-Dunne *et al.*, "Feasibility of soil moisture estimation using passive distributed temperature sensing," *Water Resour. Res.*, vol. 46, no. 3, pp. 1–12, Mar. 2010.

[51] A. M. Striegl and S. P. Loheide, "Heated distributed temperature sensing for field scale soil moisture monitoring," *Ground Water*, vol. 50, no. 3, pp. 340–347, May 2012.

[52] A. Hartog, "A distributed temperature sensor based on liquid-core optical fibers," *J. Lightw. Technol.*, vol. 1, no. 3, pp. 498–509, Sep. 1, 1983.

[53] R. Magalhães *et al.*, "Fiber-based distributed bolometry," *Opt. Exp.*, vol. 27, no. 4, pp. 4317–4328, Feb. 2019.

[54] R. Magalhães *et al.*, "Towards distributed measurements of electric fields using optical fibers: Proposal and proof-of-concept experiment," *Sensors*, vol. 20, no. 16, 4461, pp. 1–13, Aug. 2020.

[55] A. Garcia-Ruiz *et al.*, "Distributed photothermal spectroscopy in microstructured optical fibers: Towards high-resolution mapping of gas presence over long distances," *Opt. Exp.*, vol. 25, no. 3, pp. 1789–1805, Feb. 2017.

[56] J. Paek, K. Chintalapudi, R. Govindan, J. Caffrey, and S. Masri, "A wireless sensor network for structural health monitoring: Performance and experience," in *Proc. 2nd IEEE Workshop Embedded Networked Sensors (EmNetS-II)*, Sydney, NSW, Australia, May 2005, pp. 1–9.

[57] S. Jeong, Z. Foo, Y. Lee, J.-Y. Sim, D. Blaauw, and D. Sylvester, "A fully-integrated 71 nW CMOS temperature sensor for low power wireless sensor nodes," *IEEE J. Solid-State Circuits*, vol. 49, no. 8, pp. 1682–1693, Aug. 2014.

[58] G. A. Wellbrock *et al.*, "Field trial of vibration detection and localization using coherent telecom transponders over 380-km link," in *Proc. Opt. Fiber Commun. Conf. (OFC)*, San Francsico, CA, USA, 2021, pp. 1–3, Paper F3B.2.

[59] Z. Jia *et al.*, "Experimental coexistence investigation of distributed acoustic sensing and coherent communication systems," in *Proc. Opt. Fiber Commun. Conf. (OFC)*, San Francisco, CA, USA, 2021, pp. 1–3, Paper Th4.F.4.

[60] K. Toge and F. Ito, "Recent research and development of optical fiber monitoring in communication systems," *Photonic Sensors*, vol. 3, no. 4, pp. 304–313, Oct. 2013.

[61] M. Niklés, "Fibre optic distributed scattering sensing system: Perspectives and challenges for high performance applications," *Proc. SPIE*, vol. 6619, Jul. 2007, Art. no. 66190D.

[62] E. Ip, A. P. T. Lau, D. J. Barros, and J. M. Kahn, "Coherent detection in optical fiber systems," *Opt. Exp.*, vol. 16, no. 2, pp. 753–791, Jan. 2008.

[63] E. M. Ip and J. M. Kahn, "Fiber impairment compensation using coherent detection and digital signal processing," *J. Lightw. Technol.*, vol. 28, no. 4, pp. 502–519, Jul. 24, 2010.

[64] J. Alnis, A. Matveev, N. Kolachevsky, T. Udem, and T. W. Hänsch, "Subhertz linewidth diode lasers by stabilization to vibrationally and thermally compensated ultralow-expansion glass Fabry–Pérot cavities," *Phys. Rev. A, Gen. Phys.*, vol. 77, no. 5, May 2008, Art. no. 053809.

[65] Q. Yan, M. Tian, X. Li, Q. Yang, and Y. Xu, "Coherent φ-OTDR based on polarization-diversity integrated coherent receiver and heterodyne detection," *Proc. SPIE*, vol. 10323, Apr. 2017, Art. no. 103283.

[66] A. Meiyappan, P.-Y. Kam, and H. Kim, "On decision aided carrier phase and frequency offset estimation in coherent optical receivers," *J. Lightw. Technol.*, vol. 31, no. 13, pp. 2055–2069, Jul. 1, 2013.

[67] S. J. Savory, "Digital filters for coherent optical receivers," *Opt. Exp.*, vol. 16, no. 2, pp. 804–817, Jan. 2008.

[68] M. D. Jones, "Using simplex codes to improve OTDR sensitivity," *IEEE Photon. Technol. Lett.*, vol. 5, no. 7, pp. 822–824, Jul. 1993.

[69] Y. Wu, Z. Wang, J. Xiong, and Y. Rao, "Bipolar

coding for phase-demodulated ϕ-OTDR with coherent detection," in *Proc. 18th Int. Conf. Opt. Commun. Netw. (ICOCN)*, Huangshan, China, Aug. 2019, pp. 1–3.

[70] Y. Muanenda, C. J. Oton, S. Faralli, and F. Di Pasquale, "A cost-effective distributed acoustic sensor using a commercial off-the-shelf DFB laser and direct detection phase-OTDR," *IEEE Photon. J.*, vol. 8, no. 1, pp. 1–10, Feb. 2016.

[71] J. Pastor-Graells, H. F. Martins, A. Garcia-Ruiz, S. Martin-Lopez, and M. Gonzalez-Herraez, "Single-shot distributed temperature and strain tracking using direct detection phase-sensitive OTDR with chirped pulses," *Opt. Exp.*, vol. 24, no. 12, pp. 13121–13133, Jun. 2016.

[72] D. Chen, Q. Liu, and Z. He, "Phase-detection distributed fiber-optic vibration sensor without fading-noise based on time-gated digital OFDR," *Opt. Exp.*, vol. 25, no. 7, pp. 8315–8325, Mar. 2017.

[73] M. R. Fernandez-Ruiz, J. Pastor-Graells, H. F. Martins, A. Garcia-Ruiz, S. Martin-Lopez, and M. Gonzalez-Herraez, "Laser phase-noise cancellation in chirped-pulse distributed acoustic sensors," *J. Lightw. Technol.*, vol. 36, no. 4, pp. 979–985, Feb. 15, 2018.

[74] M. R. Fernández-Ruiz, L. Costa, and H. F. Martins, "Distributed acoustic sensing using chirped-pulse phase-sensitive OTDR technology," *Sensors*, vol. 19, no. 20, pp. 1–28, Oct. 2019.

[75] O. H. Waagaard *et al.*, "Real-time low noise distributed acoustic sensing in 171 km low loss fiber," *OSA Continuum*, vol. 4, no. 2, pp. 688–701, Feb. 2021.

[76] E. Ip *et al.*, "DAS over 1,007-km hybrid link with 10-Tb/s DP-16QAM co-propagation using frequency-diverse chirped pulses," in *Proc. Opt. Fiber Commun. Conf. (OFC)*, San Diego, CA, USA, 2022, pp. 1–3, Paper Th4A.2.

[77] F. Baronti *et al.*, "SNR enhancement of Raman-based long-range distributed temperature sensors using cyclic simplex codes," *Electron. Lett.*, vol. 46, no. 17, pp. 1221–1223, Aug. 2010.

[78] M. A. Soto, G. Bolognini, F. Di Pasquale, and L. Thévenaz, "Simplex-coded BOTDA fiber sensor with 1 m spatial resolution over a 50 m range," *Opt. Lett.*, vol. 35, no. 2, pp. 259–261, Jan. 2010.

[79] D. Lee, H. Yoon, P. Kim, J. Park, and N. Park, "Optimization of SNR improvement in the noncoherent OTDR based on simplex codes," *J. Lightw. Technol.*, vol. 24, no. 1, pp. 322–326, Feb. 6, 2006.

[80] H. Iribas, A. Loayssa, F. Sauser, M. Llera, and S. Le Floch, "Cyclic coding for Brillouin optical time-domain analyzers using probe dithering," *Opt. Exp.*, vol. 25, no. 8, pp. 8787–8800, Apr. 2017.

[81] Z. Yang, Z. Li, S. Zaslawski, L. Thévenaz, and M. A. Soto, "Design rules for optimizing unipolar coded Brillouin optical time-domain analyzers," *Opt. Exp.*, vol. 26, no. 13, pp. 16505–16523, Jun. 2018.

[82] M. A. Soto, S. Le Floch, and L. Thévenaz, "Bipolar optical pulse coding for performance enhancement in BOTDA sensors," *Opt. Exp.*, vol. 21, no. 14, pp. 16390–16397, Jul. 2013.

[83] M. Nazarathy *et al.*, "Real-time long range complementary correlation optical time domain reflectometer," *J. Lightw. Technol.*, vol. 7, no. 1, pp. 24–38, Jan. 1989.

[84] Y. Mao, N. Guo, K. Yu, and H. Tam, "1-cm spatial-resolution Brillouin optical time-domain analysis based on bright pulse Brillouin gain and complementary code," *IEEE Photon. J.*, vol. 4, no. 6, pp. 2243–2249, Dec. 2012.

[85] X. Sun *et al.*, "Genetic-optimised aperiodic code for distributed optical fibre sensors," *Nature Commun.*, vol. 11, no. 1, p. 5774, Nov. 2020.

[86] S. L. Floch, F. Sauser, M. Llera, and E. Rochat, "Novel Brillouin optical time-domain analyzer for extreme sensing range using high-power flat frequency-coded pump pulses," *J. Lightw. Technol.*, vol. 33, no. 12, pp. 2623–2627, Jun. 15, 2015.

[87] S. Le Floch, F. Sauser, M. Llera, and E. Rochat, "Colour cyclic code for Brillouin distributed

This article has been accepted for inclusion in a future issue of this journal. Content is final as presented, with the exception of pagination.

Ip *et al.*: Using Global Existing Fiber Networks for Environmental Sensing

sensors," *Proc. SPIE*, vol. 9634, Sep. 2015, Art. no. 963431.

[88] H. Iida, Y. Koshikiya, F. Ito, and K. Tanaka, "High-sensitivity coherent optical time domain reflectometry employing frequency-division multiplexing," *J. Lightw. Technol.*, vol. 30, no. 8, pp. 1121–1126, Apr. 15, 2012.

[89] M. J. Murray, A. Davis, and B. Redding, "Multimode fiber ϕ-OTDR with holographic demodulation," *Opt. Exp.*, vol. 26, no. 18, pp. 23019–23030, Sep. 2018.

[90] J. Gu *et al.*, "High SNR ϕ-OTDR based on frequency and wavelength diversity with differential vector aggregation method," *IEEE Photon. J.*, vol. 12, no. 6, pp. 1–12, Dec. 2020.

[91] S. Guerrier, C. Dorize, E. Awwad, and J. Renaudier, "Introducing coherent MIMO sensing, a fading-resilient, polarization-independent approach to ϕ-OTDR," *Opt. Exp.*, vol. 28, no. 14, pp. 21081–21094, Jul. 2020.

[92] C. Dorize, S. Guerrier, E. Awwad, P. A. Nwakamma, H. Mardoyan, and J. Renaudier, "An OFDM-MIMO distributed acoustic sensing over deployed telecom fibers," in *Proc. Opt. Fiber Commun. Conf. (OFC)*, San Francisco, CA, USA, 2021, pp. 1–3, Paper W7C.2.

[93] D. Iida, K. Toge, and T. Manabe, "High-frequency distributed acoustic sensing faster than repetition limit with frequency-multiplexed phase-OTDR," in *Proc. Opt. Fiber Commun. Conf.*, Anaheim, CA, USA, 2016, pp. 1–3, Paper M2D.6.

[94] D. Iida, K. Toge, and T. Manabe, "Distributed measurement of acoustic vibration location with frequency multiplexed phase-OTDR," *Opt. Fiber Technol.*, vol. 36, pp. 19–25, Jul. 2017.

[95] G. Marra *et al.*, "Ultrastable laser interferometry for earthquake detection with terrestrial and submarine cables," *Science*, vol. 361, no. 6401, pp. 486–490, Aug. 2018.

[96] Y. Yan, F. N. Khan, B. Zhou, A. P. T. Lau, C. Lu, and C. Guo, "Forward transmission based ultra-long distributed vibration sensing with wide frequency response," *J. Lightw. Technol.*, vol. 39, no. 7, pp. 2241–2249, Apr. 1, 2021.

[97] E. Ip *et al.*, "Vibration detection and localization using modified digital coherent telecom transponders," *J. Lightw. Technol.*, vol. 40, no. 5, pp. 1472–1482, Mar. 1, 2022.

[98] M. Mazur *et al.*, "Transoceanic phase and polarization fiber sensing using real-time coherent transceiver," in *Proc. Opt. Fiber Commun. Conf. (OFC)*, San Diego, CA, USA, 2022, pp. 1–3, Paper M2.F.2.

[99] Z. Zhan *et al.*, "Optical polarization–based seismic and water wave sensing on transoceanic cables," *Science*, vol. 371, no. 6532, pp. 931–936, Feb. 2021.

[100] A. Mecozzi, M. Cantono, J. C. Castellanos, V. Kamalov, R. Müller, and Z. Zhan, "Polarization sensing using submarine optical cables," *Optica*, vol. 8, no. 6, pp. 788–795, Jun. 2021.

[101] L. B. Liokumovich, N. A. Ushakov, O. I. Kotov, M. A. Bisyarin, and A. H. Hartog, "Fundamentals of optical fiber sensing schemes based on coherent optical time domain reflectometry: Signal model under static fiber conditions," *J. Lightw. Technol.*, vol. 33, no. 17, pp. 3660–3671, Sep. 1, 2015.

[102] P. Gysel and R. K. Staubli, "Statistical properties of Rayleigh backscattering in single-mode fibers," *J. Lightw. Technol.*, vol. 8, no. 4, pp. 561–567, Apr. 1990.

[103] Y. Koyamada, M. Imahama, K. Kubota, and K. Hogari, "Fiber-optic distributed strain and temperature sensing with very high measurand resolution over long range using coherent OTDR," *J. Lightw. Technol.*, vol. 27, no. 9, pp. 1142–1146, May 1, 2009.

[104] A. Masoudi and T. P. Newson, "High spatial resolution distributed optical fiber dynamic strain sensor with enhanced frequency and strain resolution," *Opt. Lett.*, vol. 42, no. 2, pp. 290–293, Jan. 2017.

[105] Z. Pan, K. Liang, Q. Ye, H. Cai, R. Qu, and Z. Fang, "Phase-sensitive OTDR system based on digital coherent detection," *Proc. SPIE*, vol. 8311,

Nov. 2011, Art. no. 83110S.

[106] Z. Wang *et al.*, "Coherent ϕ-OTDR based on I/Q demodulation and homodyne detection," *Opt. Exp.*, vol. 24, no. 2, pp. 853–858, Jan. 2016.

[107] P. Gallion and G. Debarge, "Quantum phase noise and field correlation in single frequency semiconductor laser systems," *IEEE J. Quantum Electron.*, vol. QE-20, no. 4, pp. 343–349, Apr. 1984.

[108] W. Zou, S. Yang, X. Long, and J. Chen, "Optical pulse compression reflectometry proposal and proof-of-concept experiment," *Opt. Exp.*, vol. 23, no. 1, pp. 512–522, Jan. 2015.

[109] B. Lu *et al.*, "High spatial resolution phase-sensitive optical time domain reflectometer with a frequency-swept pulse," *Opt. Lett.*, vol. 42, no. 3, pp. 391–394, Feb. 2017.

[110] M. R. Fernandez-Ruiz, H. F. Martins, L. Costa, S. Martin-Lopez, and M. Gonzalez-Herraez, "Steady-sensitivity distributed acoustic sensors," *J. Lightw. Technol.*, vol. 36, no. 23, pp. 5690–5696, Oct. 24, 2018.

[111] H. Gabai and A. Eyal, "On the sensitivity of distributed acoustic sensing," *Opt. Lett.*, vol. 41, no. 24, pp. 5648–5651, Dec. 2016.

[112] L. Costa, H. F. Martins, S. Martin-Lopez, M. R. Fernández-Ruiz, and M. Gonzalez-Herraez, "Reaching p$\varepsilon/\sqrt{Hz}$ sensitivity in a distributed optical fiber strain sensor," in *Proc. 26th Int. Conf. Opt. Fiber Sensors*, Lausanne, Switzerland, 2018, pp. 1–4, Paper TuD.3.

[113] S. Kingsley and D. Davies, "OFDR diagnostics for fiber/integrated optic systems and high resolution distributed fiber optic sensing," *Electron. Lett.*, vol. 21, no. 10, pp. 434–435, May 1985.

[114] U. Glombitza and E. Brinkmeyer, "Coherent frequency-domain reflectometry for characterization of single-mode integrated-optical waveguides," *J. Lightw. Technol.*, vol. 11, no. 8, pp. 1377–1384, Aug. 1993.

[115] B. J. Soller, D. K. Gifford, M. S. Wolfe, and M. E. Froggatt, "High resolution optical frequency domain reflectometry for characterization of components and assemblies," *Opt. Exp.*, vol. 13, no. 2, pp. 666–674, Jan. 2005.

[116] S. Venkatesh and W. V. Sorin, "Phase noise considerations in coherent optical FMCW reflectometry," *J. Lightw. Technol.*, vol. 11, no. 10, pp. 1694–1700, Oct. 1993.

[117] T. Okamoto, D. Iida, Y. Koshikiya, and N. Honda, "Deployment condition visualization of aerial optical fiber cable by distributed vibration sensing based on optical frequency domain reflectometry," *J. Lightw. Technol.*, vol. 39, no. 21, pp. 6942–6951, Nov. 1, 2021.

[118] Y. Koshikiya, X. Fan, and F. Ito, "Long range and cm-level spatial resolution measurement using coherent optical frequency domain reflectometry with SSB-SC modulator and narrow linewidth fiber laser," *J. Lightw. Technol.*, vol. 26, no. 18, pp. 3287–3294, Sep. 15, 2008.

[119] Z. Ding *et al.*, "Compensation of laser frequency tuning nonlinearity of a long range OFDR using deskew filter," *Opt. Exp.*, vol. 21, no. 3, pp. 3826–3834, Feb. 2013.

[120] K. Kishida, Y. Yamauchi, and A. Guzik, "Study of optical fibers strain-temperature sensitivities using hybrid Brillouin-Rayleigh system," *Photonic Sensors*, vol. 4, no. 1, pp. 1–11, Mar. 2014.

[121] D.-P. Zhou, W. Li, L. Chen, and X. Bao, "Distributed temperature and strain discrimination with stimulated Brillouin scattering and Rayleigh backscatter in an optical fiber," *Sensors*, vol. 13, no. 2, pp. 1836–1845, Jan. 2013.

[122] X. Lu, M. A. Soto, and L. Thévenaz, "Temperature-strain discrimination in distributed optical fiber sensing using phase-sensitive optical time-domain reflectometry," *Opt. Exp.*, vol. 25, no. 14, pp. 16059–16071, Jul. 2017.

[123] T. R. Parker, M. Farhadiroushan, V. A. Handerek, and A. J. Rogers, "Temperature and strain dependence of the power level and frequency of spontaneous Brillouin scattering in optical fibers," *Opt. Lett.*, vol. 22, no. 11, pp. 787–789, Jun. 1997.

[124] T. R. Parker, M. Farhadiroushan, R. Feced,

V. A. Handerek, and A. J. Rogers, "Simultaneous distributed measurement of strain and temperature from noise-initiated Brillouin scattering in optical fibers," *IEEE J. Quantum Electron.*, vol. 34, no. 4, pp. 645–659, Apr. 1998.

[125] X. Bao and L. Chen, "Recent progress in distributed fiber optic sensors," *Sensors*, vol. 12, no. 7, pp. 8601–8639, Jun. 2012.

[126] G. P. Agrawal, *Nonlinear Fiber Optics*, 6th ed. New York, NY, USA: Academic, 2019.

[127] M. A. Soto and L. Thévenaz, "Modeling and evaluating the performance of Brillouin distributed optical fiber sensors," *Opt. Exp.*, vol. 21, no. 25, pp. 31347–31366, 2013.

[128] S. M. Haneef, Z. Yang, L. Thévenaz, D. Venkitesh, and B. Srinivasan, "Performance analysis of frequency shift estimation techniques in Brillouin distributed fiber sensors," *Opt. Exp.*, vol. 26, no. 11, pp. 14661–14677, May 2018.

[129] F. Ravet *et al.*, "Signal processing technique for distributed Brillouin sensing at centimeter spatial resolution," *J. Lightw. Technol.*, vol. 25, no. 11, pp. 3610–3618, Nov. 1, 2007.

[130] F. Ravet, F. Briffod, B. Glisic, M. Nikles, and D. Inaudi, "Submillimeter crack detection with Brillouin-based fiber-optic sensors," *IEEE Sensors J.*, vol. 9, no. 11, pp. 1391–1396, Nov. 2009.

[131] A. K. Azad, F. N. Khan, W. H. Alarashi, N. Guo, A. P. T. Lau, and C. Lu, "Temperature extraction in Brillouin optical time-domain analysis sensors using principal component analysis based pattern recognition," *Opt. Exp.*, vol. 25, no. 14, pp. 16534–16549, Jul. 2017.

[132] H. Wu, L. Wang, N. Guo, C. Shu, and C. Lu, "Brillouin optical time-domain analyzer assisted by support vector machine for ultrafast temperature extraction," *J. Lightw. Technol.*, vol. 35, no. 19, pp. 4159–4167, Oct. 1, 2017.

[133] M. N. Alahbabi, Y. T. Cho, and T. P. Newson, "Simultaneous temperature and strain measurement with combined spontaneous Raman and Brillouin scattering," *Opt. Lett.*, vol. 30, no. 11, pp. 1276–1278, Jun. 2005.

[134] H. Kee, G. Lees, and T. Newson, "All-fiber system for simultaneous interrogation of distributed strain and temperature sensing by spontaneous Brillouin scattering," *Opt. Lett.*, vol. 25, no. 10, pp. 695–697, May 2000.

[135] B. G. Risch, R. Lovie, D. Roland, E. Rochat, and D. D. Toit, "Optical fiber cable design for distributed pipeline sensing and data transmission," in *Proc. Int. Wire Cable Symp. (IWCS)*, Atlanta, GA, USA, 2015, pp. 1–7, Paper 0582-000070.

[136] M. Zaghloul *et al.*, "Discrimination of temperature and strain in Brillouin optical time domain analysis using a multicore optical fiber," *Sensors*, vol. 18, no. 4, pp. 1–9, Apr. 2018.

[137] J. Fang *et al.*, "Multi-parameter distributed fiber sensing with higher-order optical and acoustic modes," *Opt. Lett.*, vol. 4, no. 5, pp. 1096–1099, Mar. 2019.

[138] Y. Weng, E. Ip, Z. Pan, and T. Wang, "Single-end simultaneous temperature and strain sensing techniques based on Brillouin optical time domain reflectometry in few-mode fibers," *Opt. Exp.*, vol. 23, no. 7, pp. 9024–9039, Apr. 2015.

[139] W. Zou, Z. He, and K. Hotate, "Complete discrimination of strain and temperature using Brillouin frequency shift and birefringence in a polarization-maintaining fiber," *Opt. Exp.*, vol. 17, no. 3, pp. 1248–1255, Feb. 2009.

[140] C. C. Lee, P. W. Chiang, and S. Chi, "Utilization of a dispersion-shifted fiber for simultaneous measurement of distributed strain and temperature through Brillouin frequency shift," *IEEE Photon. Technol. Lett.*, vol. 13, no. 10, pp. 1094–1096, Oct. 2001.

[141] R. Ruiz-Lombera, A. Fuentes, L. Rodriguez-Cobo, J. M. Lopez-Higuera, and J. Mirapeix, "Simultaneous temperature and strain discrimination in a conventional BOTDA via artificial neural networks," *J. Lightw. Technol.*, vol. 36, no. 11, pp. 2114–2121, Jun. 1, 2018.

This article has been accepted for inclusion in a future issue of this journal. Content is final as presented, with the exception of pagination.

Ip *et al.*: Using Global Existing Fiber Networks for Environmental Sensing

[142] R. W. Boyd, *Nonlinear Optics*. New York, NY, USA: Academic, 2008.

[143] G. Bolognini and A. Hartog, "Raman-based fibre sensors: Trends and applications," *Opt. Fiber Technol.*, vol. 19, no. 6, pp. 678–688, Dec. 2013.

[144] G. Bolognini, J. Park, M. A. Soto, N. Park, and F. Di Pasquale, "Analysis of distributed temperature sensing based on Raman scattering using OTDR coding and discrete Raman amplification," *Meas. Sci. Technol.*, vol. 18, no. 10, pp. 3211–3218, Oct. 2007.

[145] M. B. Hausner, F. Suárez, K. Glander, N. van de Giesen, J. S. Selker, and S. W. Tyler, "Calibrating single-ended fiber-optic Raman spectra distributed temperature sensing data," *Sensors*, vol. 11, no. 11, pp. 10859–10879, 2011.

[146] J. E. Shelby, "Molecular diffusion and solubility of hydrogen isotopes in vitreous silica," *J. Appl. Phys.*, vol. 48, no. 8, pp. 3387–3394, Aug. 1977.

[147] A. Fernandez *et al.*, "Radiation-tolerant Raman distributed temperature monitoring system for large nuclear infrastructures," *IEEE Trans. Nucl. Sci.*, vol. 52, no. 6, pp. 2689–2691, Dec. 2005.

[148] M. A. Sotom, A. Signorini, T. Nannipieri, S. Faralli, G. Bolognini, and F. Di Pasquale, "Impact of loss variations on double-ended distributed temperature sensors based on Raman anti-Stokes signal only," *J. Lightw. Technol.*, vol. 30, no. 8, pp. 1215–1222, Apr. 15, 2012.

[149] K. Suh and C. Lee, "Auto-correction method for differential attenuation in a fiber-optic distributed-temperature sensor," *Opt. Lett.*, vol. 33, no. 16, pp. 1845–1847, Aug. 2008.

[150] M. A. Soto *et al.*, "Raman-based distributed temperature sensor with 1 m spatial resolution over 26 km SMF using low-repetition-rate cyclic pulse coding," *Opt. Lett.*, vol. 36, no. 13, pp. 2557–2559, Jul. 2011.

[151] J. Dakin, D. Pearce, A. Strong, and C. Wade, "A novel distributed optical fiber sensing system enabling location of disturbances in a Sagnac loop interferometer," *Proc. SPIE*, vol. 838, pp. 325–328, Mar. 1987.

[152] E. Udd, "Sagnac distributed sensor concepts," *Proc. SPIE*, vol. 1586, pp. 46–52, Jan. 1991.

[153] X. Fang, "A variable-loop Sagnac interferometer for distributed impact sensing," *J. Lightw. Technol.*, vol. 14, no. 10, pp. 2250–2254, Oct. 1996.

[154] P. M. Krummrich *et al.*, "Demanding response time requirements on coherent receivers due to fast polarization rotations caused by lightning events," *Opt. Exp.*, vol. 24, no. 11, pp. 12442–12457, May 2016.

[155] D. Charlton *et al.*, "Field measurement of SOP transients in OPGW, with time and location correlation to lightning strikes," *Opt. Exp.*, vol. 25, no. 9, pp. 9689–9696, May 2017.

[156] F. Ravet, F. Briffod, A. Goy, and E. Rochat, "Mitigation of geohazard risk along transportation infrastructures with optical fiber distributed sensing," *J. Civil Struct. Health Monitor.*, vol. 11, no. 4, pp. 967–988, Sep. 2021.

[157] F. Ravet, A. Melo, F. Oliveros, and E. Rochat, "Retrofitting existing optical fiber infrastructure to mitigate geohazard risk: The TGP case," in *Proc. ASME-ARPEL Int. Pipeline Geotech. Conf.*, Jun. 2021, Paper IPG2021-64796.

[158] F. Ravet, E. G. Ortiz, B. Peterson, G. Hoglund, and M. Niklès, "Geohazard prevention with online

continuous fiber optic monitoring," in *Proc. Rio Pipeline Conf. Expo.*, Rio de Janeiro, Brazil, 2011, Paper IBP1277_11.

[159] F. Ravet, C. Borda, E. Rochat, and M. Niklès, "Geohazard prevention and pipeline deformation monitoring using distributed optical fiber sensing," in *Proc. ASME Int. Pipeline Geotechnical Conf.*, Bogotá, Colombia, Jul. 2013, Art. no. V001T04A001, Paper IPG 2013-1908.

[160] F. Ravet, M. Niklès, and E. Rochat, "A decade of pipeline geotechnical monitoring using distributed fiber optic monitoring technology," in *Proc. ASME Int. Pipeline Geotech. Conf.*, Lima, Peru, Jul. 2017, pp. 1–18, Paper IPG2017-2503.

[161] G. A. Lanan, T. Cowin, B. Hazen, D. Maguire, J. D. Hall, and C. Perry, "Oooguruk offshore Arctic flowline design and construction," in *Proc. Offshore Technol. Conf.*, Houston, TX, USA, 2008, Paper OTC2008-19353.

[162] B. Eisler, G. Lanan, M. Niklès, and L. Zuckerman, "Distributed fiber optic temperature sensing system for buried subsea Arctic pipelines," in *Proc. Deep Offshore Technol. Conf. (DOT)*, Houston, TX, USA, 2008, pp. 12–14.

[163] F. Ravet, A. Børnes, C. Borda, E. Tjåland, H. Hilde, and M. Nikles, "DEH cable system preventive protection with distributed temperature and strain sensors," in *Proc. Int. Pipeline Conf. (IPC)*, Calgary, AB, Canada, 2012, pp. 21–30, Paper IPC2012-90275.

[164] F. Ravet, C. Silva, R. Gil, S. Maguire, and E. Rochat, "Sand dune migration monitoring for pipeline hazard risk mitigation: The Peru LNG coastal section case," in *Proc. Int. Pipeline Conf. (IPC)*, Calgary, AB, Canada, 2020, Art. no. V003T04A015, Paper IPC2020-9247.

[165] F. Ravet, C. Silva, R. Gil, S. Maguire, and E. Rochat, "Erosion risk mitigation with DTS based monitoring system," in *Proc. Abu Dhabi Int. Petroleum Exhib. Conf. (ADIPEC)*, 2020, Paper SPE-202654-MS.

[166] L. M. Highland and P. Bobrowski, "The landslide handbook—A guide to understanding landslides," U.S. Geol. Surv. Circular, Reston, VA, USA, Tech. Rep., 2008.

[167] C. Silva and F. Ravet, "Pipeline monitoring with geotechnical optical fiber," in *Proc. Int. Pipeline Geotech. Conf. (IGP)*, Lima, Peru, 2017, Art. no. V001T03A003, Paper IPG2017-2510.

[168] S. P. Timoshenko and J. N. Goodier, *Theory of Elasticity*. New York, NY, USA: McGraw-Hill, 1970.

[169] M.-F. Huang *et al.*, "Field trial of cable safety protection and road traffic monitoring over operational 5G transport network with fiber sensing and on-premise AI technologies," in *Proc. 26th Optoelectron. Commun. Conf.*, Hong Kong, 2021, Paper T5A.8.

[170] T. J. Xia *et al.*, "First proof that geographic location on deployed fiber cable can be determined by using OTDR distance based on distributed fiber optical sensing technology," in *Proc. Opt. Fiber Commun. Conf. (OFC)*, San Diego, CA, USA, 2020, pp. 1–3, Paper Th3A.5.

[171] C. Narisetty, T. Hino, M.-F. Huang, H. Sakurai, T. Ando, and S. Azuma, "TrafficNet: A deep neural network for traffic monitoring using distributed fiber-optic sensing," in *Proc. 27th ITS World Congr.*, Los Angeles, CA, USA, 2020. [Online]. Available: https://trid.trb.org/view/1759837

[172] T. J. Xia *et al.*, "Field trial of abnormal activity detection and threat level assessment with fiber optic sensing for telecom infrastructure protection," in *Proc. Opt. Fiber Commun. Conf. (OFC)*, San Francisco, CA, USA, 2021, pp. 1–3, Paper Th4H.3.

[173] C. Narisetty *et al.*, "Overcoming challenges of distributed fiber-optic sensing for highway traffic monitoring," *Transp. Res. Rec., J. Transp. Res. Board*, vol. 2675, no. 2, pp. 233–242, Feb. 2021.

[174] M. S. Longuet-Higgins, "A theory of the origin of microseisms," *Philos. Trans. Roy. Soc. London. A, Math. Phys. Sci.*, vol. 243, pp. 1–35, Sep. 1950.

[175] E. F. Williams *et al.*, "Scholte wave inversion and passive source imaging with ocean-bottom DAS," *Lead. Edge*, vol. 40, no. 8, pp. 576–583, Aug. 2021.

[176] A. Ugalde *et al.*, "Noise levels and signals observed on submarine fibers in the Canary Islands using DAS," *Seismolog. Res. Lett.*, vol. 93, no. 1, pp. 351–363, Jan. 2022, doi: 10.1785/0220210049.

[177] W. Wu, Z. Zhan, S. Peng, S. Ni, and J. Callies, "Seismic ocean thermometry," *Science*, vol. 369, no. 6510, pp. 1510–1515, Sep. 2020.

[178] S. Ide, E. Araki, and H. Matsumoto, "Very broadband strain-rate measurements along a submarine fiber-optic cable off Cape Muroto, Nankai subduction zone, Japan," *Earth, Planets Space*, vol. 73, no. 1, pp. 1–10, Mar. 2021.

[179] A. Garcia-Ruiz *et al.*, "Distributed detection of hydrogen and deuterium diffusion into a single-mode optical fiber with chirped-pulse phase-sensitive optical time-domain reflectometry," *Opt. Lett.*, vol. 44, no. 21, pp. 5286–5289, Nov. 2019.

[180] R. Magalhaes, T. Neves, L. Scherino, S. Martin-Lopez, and H. F. Martins, "Reaching long-term stability in CP-ϕOTDR," *J. Lightw. Technol.*, vol. 40, no. 12, pp. 3916–3922, Jun. 15, 2022.

[181] P. A. Williams, W. C. Swann, and N. R. Newbury, "High-stability transfer of an optical frequency over long fiber-optic links," *J. Opt. Soc. Amer. B, Opt. Phys.*, vol. 25, no. 8, pp. 1284–1293, Aug. 2008.

[182] F. Cunzheng, L. Hao, Y. Baoqiang, Y. Zhijun, and S. Qizhen, "246 km long distance fiber optic DAS system based on multi-span bidirectional EDFAs and cascaded AOMs," in *Proc. Opt. Fiber Commun. Conf. (OFC)*, San Diego, CA, USA, 2022, pp. 1–3, Paper W4D.4.

[183] Y. Horiuchi, S. Yamamoto, S. Akiba, and H. Wakabayashi, "Highly accurate fault localization over 4580 km optical amplifier system using coherent Rayleigh backscattter reflectometry," in *Proc. Eur. Conf. Opt. Commun. (ECOC)*, Montreux, Switzerland, 1993, Paper MoC1.3.

[184] T. Otani, Y. Horiuchi, T. Kawazawa, K. Goto, and S. Akiba, "Fault localization of optical WDM submarine cable networks using coherent-optical time-domain reflectometry," *IEEE Photon. Technol. Lett.*, vol. 10, no. 7, pp. 1000–1002, Jul. 1998.

[185] A. Bononi, M. Bertolini, P. Serena, and G. Bellotti, "Cross-phase modulation induced by OOK channels on higher-rate DQPSK and coherent QPSK channels," *J. Lightw. Technol.*, vol. 27, no. 18, pp. 3974–3983, Sep. 28, 2009.

ABOUT THE AUTHORS

Ezra Ip received the B.E. degree (Hons.) in electrical and electronics engineering from the University of Canterbury, Christchurch, New Zealand, in 2002, and the M.S. and Ph.D. degrees in electrical engineering from Stanford University, Stanford, CA, USA, in 2004 and 2008, respectively. His doctoral thesis was on coherent detection and digital signal processing for optical communications.
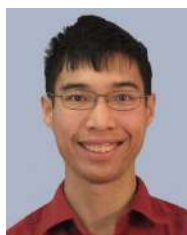
He joined NEC Laboratories America, Inc., Princeton, NJ, USA, in 2009, where he is currently a Senior Researcher with the Optical Networking and Sensing Department. He has published more than 100 journal articles and conference papers in the areas of high-capacity optical transmission, digital signal processing techniques, space-division multiplexing, and distributed fiber sensing.

Dr. Ip has served on the topical program committees of OFC, ECOC, APC, and other conferences. He is an Associate Editor of IEEE PHOTONICS TECHNOLOGY LETTERS.

Fabien Ravet (Senior Member, IEEE) received the Ph.D. degree in physics from the University of Ottawa, Ottawa, ON, Canada, in 2007. His doctoral thesis covered the study of Brillouin scattering fundamentals, its application to distributed sensing, and its implementation to structural health monitoring.

He started his career in 2004 as a Researcher at the University of Mons, Mons, Belgium, working on the development of characterization techniques for fiber optic systems. In 1999, he moved to GTS Network Services, Belgium, where he was in charge of the testing and evaluation of optical networking technologies. In 2000, he joined Nortel Networks, Canada, as Application Senior Designer for optical transport systems. From 2007 to 2021, he was with Omnisens SA, Morges, Switzerland, focusing on the development, the implementation, and the promotion of distributed fiber optic sensing technologies in the energy industry. He also contributed tot he development of IEC Standards for distributed sensing. He is currently the Chief Operations Officer with Gradesens, Switzerland, a company developing predictive maintenance solutions integrating wireless vibration and temperature sensors with advanced data analytics approach.

Hugo Martins, photograph and biography not available at the time of publication.

Ming-Fang Huang, photograph and biography not available at the time of publication.


Tatsuya Okamoto, photograph and biography not available at the time of publication.

Shaobo Han (Member, IEEE), photograph and biography not available at the time of publication.

Chaitnaya Narisetty, photograph and biography not available at the time of publication.

Jian Fang (Member, IEEE), photograph and biography not available at the time of publication.

Yue-Kai Huang (Member, IEEE) received the B.S. degree in electrical engineering and the M.S. degree in electro-optical engineering from National Taiwan University, Taipei, Taiwan, and the Ph.D. degree in electrical engineering from Princeton University, Princeton, NJ, USA, in 2008.
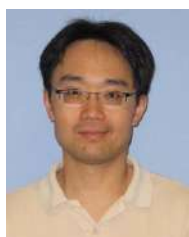
He joined NEC Laboratories America, Inc., Princeton, in 2008, where he currently holds the position of a Senior Researcher. He has published more than 100 journal articles and conference papers. He was awarded with more than 40 U.S. patents. His research interests and projects include long-distance fiber transmission system, optical and RF frontend designs for high-speed transceiver, and system design for distributed fiber sensing.

Dr. Huang has served on TPC subcommittees of OFC, CLEO, and OECC. He had reviewed many journals, including *Journal of Lightwave Technology*, IEEE PHOTONICS TECHNOLOGY LETTERS, and *Optics Letters*. He serves as an Associate Editor for *Optics Express*.

Milad Salemi, photograph and biography not available at the time of publication.

Etienne Rochat received the master's degree in engineering from the Swiss Federal Institute of Technology (EPFL), Lausanne, Switzerland, and the Ph.D. degree in science from the University of Neuchâtel, Neuchâtel, Switzerland.

He worked first as a Research Scientist at the ABB Corporate Research Centre, Baden, Switzerland, developing fiber sensors for remote pressure and temperature measurement in oil reservoir and then as a Research Fellow at the University of Essex, Colchester, U.K., in nonconventional optical communication. He joined Omnisens SA, Morges, Switzerland, in 2004, and worked originally as a Product Manager for the company former trace gas analyzer. In 2009, he became a research and development manager for fiber optic distributed sensing, then head of engineering in 2010, and CTO in 2013. He is in charge of product research and development for the company monitoring solution, featuring worldwide applications for pipeline, and power cable monitoring. He is the author of numerous papers in peer-reviewed journals and conference proceedings and the inventor of more than ten patent families.

Dr. Rochat is also an Active Member of the FOSA Technology Committee, and CIGRE and IEC Committees.

Fabien Briffod received the Ph.D. degree in electrical engineering from the Swiss Federal Institute of Technology, Lausanne, Switzerland, in 2002. His doctoral thesis covered the study of fiber-optic current sensors and their application to high-voltage ac or high-current dc.

In 2002, he joined Omnisens SA, Morges, Switzerland, as a Product Manager, where he was in charge of the development of fiber optic sensing instruments and solutions. Since 2010, he has been a Project Management Position, where he is responsible for the implementation of Omnisens monitoring solutions for customers from different industries, such as oil and gas (pipelines leak and ground movement), offshore-SURF (pipelines), and power (offshore wind farms and interconnection cables).

Alexandre Goy received the Diploma degree in microengineering from the Swiss Federal Institute of Technology (EPFL), Lausanne, Switzerland, in 2003, the master's degree in geology from the University of Lausanne, Lausanne, in 2008, and the Ph.D. degree in microscopy and nonlinear optics from the Group of Demetri Psaltis, EPFL, in 2013.

He had two postdoctoral experiences at Princeton University, Princeton, NJ, USA, and the Massachusetts Institute of Technology (MIT), Cambridge, MA, USA, where he worked on the applications of neural networks to optical imaging. In 2019, he joined Omnisens SA, Morges, Switzerland, as a Senior Research and Development Engineer, where he is involved in the development of distributed temperature and acoustic fiber sensing solutions.

Maria del Rosario Fernândez-Ruiz, photograph and biography not available at the time of publication.

Miguel Gonzâlez Herrâez (Member, IEEE), photograph and biography not available at the time of publication.